



FACULTÉ
DES SCIENCES

UNIVERSITÉ LIBRE DE BRUXELLES



北航物理学院
SCHOOL OF PHYSICS, BUAA

Search for high mass resonances in electron-electron and electron-muon final states with CMS data and study of exotic states with BESIII data

Thesis submitted by Xuyang GAO

in fulfilment of the requirements of the PhD Degree in Physics (ULB -
“Docteur en Sciences”) and in Particle physics and nuclear physics (BUAA)
Academic year 2018-2019

Supervisors: Professor Barbara CLERBAUX (Université libre de Bruxelles)

Interuniversity Institute for High Energies (ULB-VUB)

and Professor Chengping SHEN (Beihang University)

School of Physics

Thesis jury:

Prof. Gilles De Lentdecker (Université libre de Bruxelles, Chair)

Prof. Barbara Clerbaux (Université libre de Bruxelles, co-promoter)

Prof. Chengping Shen (Beihang University, co-promoter)

Prof. Yajun Mao (Peking University)

Prof. Arnd Meyer (RWTH Aachen University)

Prof. Li Yuan (Beihang University, Secretary)

Dr. Reza Goldouzian (University of Notre Dame)

PhD thesis

Search for high mass resonances in electron-electron and electron- muon final states with CMS data and study of exotic states with BESIII data

Beihang University
Université libre de Bruxelles

Supervisor:

Prof. Chengping Shen (BUAA)
Prof. Barbara Clerbaux (ULB)

Author:

Xuyang Gao

摘 要

标准模型是目前描述人们对自然界的物质及相互作用规律的认知的最为精确的理论，它描述了目前自然界已知的四种相互作用中的三种，即电磁相互作用，强相互作用和弱相互作用。截至目前，标准模型所描述的所有粒子都已经被发现，高能物理实验得到的结果也都与标准模型的计算结果在统计学上相符合。但标准模型仍然无法解释自然界所有的物质与相互作用，因此，标准模型被广泛的认为是一个更加基础的理论在低能下有限范围内的有效理论。

理论学家提出了很多种不同的超出标准模型框架的理论，尝试解释一种或多种标准模型无法解释的现象。这些新理论也预言了一些在当前阶段，可以被高能物理实验所观测到的信号。对这些信号的寻找，将为验证对应理论的可信度提供重要的直接证据。

与此同时，各个高能物理实验也先后发现了许多行为与粲偶素粒子类似的新粒子，这些被称为类粲偶素粒子的数量远超过目前理论在相应能量区间的预言，因此对这些类粲偶素粒子的参数性质研究，将会为理论上对这些粒子的解释提供重要的信息支持。

本篇论文的前半部分讲述了利用CMS实验在2016年和2017年收集到的实验数据，在电子-电子末态和电子-缪子末态上，在高质量区间寻找新的物理信号的物理分析。比如在电子-电子末态上，寻找质量更高的玻色子 Z'_{SSM} 和大统一理论(Grand unified theory, GUT)中预言的 Z'_ψ 玻色子，再比如在电子-缪子末态上，寻找来自于超对称模型里描述的R宇称破缺(R-parity violation, RPV)现象或量子黑洞模型(Quantum black hole, QBH)的轻子味破缺(Lepton flavor violation, LFV)现象。

本文首先利用了CMS实验在2016年收集到的积分亮度为 35.9 fb^{-1} 的数据，在电子-缪子末态，尝试寻找轻子味破缺(LFV)现象。数据与基于标准模型的模拟事例符合很好，没有发现超出当前标准模型描述的物理现象。因此，我们计算了95%置信水平下，针对不同理论模型预言的最小可以存在的质量，即排除质量。RPV, QBH和 Z' 的排除质量。分别是：超对称理论的R-parity violating模型，排除质量为3.8 TeV (耦合常数 $\lambda_{132} = \lambda_{231} = \lambda'_{311} = 0.1$)；量子黑洞Quantum black hole的模型，在额外维度 $n = 1, (4, 5, 6)$ 情况下的排除质量为3.6, (5.3 5.5, 5.6) TeV；高质量的电中性 Z' 粒子，在衰变到 $e\mu$ 末态分支比为10%的假设下，得到的排除质量为4.4 TeV；

之后，本文利用CMS实验在2016年收集到的积分亮度为 35.9 fb^{-1} 的数据，同时结合2017年收集到的积分亮度为 41.1 fb^{-1} 的数据，在电子-电子末态上尝试寻找高质量的共振态信号。最终搜索结果与标准模型描述的一致，并未发现新物理信号。因此，我们计算了针对不同理论模型预言的 Z'_{SSM} 和 Z'_ψ 玻色子的排除质量，分别为4.7 TeV和4.1 TeV。

本篇论文的后半部分是利用联合拟合方法，根据BESIII实验最新发布的实验数据，研究类粲偶素粒子 $Y(4220)$ 的参数性质。在假设出现于反应过程 $e^+e^- \rightarrow \pi^+\pi^-h_c$ ， $\omega\chi_{c0}$ ， $\pi^+\pi^-J/\psi$ ，和 $D^0D^{*-}\pi^+ + c.c.$ 中的，不变质量在 4.2 GeV附近的信号是来自同一个共振态的前提下，利用联合拟合的方法，得出了这个共振态的质量和宽度参数，并结合理论上关于这个共振态的一些解释和本次拟合中得出的轻子化衰变宽度，做出了一些讨论。

关键词：CMS， Z' ，高质量共振态，轻子味破缺，奇特态， $Y(4220)$ ，类粲偶素。

Abstract

We present a search for lepton flavor violation processes at $e\mu$ final states with the data collected by the CMS experiment at the LHC at a center-of-mass energy of 13 TeV in 2016 corresponding to the integrated luminosity of 35.9 fb^{-1} . No evidence for physics beyond the Standard Model is observed in the $e\mu$ invariant mass spectrum, the results are interpreted in terms of three different models, an R-parity violating SUSY model (RPV), a heavy Z' gauge boson model and a quantum black hole model (QBH). In addition, the lower mass limits at 95% confidence level (C.L.) are found for RPV $M_{\tilde{\nu}_\tau}$ to be 1.7 (3.8) TeV corresponding to the RPV couplings $\lambda_{132} = \lambda'_{311} = 0.01$ (0.1), for Z' to be 4.4 TeV, and for QBH to be 3.6 (5.3, 5.5, 5.6) corresponding to the extra dimensions $n = 1$ (4, 5, 6).

We also present a search for new high-mass resonances decaying into electron pair with CMS 2016 data. No evidence of signature beyond the Standard Model prediction in the ee invariant mass spectrum observed, therefore the lower mass limits at 95% C.L. are found for sequential Standard Model Z'_{SSM} boson to be 4.5 TeV, for grand unify theory Z'_ψ boson to be 3.9 TeV, and for spin-2 graviton from the Randall-Sundrum model at 1.85 (3.3, 3.9) TeV corresponding to coupling parameters $k/\overline{M}_{\text{Pl}} = 0.01$ (0.05, 0.1). Then we update the results of lower mass limits for Z'_{SSM} and Z'_ψ to be 4.7 TeV and 4.1 TeV with the combination of 2016 data in ee and $\mu\mu$ channels and 2017 data in ee channel.

Further to these, a study of the vector charmonium-like state $Y(4220)$ is performed by using a combined fit on the cross sections of $e^+e^- \rightarrow \pi^+\pi^-h_c$, $\omega\chi_{c0}$, $\pi^+\pi^-J/\psi$, and $D^0D^{*-}\pi^+ + c.c.$ measured by the BESIII experiment. The mass and width of the $Y(4220)$ are found to be $M = (4219.6 \pm 3.3 \pm 5.1) \text{ MeV}$ and $\Gamma = (56.0 \pm 3.6 \pm 6.9) \text{ MeV}$, where the first uncertainties are statistical and the second ones are systematic. We find the lower limit of its leptonic decay width to be 30 eV. We also estimate its partial decay width to $\pi\pi J/\psi$ in different scenarios. These results can be compared with the theoretical expectations of different models, and help the understanding of the nature of the $Y(4220)$ state.

Keywords: CMS, LHC, Z' , high mass resonance, lepton flavor violation, $Y(4220)$, XYZ particles, charmonium-like state, BESIII.

Résumé

Nous présentons une recherche de violation de la saveur leptonique dans l'état final $e\mu$ avec les données collectées par l'expérience CMS au LHC en 2016. Les données ont été prises à une énergie de centre de masse de 13 TeV en 2016 et correspondent à une luminosité intégrée de 35.9 fb^{-1} . Aucune preuve d'existence de physique au-delà du modèle standard n'ayant été observée dans le spectre de masse invariante $e\mu$, les résultats sont interprétés selon trois modèles différents: un modèle SUSY (RPV) violant la R-parité, un modèle de boson de jauge massif Z' et un modèle de trou noir quantique (QBH). Des limites de masse inférieure à un niveau de confiance de 95% (95% C.L.) ont été trouvées pour chacun des trois modèles: 1.7 (3.8) TeV pour un sneutrino tau RPV, correspondant à un couplage RPV $\lambda_{132} = \lambda'_{311} = 0.01$ (0.1), 4.4 TeV pour un Z' , et 3.6 (5.3, 5.5, 5.6) pour un QBH correspondant à $n = 1$ (4, 5, 6) dimensions supplémentaires.

Nous présentons également une recherche de nouvelles résonances de masses se désintégrant en paires d'électrons avec les données prises par CMS en 2016. Aucune physique au-delà du modèle standard n'a été observée dans le spectre de masse invariante ee . Des limites inférieures de masse à 95% C.L. ont été calculées: 4.5 TeV pour le boson Z'_{SSM} du modèle standard séquentiel, 3.9 TeV pour le boson Z'_{ψ} du modèle de supercordes, et 1.85 (3.3, 3.9) TeV pour le graviton spin-2 du modèle de Randall-Sundrum pour des paramètres de couplage k/\bar{M}_{Pl} 0.01 (0.05, 0.1). Ensuite, en combinant les données 2016 dans les canaux ee et $\mu\mu$ avec les données 2017 dans le canal ee , nous avons obtenu des nouvelles limites de 4.7 TeV pour la masse du Z'_{SSM} et de 4.1 TeV pour la masse Z'_{ψ} .

De plus, une étude sur le vecteur de type charmonium $Y(4220)$ a été réalisée. Il s'agit d'un ajustement combiné sur les sections efficaces de $e^+e^- \rightarrow \omega\chi_{c0}$, $e^+e^- \rightarrow \pi^+\pi^-h_c$, $e^+e^- \rightarrow \pi^+\pi^-J/\psi$ et $e^+e^- \rightarrow D^0D^{*-}\pi^+ + \text{c. c.}$ mesurés par l'expérience BESIII. Nous avons trouvés une masse $M = (4219.6 \pm 3.3 \pm 5.1) \text{ MeV}$ et une largeur totale $\Gamma = (56.0 \pm 3.6 \pm 6.9) \text{ MeV}$ pour le $Y(4220)$, où les premières incertitudes sont statistiques et les deuxièmes sont systématiques. Nous avons déterminé une limite inférieure d'environ 30 eV pour sa largeur de désintégration leptonique. Nous estimons également sa largeur de désintégration partielle en $\pi J/\psi$ dans plusieurs scénarios. Ces résultats peuvent être comparées aux prédictions des modèles théoriques et permettent de mieux comprendre la nature de l'état $Y(4220)$.

Acknowledgements

I have received supports from both Beihang University and Université libre de Bruxelles as a joint PhD. The research projects in this thesis were funded by China Scholarship Council and supported by the Academic Excellence Foundation of BUAA for PhD Students.

I would like to thank my supervisors Prof. Chengping Shen in BUAA and Prof. Barbara Clerbaux in ULB for giving me great supports, guidance and advices with extraordinary patience during my whole PhD period. I started my PhD study in 2014, Prof. Chengping Shen showed me the general concepts of particle physics, guided me the first step to this area, and introduced me as a Joint PhD student to ULB. I were in Bruselles from 2015 to 2017, under the guidance and supervision of Prof. Barbara Clerbaux, she is a very nice person. She introduced me to the lab members and taught me how to work in a collaboration. They also introduced me to the lectures, summer schools and meetings, from which I benefited a great deal. Both supervisors also gave strong supports to my PhD thesis with the ideas and writing skills.

Then I would like to thank Reza Goldouzian, who supervised all my CMS works and taught me lots of knowledge both in physics and coding. Furthermore, I would like to thank my colleagues Wenxing, Diego, David and Qun and other nice colleagues in IIHE, they helped me a lot during my stay in Belgium. I would like to thank my colleagues and friends in China, also.

In the end, I would like to thank my family for their understandings, supports and trusts, especially to my wife Tingting for being with me.

Contents

1	Theoretical and experimental bases	3
1.1	Standard model	3
1.2	The physics beyond the Standard Model	5
1.2.1	Questions that Standard Model does not address	5
1.2.2	BSM models considered in this thesis	6
1.2.2.1	R-parity violating SUSY model	6
1.2.2.2	Quantum black hole model	6
1.2.2.3	Z' models	7
1.2.2.4	Randall-Sundrum model for a spin-2 graviton candidate	7
1.2.3	Results review	8
1.3	Exotic states	8
1.3.1	The quark model	8
1.3.2	Charmonium(-like) XYZ states	9
1.3.2.1	The X states	11
1.3.2.2	The Y states	13
1.3.2.3	The Z states	14
1.3.2.4	The pentaquark states	16
1.3.2.5	A short summary of charmonium-like states	17
1.3.2.6	Y states at 4.2 GeV in BESIII experiment	17
1.4	Particle physics experiment	19
1.4.1	The Large Hadron Collider (LHC)	20
1.4.2	The Compact Muon Solenoid (CMS)	20
1.4.2.1	Superconduction magnet	21
1.4.2.2	Inner tracking system	21
1.4.2.3	Electromagnetic calorimeter	22
1.4.2.4	Hadron calorimeter	22
1.4.2.5	Muon Detector	23
1.4.2.6	Trigger System	23
1.4.2.7	Electron reconstruction in CMS	24

1.4.2.8	Muon reconstruction in CMS	24
1.5	Variable definitions	24
2	Search for lepton flavor violation processes in electron-muon final states with CMS	
	2016 data	27
2.1	Data and simulation samples	27
2.1.1	Data	27
2.1.2	RPV, Z' , and QBH signal samples	27
2.1.3	SM background samples	28
2.2	Event selection	28
2.2.1	Electron reconstruction	29
2.2.2	Electron identification and isolation	29
2.2.3	Muon reconstruction	30
2.2.4	Muon identification and isolation	30
2.2.5	Trigger strategy	32
2.2.6	Event selection	32
2.2.7	Event corrections	33
2.3	Background estimation	35
2.3.1	Prompt background	35
2.3.2	Jet background	35
2.4	Systematic uncertainties	37
2.4.1	Background systematics	37
2.4.2	RPV, QBH, and Z' signal systematics	40
2.5	Invariant mass distributions	44
2.6	Invariant mass resolution	46
2.7	Statistical interpretation	49
2.7.1	Signal model	50
2.7.2	Background model	52
2.7.3	Limit setting procedure	52
2.8	Limit results	54
2.8.1	RPV τ sneutrino	54
2.8.2	Sequential Standard Model Z'	55
2.8.3	QBH	55
2.9	Chapter summary and personal contributions	58

3	Search for high mass resonances in dielectron final states with CMS 2016 and 2017 data	59
3.1	Data and simulation samples	59
3.1.1	Data	59
3.1.2	SM background samples	59
3.1.3	Signal samples	60
3.2	Tag and probe method	60
3.3	Trigger strategy	60
3.4	Event selection	61
3.5	HEEP ID scale factors	61
3.5.1	HEEP ID efficiencies	61
3.5.2	HEEP ID and scale factors	62
3.6	Mass resolution and scale	63
3.7	Standard model backgrounds	64
3.7.1	SM Drell-Yan background	65
3.7.2	$t\bar{t}$ and $t\bar{t}$ -like background	66
3.7.3	Jet background	66
3.8	Invariant mass plot and limit plot	67
3.8.1	Systematic uncertainties	67
3.8.2	Statistical methods	68
3.8.3	Limit inputs	68
3.8.4	Results	70
3.9	Update with CMS 2017 data	74
3.10	Chapter summary and personal contributions	77
4	Study exotic state $Y(4220)$ with BESIII data	79
4.1	$Y(4220)$ state in BESIII	79
4.2	Motivation	82
4.3	The data and the fit formalism	82
4.4	Fit results	83
4.5	Systematic uncertainties	86
4.6	Chapter summary and discussion	86
5	Conclusion	89
6	Appendix	91
A	Lepton kinematics	91
B	LFV signal invariant mass resolution	100
C	HEEP ID efficiencies	102

D ee mass scale and resolution	105
References	107

Introduction

The Standard Model of particle physics based on the quantum field theory provides an successful description of the fundamental constituents of nature as we observe. It describes three of four kinds of forces in the universe, the electromagnetic force, the weak force and the strong force. The mechanisms of Standard Model are tested by various experiments and are found to be in very good agreement with experimental results. However, Standard Model is generally admitted to be the best but not the most fundamental theory, as it fails to address some of most important questions about the matter and forces in our universe. Therefore theories beyond Standard Model (BSM) are raised.

Some of the favored BSM theories attempt to extend the Standard Model by introducing new symmetries to the current model or to unify the forces at higher energy scale, which could lead to some observable signatures in the invariant mass spectra of final state particles. For example, the lepton flavor violation processes from a high mass state decaying into an electron and a muon, or a new heavy neutral Z boson-like particle decaying into electron pair.

In another hand, the Standard Model allows the existence of exotic states, they have the quark or gluon components which differ from the “ordinary” ones ($q\bar{q}$ or qqq). In the last decade, some experiments observed many resonant signatures at low energy scale that look like inside the law of Standard Model but out of the predictions by some theoretical calculations. For example, the number of observed resonances that have $c\bar{c}$ components in experiments at the mass above $D\bar{D}$ threshold is more than that of charmonium states predicted by the potential model. These states are referred to as charmonium-like states and would be good candidates for exotic states. The study on properties of such resonances would help to push the understanding of the exotic states.

People build large-scale scientific facilities in order to study the nature. In high energy physics field, various large accelerators and detectors are built for different physics purposes, that currently include the study and validation of the current Standard Model, and the search for new physics beyond the Standard Model. In general, there are two types of accelerators, one runs at the high energy frontier, the other one runs at high density frontier. The former one provides a horizon through very wide energy range, while the latter one gives high statistical data on dedicated energy points.

In this thesis, Chapter 1 gives a short introduction about the Standard Model and the physics beyond, the general accelerators and detectors, and details some theories that motivate the analysis performed in this thesis. Chapter 2 presents the search for the lepton flavor violation processes in $e\mu$ final states with CMS 2016 data, Chapter 3 details the search for high mass resonances at ee final states with CMS 2016 and 2017 data. Chapter 4 presents the study of the resonant parameters of a charmonium-like state, the $Y(4220)$, by simultaneous fits to the cross sections of different decay modes measured by the BESIII experiment.

Chapter 1

Theoretical and experimental bases

1.1 Standard model

The Standard Model (SM) of particle physics is a theory to describe the laws of our universe at the micro-scale. It is based on the quantum field theory that describes the matter particles and force particles as fields. The predictions and interpretations of the Standard Model have been observed and tested by various experiments with exquisite precision, the results indicate that the Standard Model is the most accurate theory for the forces and matter up to now.

Figure 1.1 shows the components of SM, it splits particles in the universe into two groups. The first group is the matter particles, including the quarks and leptons, they are point-like fermions with semi-integer spin. The second group is the force particles, they are bosons with integer spin, the matter particles interact with each other by exchanging the force particles.

There are six different flavors of quarks, which are grouped in three generations, each generation contains a $+2/3$ and a $-1/3$ charged partner. Quark carries color, an internal property that can explain the construction of hadrons. There are three different colors for each quark, labeled ‘R’, ‘G’ and ‘B’. The anti-quarks have the same masses but opposite charges and colors. All isolated objects must be colorless according to the law of Standard Model, so that there is no “free” quark observed, all quarks can only exist within the colorless combinations. There are some possible combinations of quark found in experiments such as three quarks qqq for baryons and a quark anti-quark pair $q\bar{q}$ for mesons.

The second class of matter particles is the leptons. They carry integer electrical charges but no color charges. The leptons are grouped up with three generations, each includes a lepton and a neutrino, the anti-leptons have the same masses but opposite charges. The lepton can decay to another generation lepton but must obey the lepton flavor number conservation.

There are four kinds of fundamental forces acting on the matter particles, the electromagnetic force, the weak nuclear force, the strong nuclear force, and the gravitational force.

However the gravitational force is a long range force and performs differently from the other three forces, it gives so negligible effect in the subatomic level that it is usually ignored at the micro-scale.

1. THEORETICAL AND EXPERIMENTAL BASES

Each of the other three forces is carried by intermediate particles that are the excitations of associated fields.

The intermediate particle of the electromagnetic force is the photon, which is an electrical neutral massless boson. The relevant theory on the electromagnetic force in the Standard Model is known as quantum electrodynamics (QED).

The weak force is responsible for all flavor-changing reactions. The intermediate particles of the weak force are the spin-1 charged W^\pm bosons and the neutral Z^0 boson. They are so heavy that the effective ranges are very short.

The theory on the strong force in the Standard Model is known as quantum chromodynamics (QCD). The intermediate particles of the strong force are known as gluons. The gluons are massless and couple to color charge. The strong interaction has a larger coupling constant than the electromagnetic force, $\alpha_S \sim 1$ whereas $\alpha_{EM} \sim 1/137$.

In addition to the particles introduced above, there is one particle, the spin-zero Higgs particle, that plays a particularly special role in the Standard Model. It has unique properties that can provide other particles masses. According to the Higgs theory, the whole of space is filled with a non-zero expectation value of the Higgs field. The particles which interact with this scalar field have modified properties and acquire masses according to their strength of interactions with the field.

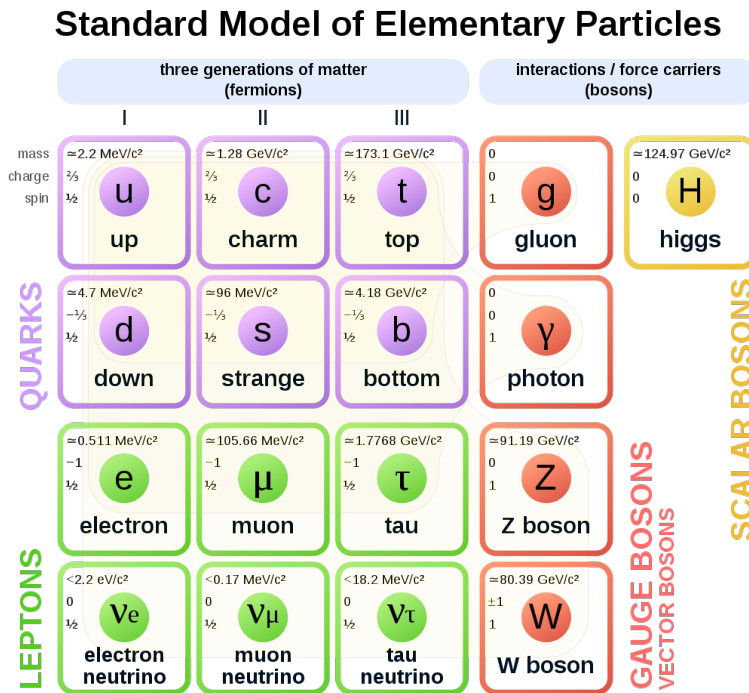


Figure 1.1: Standard Model of Elementary Particles.

1.2 The physics beyond the Standard Model

The SM is not the perfect theory of everything. There still are some important questions about the matter and forces out the approach of the Standard Model. For examples, the neutrino masses, the absence of gravity, the dark matter and dark energy, the number of free parameters in SM, and the asymmetry between matter and anti-matter.

The SM is therefore commonly admitted as a low energy approximation of a more fundamental theory at high energy.

1.2.1 Questions that Standard Model does not address

The examples of issues mentioned above are described below:

- The neutrino masses: the neutrino should be massless particles according to the SM. However, the neutrino oscillation is observed in experiments that hints the neutrinos should have mass since they can change flavors. If massive neutrinos are considered in the SM framework, new theoretical problems would arise. For example, the upper neutrino mass limits are set at $m < 2$ eV, which are extraordinary small masses compared to other SM particles.

- The gravity: the gravity is not included in the SM since it is so weak at the sub-atomic scale comparing to the other three kinds of forces. There is no interaction to explain the gravitational attraction between the fundamental particles. And the approaches arising from the SM can not work well on the experimental results, which is apart from the general relativity as well.

- The dark matter/energy: the mass distribution got from the cosmological observations according to the velocity and position of stars indicates that the mass of the whole universe is much more than the observable matter. This assumption is further supported by the temperature and polarization anisotropies from the Cosmic Microwave Background. These non-luminous components which contribute only to gravity are referred to as dark matter and dark energy. In general, the Standard Model explains only about 5% of the energy present in the universe, while the content of dark matter is around 26%, the rest 69% component is due to the dark energy.

- Number of free parameters in SM: the number of free parameters in SM is as many as 19. These parameters come from the three CKM mixing angles, one CP violation phase, one EM coupling constant, one weak coupling constant, one strong coupling constant, one QCD vacuum angle, one vacuum expectation value, one mass of the scalar boson, and nine fermion masses. The values of these parameters are known from experiments, the origin of the values and the relations between each other are still unknown.

- Matter anti-matter asymmetry: the content of matter and anti-matter in the universe should be almost equal according to the Standard Model despite the charge conjugation parity symmetry violation exists. But if we assume that there are equal matter and anti-matter in the initial universe, the observed matter in the universe are many orders of magnitude higher than the maximum allowable

1. THEORETICAL AND EXPERIMENTAL BASES

value of the Standard Model. This may hint the existence of some new violation processes beyond the SM.

1.2.2 BSM models considered in this thesis

This thesis represents a search for lepton flavor violation processes in $e\mu$ final states and a search for neutral high mass resonances in ee final states. The relevant theoretical models are listed as follows.

1.2.2.1 R-parity violating SUSY model

The Supersymmetry (SUSY) introduces a new symmetry between the SM particles, which is regarded as one of the most promising theories of physics beyond the Standard Model. In SUSY, each SM particle would have an associated particle, which is known as its superpartner, and would share the same mass and internal quantum numbers except spin. Once a spontaneously broken symmetry happens, the mass of SM particles and the relevant superpartners would be different. These superpartners would be new and undiscovered particles.

In many models of SUSY, the terms of super-potential which violate both baryon and lepton number, are removed from the classical Lagrangian by asking for an additional symmetry, called R-parity.

In this thesis, the conservation of R-parity is not assumed, the R-parity violation (RPV) terms of the super-potential (W_{RPV}) have the following structure [1]:

$$W_{RPV} = \epsilon_{ab} \left[\frac{1}{2} \lambda_{ijk} L_i^a L_j^b \bar{E}_k + \lambda'_{ijk} L_i^a Q_j^{xb} \bar{D}_{kx} \right] - \epsilon_{ab} \kappa^i L_i^a H_u^b + \frac{1}{2} \epsilon_{xyz} \lambda''_{ijk} \bar{U}_i^x \bar{D}_j^y \bar{D}_k^z \quad (1.1)$$

Where L_i and E_i present the super-fields of the scalar super-partners of leptons, the Q_i , U_i , D_i present the super-fields of the scalar super-partners of quarks.

The λ and λ' are Yukawa couplings that lead to lepton number (L) violating interactions. Here the tau sneutrino $\tilde{\nu}_\tau$ is chosen as the predicted particle because it is a viable lightest supersymmetric particle (LSP) candidate that can decay into the final state under study via the coupling λ_{123} or λ'_{311} .

1.2.2.2 Quantum black hole model

Many models have been developed to address the hierarchy problem using low scale quantum gravity [2, 3, 4]. These models allow the production of microscopic black holes in high energy particle collisions. These black holes are different from their astrophysical counterparts in the fact that their masses are expected to be close to the Planck scale which is in the TeV region. Semi-classical black holes are thermal objects, their decays are expected to be well described by Hawking radiation and they are expected to have masses of 5 to 20 times the Planck scale. With masses expected to be above 5 TeV, it is less probable that semi-classical thermal black holes will be observed at the LHC with a pp collision at 13 TeV center of mass energy. However non-thermal QBHs are predicted to have masses

close to the Planck scale and are an excellent candidate to be observed at the LHC. Non-thermal black holes are expected to decay into a pair of particles.

QBHs can decay to many states, and the LFV final state is one of the many allowed states. Consequently, this thesis presents a search for the decay of $\text{QBH} \rightarrow e\mu$ as well.

1.2.2.3 Z' models

- Sequential Standard Model Z'

Sequential Standard Model extends the gauge group of the SM by additional $U'(1)$ gauge groups. The $U'(1)$ gauge groups, or a linear combination of them, can be broken near the TeV scale, giving rise to new massive gauge bosons include the Z' boson, called Z'_{SSM} . The Z'_{SSM} could be a benchmark model since it describes a heavy neutral Z' boson that has SM-like couplings to Standard Model Z boson.

- GUT Z' model

The grand unified theory (GUT) tries to extend the gauge group of SM to combine the interactions of the weak, strong and electron magnetic into one at high energy. It may provide a probability to a theory of everything if it can unify gravity with three other interactions as well. Grand unified theories based on the E_6 gauge group predict the existence of new neutral gauge bosons [6, 7]. One imagines a symmetry breaking pattern $E_6 \rightarrow SO(10) \times U(1)_\psi \rightarrow SU(5) \times U(1)_\chi \times U(1)_\psi$. Then $SU(5)$ breaks to the SM and only one linear combination $G = U(1)_\theta = c_\theta U(1)_\psi - s_\theta U(1)_\chi$ remains light at the TeV scale, θ is treated as a free parameter with the value of $\theta = 0$, corresponds to the boson called Z'_ψ .

We can consider not only the flavor conservation decay such as $Z' \rightarrow ee$ but also the LFV decay $Z' \rightarrow e\mu$. Due to simplicity reasons, interference between the SM Z boson and the Z' is not included. We consider a branching ratio of $\text{BR}(Z' \rightarrow e\mu) = 10\%$ to be constant over the whole mass range from 500 GeV up to 5 TeV similar to the branching ratio of the Standard Model Z to leptons.

1.2.2.4 Randall-Sundrum model for a spin-2 graviton candidate

Theories that allow the gravitational force to propagate into extra spatial dimensions [8] could explain the large separation between the electroweak symmetry breaking energy scale and the gravitational energy scale. In such models, graviton excitations could be observed as spin-2 high-mass resonances.

Kaluza-Klein graviton (GKK) excitations arising in the Randall-Sundrum (RS) model of extra spatial dimensions [8, 9] involve a finite five-dimensional bulk that is warped as a function of the position of the four-dimensional subspace in the fifth dimension. In particular, the RS model predicts excited Kaluza-Klein modes of the graviton, without suppressing its couplings to the SM particles. The modes appear as spin-2 resonances and can decay into dilepton final states. There are two free parameters in the model: the mass of the first graviton excitation and the coupling k/\overline{M}_{Pl} , where k is the warp factor of the five-dimensional anti-de Sitter space and \overline{M}_{Pl} is the reduced Planck mass.

1. THEORETICAL AND EXPERIMENTAL BASES

The intrinsic widths of the first excitation of the gravitons for the coupling parameters k/\overline{M}_{Pl} of 0.01, 0.05, and 0.10, are 0.01, 0.36 and 1.42 GeV, respectively.

1.2.3 Results review

Direct searches for resonances in the $e\mu$ invariant mass spectrum with interpretations in terms of $\tilde{\nu}_\tau$ productions have been carried out by the CDF [11] and D0 [12] collaborations at the Tevatron. At LHC, the search has been performed by the ATLAS collaboration using proton-proton collision data at a center of mass energy of 7 TeV [13], 8 TeV [14] and 13 TeV [15, 16] and by the CMS collaboration [17] ([18]) using proton-proton collision data at a center of mass energy of 8 TeV (13 TeV).

Scenarios of resonant tau sneutrino lightest supersymmetric particle production in R-parity violating supersymmetry are excluded, by the CMS 8 TeV search, for LSP masses below 1.28 TeV for couplings $\lambda_{132} = \lambda'_{311} = 0.01$ and below 2.16 TeV for $\lambda_{132} = 0.05$ and $\lambda'_{311} = 0.1$.

Search for QBHs decaying to $e\mu$ final state was performed previously by CMS collaboration [17] and ATLAS collaboration [15], the excluded masses were found to be 3.63 (2.36) TeV by CMS and 4.54 (2.44) TeV by ATLAS for the ADD $n=6$ (RS $n=1$).

Searches for high-mass Z' gauge bosons at ee final states have been performed by the CMS collaboration at the LHC with proton-proton collision data collected at centre-of-mass (c.m.) energy $\sqrt{s} = 7$ TeV [19, 20], 8 TeV [21, 22] and 13 TeV [23] and the excluded mass of combined ee and $\mu\mu$ channels were found to be 2.33 (2.0) TeV, 2.9 (2.57) TeV and 3.37 (2.82) TeV for Z'_{SSM} (Z'_ψ) models, respectively. Similar searches have also been performed by the ATLAS collaboration with data collected at 7 TeV [24, 25], 8 TeV [26], and 13 TeV [27] and the excluded mass were found to be 1.408 (0.738) TeV, 2.90 (2.51) TeV and 4.3 (3.6) TeV, respectively.

Results of searches for spin-2 graviton in pp collision data have previously been reported by the ATLAS [26, 27] and CMS [21, 23] Collaborations. At the Tevatron, the CDF and D0 Collaborations have published results based on a pp collision sample at $\sqrt{s} = 1.96$ TeV, corresponding to an integrated luminosity of approximately 5 fb^{-1} [28, 29, 30, 31, 32, 33].

1.3 Exotic states

1.3.1 The quark model

In particle physics, the quark model is a classification scheme for hadrons in terms of their valence quarks in a meaningful way. The quark model is successful in organizing the large number of known lighter hadrons that were being discovered starting in the 1950s. Within the quark model, the inter-quark interactions include the linear confinement force and the one gluon exchange force. There also exist various hyperfine interactions such as the spin-spin interaction, the color-magnetic interaction, the spin-orbit interaction, and the tensor force, etc. Up to now, nearly all the mesons and baryons can be classified within such a simple quark model picture.

In another hand, the theory gives no limit on the number of quarks in a hadron, as long as the hadron's color charge is white, or color-neutral, such as the tetraquarks ($q\bar{q}q\bar{q}$), the pentaquarks ($qqqq\bar{q}$) and the glueballs, which are sometimes denoted as exotic states. The observed quarkmonium-like whose properties do not appear to fit the standard picture of charmonium and bottomonium state would be good candidates for such exotic states.

1.3.2 Charmonium(-like) XYZ states

The flavorless meson composed by a charm and an anti-charm quark is called ‘‘charmonium’’, the first charmonium state is the J/ψ meson observed in 1974. Theorists give a prediction for the masses of the charmonium states according to the static quark anti-quark potential in strong interaction [10, 34, 35]. The spectrum of predicted charmonium states is shown in figure 1.2.

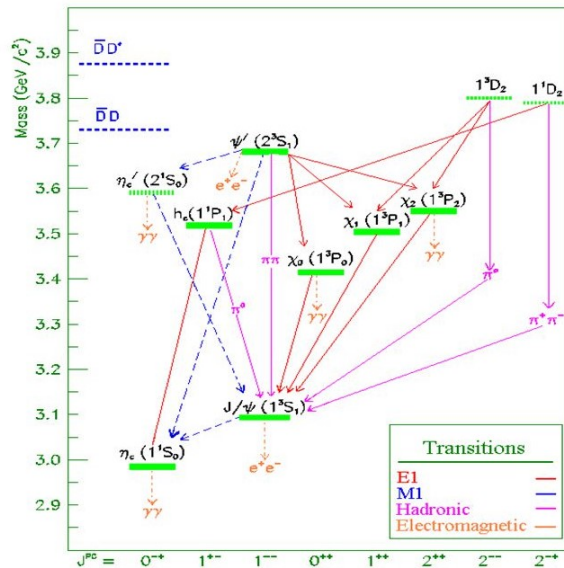


Figure 1.2: The charmonium spectrum.

However, during the past decades, many non-expected states were found, which do not fit into the potential model prediction which is shown in figure 1.3. The number of such non-expected states over the $D\bar{D}$ threshold is much more than the number of predicted charmonium states. These kinds of states out of prediction but have components of charm anti-charm are called charmonium-like states.

In general, according to the different production mechanisms, all the observed charmonium-like states were produced by one of the following ways:

- B meson decay process
- e^+e^- annihilation process
- Double charmonium production
- $\gamma\gamma$ fusion process

1. THEORETICAL AND EXPERIMENTAL BASES

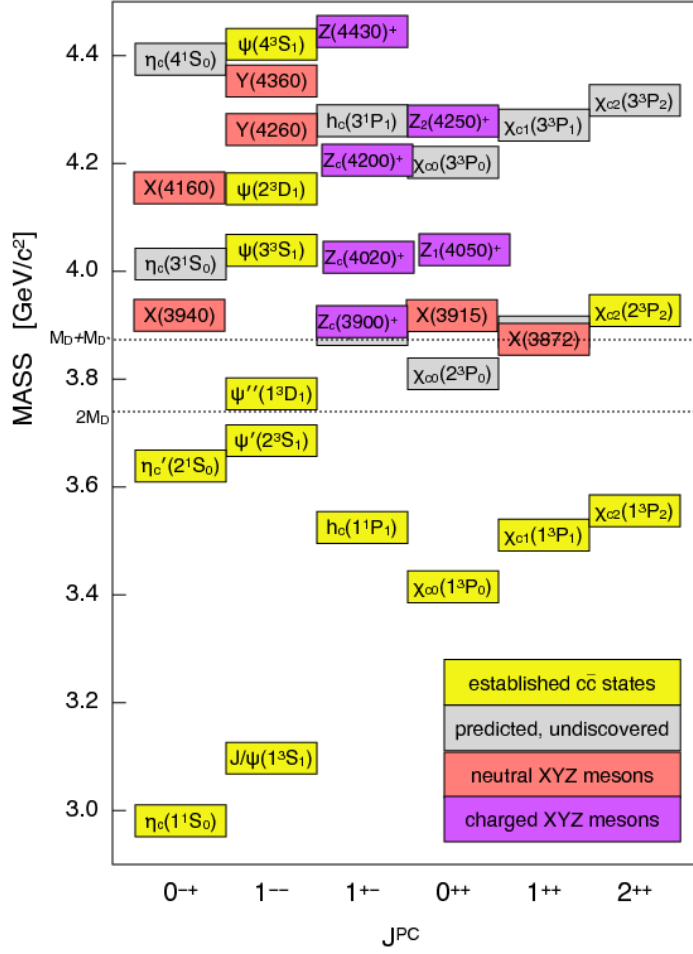


Figure 1.3: Part of the observed charmonium(-like) states.

- Hadronic decays of the higher charmonium states

The observed charmonium-like states are named as the form $X/Y/Z(\text{Mass})^{\text{charge}}$ according to their J^{PC} numbers and masses, where J is the angular momentum, P is the intrinsic parity, and C is the charge conjugation parity.

Many of the charmonium-like states were observed at “B-factories”, BaBar experiment and Belle experiment, which provide the e^+e^- collision events at beam energies 10.5 GeV-11.0 GeV, and have quite high B mesons production rate. With a typical instantaneous luminosity of $1 \times 10^{34} \text{ s}^{-1} \text{ cm}^{-2}$, considering the cross section $\sigma(e^+e^- \rightarrow \Upsilon(4S)) \simeq 1$ nano barn, we get about 10^6 B meson pairs per day. In addition to the study of the charmonium(-like) spectra through the B meson decay, the initial state radiation (ISR) method provides a way to get e^+e^- collision events at B-factories. The electron (positron) has a probability to radiate one or more photons that take part of the energy away before collision, those events can be used to study the charmonium(-like) spectra.

Besides the B-factories introduced above, there are some other particle physics experimental collaborations that have given considerable contributions to the observation and study on the XYZ

states, such as CLEO-c [36], BESIII [37], CDF [38], D0 [39], LHCb [40], CMS [41], and so on. All these collaborations have been continuing to provide a series of observations and confirmations on the XYZ states, which inspired theorists to focus their interests on exploring the underlying mechanism behind those exotic phenomena.

As one of the most important issues in hadron physics, the study of the charmonium-like states provides us a good chance to deepen our understanding of the complicated non-perturbative behavior of QCD in the low energy regime. Especially, investigations of the underlying structures of the charmonium-like states may help us to understand the mechanism of the confinement and chiral symmetry breaking mechanism better.

1.3.2.1 The X states

- X(3872). The first observed charmonium-like state is the X(3872), which is observed in B meson decay in the decay $B \rightarrow K(X(3872) \rightarrow J/\psi\pi^+\pi^-)$ by Belle [42] and then confirmed by other experiments [43, 44, 45, 46, 47, 48]. However, we still do not fully understand the nature of X(3872) although the huge experimental efforts.

Among the XYZ states, the X(3872) is one of the few charmonium-like states observed in multi decay channels, it was mostly observed in the B meson decay mode $B \rightarrow KX(3872)$ with $X(3872) \rightarrow J/\psi\pi^+\pi^-$, and also produced in $p\bar{p}$ annihilations, pp/ee collisions with decaying into $D^{*0}\bar{D}^0$, $D^0\bar{D}^0\pi^0$, $\gamma J/\psi$, $\gamma\psi(3686)$, and $\omega J/\psi$. Its quantum numbers have been studied by several experiments such as Belle, BaBar, and CDF and finally determined to be $I^G J^{PC} = 0^+1^{++}$ by LHCb experiment in 2013 [49].

The parameters of the X(3872) from the fit to the results reported by different experiments are a mass at (3871.69 ± 0.17) MeV and a width less than 1.2 MeV at 90% C.L. The mass is extremely close to the $D^0\bar{D}^{*0}$ threshold, (3871.81 ± 0.09) MeV.

- X(3823). The BESIII collaboration confirmed the X(3823) resonance in the $\gamma\chi_{c1}$ final state from the process $e^+e^- \rightarrow \pi^+\pi^-\gamma\chi_{c1}$ with a significance of 6.2σ in 2015 [50]. This observation confirmed the study reported by Belle in 2013 [51]. The mass and width were measured to be $M = (3827 \pm 1.3 \pm 0.7)$ MeV and $\Gamma < 16$ MeV at the 90% C.L.

There are two charmonium-like states X(3940) and X(4160) observed through the double charmonium production. The final states of the double charmonium production process include a charmonium-like state plus a J/ψ [52, 53]. The two X states, X(3940) and X(4160), were produced from the following processes:

1. THEORETICAL AND EXPERIMENTAL BASES

$$\begin{aligned} \text{X}(3940) & : e^+e^- \rightarrow J/\psi\bar{D}D^*, \\ \text{X}(4160) & : e^+e^- \rightarrow J/\psi D^{*+}D^{*-}, \end{aligned}$$

- X(3940). The observation of the charmonium-like state X(3940) was first reported by Belle in the process $e^+e^- \rightarrow J/\psi\bar{D}D^*$ with a significance of 5.0σ [52]. The mass and width were measured to be $M = (3943 \pm 6 \pm 6) \text{ MeV}$ and $\Gamma = (15.4 \pm 10.1) \text{ MeV}$, respectively. But there was no evidence of $\text{X}(3940) \rightarrow D\bar{D}$ decay mode. The Belle confirmed the X(3940) with a significance of 5.7σ [53] in next year but still didn't find this state in other decay modes.

- X(4160). The Belle reported the observation of the X(4160) in $e^+e^- \rightarrow J/\psi D^{*+}D^{*-}$ process with a significance of 5.1σ [53]. The mass and width were measured to be $M = (4156_{-20}^{+25} \pm 15) \text{ MeV}$ and $\Gamma = (139_{-61}^{+111} \pm 21) \text{ MeV}$, respectively.

At present, both the X(3940) and X(4160) were only observed by Belle with the significance larger than 5σ , and still need to be confirmed by other experiments.

The $\gamma\gamma$ fusion process $\gamma\gamma \rightarrow X$ produces C -even charmonium states in B factories. The two photons do not couple to any $J = 1$ state, therefore, the $\gamma\gamma$ fusion process can only produce charmonium-like states with quantum numbers such as $I^G J^{PC} = 0^+0^{++}, 0^+2^{++}, \dots$.

$$\begin{aligned} \text{X}(3915) & : \gamma\gamma \rightarrow J/\psi\omega, \\ \text{X}(4350) & : \gamma\gamma \rightarrow J/\psi\phi, \end{aligned}$$

- X(3915). The X(3915) regarded as $\chi'_{c0}(2P)$ was first observed by Belle in $\gamma\gamma \rightarrow J/\psi\omega$ process [54]. The mass and width were measured to be $M = (3915 \pm 3 \pm 2) \text{ MeV}$ and $\Gamma = (17 \pm 10 \pm 3) \text{ MeV}$, respectively. The X(3915) should carry positive C -parity and G -parity according to the $I^G J^{PC} = 0^-1^{--}$ of J/ψ and ω .

Babar confirmed the existence of X(3915) in $\gamma\gamma \rightarrow J/\psi\omega$ process and gave the favored $J^P = 0^+$ of the X(3915) [55].

- X(4350). The Belle collaboration studied the $\gamma\gamma \rightarrow J/\psi\phi$ process and observed a new structure around 4.35 GeV in the $\phi J/\psi$ final state [56]. The mass and width were measured to be $M = (4350.6_{-5.1}^{+4.6} \pm 0.7) \text{ MeV}$ and $\Gamma = (13_{-9}^{+18} \pm 4) \text{ MeV}$, respectively.

1.3.2.2 The Y states

- Y(3940). The charmonium-like state Y(3940) was firstly reported by the Belle collaboration in the $\omega J/\psi$ final state from the $B \rightarrow K\omega J/\psi$ mode in 2004 [57]. The statistical significance is more than 8σ , and the mass and width are measured to be $M = (3943 \pm 11 \pm 13)$ MeV and $\Gamma = (87 \pm 22 \pm 26)$ MeV, respectively. The product of branching fraction is given by Belle as well: $BR(B \rightarrow KY(3940)) \times BR(Y(3940) \rightarrow \omega J/\psi) = (7.1 \pm 1.3 \pm 3.1) \times 10^{-5}$. This observation is confirmed by BaBar collaboration later. The recently measured mass and width for Y(3940) are $M = (3919.1_{-3.5}^{+3.8} \pm 2.0)$ MeV and $\Gamma = (31_{-8}^{+10} \pm 5)$ MeV, respectively [58].

- Y(4140) and Y(4274). The evidence of the Y(4140) was firstly announced by the CDF collaboration in the decay mode $B \rightarrow KJ/\psi\phi$ in $p\bar{p}$ collisions at center of mass 1.96 TeV with an integrated luminosity of 2.7 fb^{-1} and a statistical significance of 3.8σ in 2009 [59]. The structure was not observed in the search of $\gamma\gamma \rightarrow J/\psi\phi$ from Belle [56]. In 2011, the CDF confirmed the Y(4140) using increased $B^+ \rightarrow K^+J/\psi\phi$ sample with a significance greater than 5σ [60], and CDF reported evidence for another structure named as Y(4274). The mass and width of Y(4140) were measured to be $M = (4143.4_{-3.0}^{+2.9} \pm 0.6)$ MeV and $\Gamma = (15.3_{-6.1}^{+10.4} \pm 2.5)$ MeV. The LHCb collaboration searched for the Y(4140) using $B \rightarrow KJ/\psi\phi$ events with an integrated luminosity of 0.37 fb^{-1} in pp collision one year later, but no observation [61].

In 2013, both the D0 and CMS collaborations confirmed the existence of the Y(4140). The D0 studied the $B^+ \rightarrow K^+J/\psi\phi$ process and reported the evidence of Y(4140) at 3.1σ [62]. The CMS studied the $B^\pm \rightarrow K^\pm J/\psi\phi$ process with the data collected in pp collision at $\sqrt{s} = 7$ TeV and got a significance greater than 5σ . The CMS confirmed the existence of the Y(4274) as well [63].

In the e^+e^- annihilation processes, there were five charmonium-like states including the Y(4008), Y(4260), Y(4360), Y(4630), and Y(4660) reported due to the initial-state radiation (ISR) technology. The Y states in charmonium spectrum were found in following decay modes:

$$\begin{aligned} Y(4260) \text{ and } Y(4008) & : e^+e^- \rightarrow \gamma_{\text{ISR}}\pi^+\pi^-J/\psi, \\ Y(4360) \text{ and } Y(4660) & : e^+e^- \rightarrow \gamma_{\text{ISR}}\pi^+\pi^-\psi(3686), \\ Y(4630) & : e^+e^- \rightarrow \gamma_{\text{ISR}}\Lambda_c\bar{\Lambda}_c, \end{aligned}$$

- Y(4260) and Y(4008). The first observation of the Y(4260) was announced by Babar collaboration in 2005 [78] in the process $e^+e^- \rightarrow \gamma_{\text{ISR}}\pi^+\pi^-J/\psi$ using the ISR technique at $\sqrt{s} = 10.58$ GeV. The later confirmations were presented by CLEO [65] and Belle [64] in the same process.

A fit to the Y(4260) resonance yielded the mass and width $M = (4251 \pm 9)$ MeV and $\Gamma = (120 \pm 12)$ MeV. The quantum numbers are $J^{\text{PC}} = 1^{--}$ since the Y(4260) was directly produced from the e^+e^-

1. THEORETICAL AND EXPERIMENTAL BASES

annihilation. The $Y(4260)$ has also the probability to decay into another charmonium-like state, such as the $X(3872)$ (hinted but no observation), the $Z_c(3900)^\pm$ [66, 81].

The resonant structure around the 4.2 GeV was found in several final states from different decay modes, which gives us the possibility to measure the $Y(4260)$ resonance parameters better. The detailed study for this resonance will be introduced in the following chapter.

Besides the $Y(4260)$, Belle reported a hint of another very broad structure called the $Y(4008)$, which comes from the fit to the $\pi^+\pi^-J/\psi$ invariant mass distribution. Babar didn't find such a structure around 4 GeV in the same reaction [67]. The results of the $Y(4008)$ should be clarified in future experiments.

- $Y(4360)$ and $Y(4660)$. After the the observation of $Y(4260)$, Babar collaboration analyzed another ISR process, $e^+e^- \rightarrow \gamma_{\text{ISR}}\pi^+\pi^-\psi(3686)$, that is similar to the $e^+e^- \rightarrow \gamma_{\text{ISR}}\pi^+\pi^-J/\psi$. There is no signature for the $Y(4260)$, but a new structure was observed and named as the $Y(4360)$ [68] in 2007. In the same year, Belle confirmed the observation of the $Y(4360)$ and observed a new resonant structure named as the $Y(4660)$ [68]. Babar didn't confirm the existence of the $Y(4660)$ until 2012 with the larger data sample [70].

The averaged masses and widths of the $Y(4360)$ and $Y(4660)$ provided by different experiments are $M_{Y(4360)} = (4354 \pm 10)$ MeV, $\Gamma_{Y(4360)} = (78 \pm 16)$ MeV, and $M_{Y(4660)} = (4665 \pm 10)$ MeV, $\Gamma_{Y(4660)} = (53 \pm 16)$ MeV. The quantum numbers of the $Y(4360)$ and $Y(4660)$ are $J^{PC} = 1^{--}$ since they are from the e^+e^- annihilation.

For the $Y(4360)$ and $Y(4660)$, the only observed open charm decay mode is the $\pi^+\pi^-\psi(3686)$, the other open charm decay modes such as $D^0D^{*-}\pi^+$ are still missing.

- $Y(4630)$. The $Y(4630)$ was observed by Belle in the cross sections distribution of $e^+e^- \rightarrow \gamma_{\text{ISR}}\Lambda_c\bar{\Lambda}_c$ process in 2008, and the statistical significance is 8.2σ [71]. The mass and width were measured to be $M = (4634_{-7}^{+8} {}_{-8}^{+5})$ MeV and $\Gamma = (92_{-24}^{+40} {}_{-21}^{+10})$ MeV, respectively. The mass is close to the $\Lambda_c\bar{\Lambda}_c$ threshold and is consistent within errors of the $Y(4660)$. Further experiments are needed to determine whether the $Y(4630)$ and $Y(4660)$ are the same structure.

1.3.2.3 The Z states

- $Z(3930)$. The $Z(3930)$ was observed in the $D\bar{D}$ invariant mass spectrum in the process of $\gamma\gamma \rightarrow D\bar{D}$ by Belle in 2005 [79]. The mass and width were measured to be $M = (3929 \pm 5 \pm 2)$ MeV and $\Gamma = (29 \pm 10 \pm 2)$ MeV. This Z state was confirmed by BaBar in 2010 and identified as a tensor state with $J^{PC} = 2^{++}$, the $Z(3930)$ was generally regarded as the $\chi'_{c2}(2P)$ candidate since the mass and width are consistent with the prediction by the potential model.

• $Z^\pm(4430)$. The charged charmonium-like state $Z^\pm(4430)$ was first observed by the Belle in $\pi^\pm\psi(3686)$ invariant mass distribution in $B \rightarrow K\pi^\pm\psi(3686)$ decays in 2007 [72], with a statistical significance of 6.5σ . The mass and width were measured to be $M = (4433 \pm 4 \pm 2)$ MeV and $\Gamma = (45_{-13}^{+18} {}_{-13}^{+30})$ MeV, respectively. This signal was not seen in the BaBar experiment [73].

Belle also performed a full amplitude analysis of $B^0 \rightarrow K^+\pi^-\psi(3686)$ decays to determine the spin and parity of the $Z^-(4430)$. The quantum numbers was measured to be $J^P = 1^+$, this hypothesis being favored over the $0^-, 1^-, 2^-$ and 2^+ at the levels of $3.4\sigma, 3.7\sigma, 4.7\sigma$ and 5.1σ , respectively.

The LHCb collaboration confirmed the existence of the $Z^-(4430)$ by performing a four-dimensional fit in the analysis of the $\pi^-\psi(3686)$ invariant mass distribution in the $B^0 \rightarrow K^+\pi^-\psi(3686)$ decay [74]. The mass and width of $Z^+(4430)$ were measured to be $M = (4475 \pm 7_{-25}^{+15})$ MeV and $\Gamma = (172 \pm 13_{-34}^{+37})$. The LHCb also established the spin-parity of $Z^+(4430)$ to be $J^P = 1^+$ and ruled out the $0^-, 1^-, 2^+$ and 2^- hypotheses by at least $9.7\sigma, 15.8\sigma, 16.1\sigma$ and 14.6σ , respectively.

• $Z^+(4051)$ and $Z^+(4248)$. These two charged charmonium-like states were first observed by Belle in the $\pi^+\chi_{c1}$ final state in 2008 [75]. The masses and the widths were measured to be $M_{Z^+(4051)} = (4051 \pm 14_{-41}^{+20})$ MeV, $\Gamma_{Z^+(4051)} = (82_{-17}^{+21} {}_{-22}^{+47})$ MeV and $M_{Z^+(4248)} = (4248_{-29}^{+44} {}_{-35}^{+180})$ MeV, $\Gamma_{Z^+(4248)} = (177_{-39}^{+54} {}_{-61}^{+316})$ MeV, respectively.

Neither of these two states was confirmed by BaBar in the $\pi^+\chi_{c1}$ mass spectrum from $\bar{B}^0 \rightarrow K^-\pi^+\chi_{c1}$ and $B^+ \rightarrow K_S^0\pi^+\chi_{c1}$ decay modes [76]. The upper limits on the branching fractions at 90% C.L. were set and are consistent with the Belle results.

• $Z^+(4200)$ and $Z^+(4240)$. Belle reported the observation of a new charged charmonium-like structure $Z^+(4200)$ [77] in the π^+J/ψ decay final state with a significance of 6.2σ . The mass and width were measured to be $M = (4196_{-29}^{+31} {}_{-13}^{+17})$ MeV and $\Gamma = (370_{-70}^{+70} {}_{-132}^{+70})$ MeV, respectively. The $Z^+(4200)$ is a broad structure and favors $J^P = 1^+$.

The LHCb also reported the observation of a new structure $Z^-(4240)$ [74] in the $\pi^-\psi(3686)$ final state from the decay mode $B^0 \rightarrow K^+\pi^-\psi(3686)$ with a significance of 6σ . The mass and width were measured to be $M = (4239 \pm 18_{-10}^{+45})$ MeV and $\Gamma = (220 \pm 47_{-74}^{+108})$ MeV, respectively. The $Z^-(4240)$ favors $J^P = 0^-$ over $1^-, 2^-$ and 2^+ by 8σ but 1^+ only by 1σ , which means the $J^P = 1^+$ is not fully excluded.

There are three charged charmonium-like structures around 4.2 GeV were observed through B-meson decays, the $Z^+(4200)$, $Z^+(4240)$ and $Z^+(4248)$. More precise experimental studies are needed, especially the spin-parity quantum numbers, to further clarify the above charged charmonium-like states.

1. THEORETICAL AND EXPERIMENTAL BASES

The charged charmonium-like states from the hadronic decays of the $Y(4260)$ and higher charmonia will be introduced in this sub section. There are four charged charmonium-like states listed below:

$$\begin{aligned} e^+e^- &\rightarrow Z_c(3900)\pi^\mp \rightarrow J/\psi\pi^\pm\pi^\mp, \\ e^+e^- &\rightarrow Z_c(4025)\pi^\mp \rightarrow (D^*\bar{D}^*)^\pm\pi^\mp, \\ e^+e^- &\rightarrow Z_c(4020)\pi^\mp \rightarrow h_c\pi^\pm\pi^\mp, \\ e^+e^- &\rightarrow Z_c(3885)\pi^+ \rightarrow (D\bar{D}^*)^-\pi^+, \end{aligned}$$

- $Z_c(3900)$ and $Z_c(3885)$. The $Z_c(3900)$ and the $Z_c(3885)$ were observed in process $Y(4260) \rightarrow \pi^- Z_c^+$ by BESIII collaboration [81, 82]. The $Z_c(3900)$ state was also observed by Belle at the same time [66].

The quantum numbers of the $Z_c(3900)$ were argued to be $I^G J^P = 1^+ 1^+$ assuming the orbital angular momentum between the J/ψ and π is zero.

The $Z_c(3885)$ was observed in $Y(4260) \rightarrow (D\bar{D}^*)^\pm\pi^\mp$ processes by BESIII with a significance greater than 10σ . If we consider the $Z_c(3900)$ and $Z_c(3885)$ as the same state, this Z state was observed in both the hidden-charm and open-charm decay channels, and the ratio of the partial decay widths of these two decay modes was measured as

$$\frac{\Gamma(Z_c(3885) \rightarrow DD^*)}{\Gamma(Z_c(3900) \rightarrow J/\psi\pi)} = (6.2 \pm 1.1 \pm 2.7).$$

under this assumption.

The neutral partner of the charged $Z_c(3900)$ was discovered by BESIII in the $\pi^0\pi^0 J/\psi$ final state with a significance of 10.4σ [83]. The $Z_c(3885)$ was observed in the $e^+e^- \rightarrow (D\bar{D}^*)^0\pi^0$ process as well [84].

- $Z_c(4025)$ and $Z_c(4020)$. The charged charmonium-like structure $Z_c(4020)$ was observed by BESIII in the process $e^+e^- \rightarrow \pi^+\pi^-h_c$ [86]. Another state $Z_c(4025)$ state was firstly observed in the process $e^+e^- \rightarrow \pi^\pm(D^*\bar{D}^*)^\mp$ by BESIII in 2014 as well [85]. The mass of the $Z_c(4025)$ state is very close to that of the $Z_c(4020)$ while the $Z_c(4025)$ is much broader than the $Z_c(4020)$. The quantum number of these two Z_c states are probably $I^G J^P = 1^+ 1^+$ [87].

1.3.2.4 The pentaquark states

In 2015, the LHCb collaboration reported the observation of two exotic structures in the invariant mass distributions of $J/\psi p$ from the process $\Lambda_b^0 \rightarrow J/\psi K^- p$, denoted as the $P_c(4380)^+$ and $P_c(4450)^+$, with the data of pp collision corresponding to 1 fb^{-1} at 7 TeV and 2 fb^{-1} at 8 TeV. The statistical significance are 9σ for the $P_c(4380)^+$ and 12σ for the $P_c(4450)^+$.

The masses and widths of these two states were measured to be:

$$\begin{aligned}
 M_{P_c(4380)^+} &= (4380 \pm 8 \pm 29) \text{ MeV} \\
 \Gamma_{P_c(4380)^+} &= (205 \pm 18 \pm 86) \text{ MeV} \\
 M_{P_c(4450)^+} &= (4449.8 \pm 1.7 \pm 2.5) \text{ MeV} \\
 \Gamma_{P_c(4450)^+} &= (39 \pm 5 \pm 19) \text{ MeV}
 \end{aligned}$$

The $P_c(4380)^+$ and $P_c(4450)^+$ states preferred the $J^P = 3/2^-, 5/2^+$ but some other combinations are only slightly less favored such as $(3/2^+, 5/2^-)$ and $(5/2^+, 3/2^-)$. All the other combinations ($1/2^\pm$ to $7/2^\pm$) were ruled out.

These two states must have minimal quark contents $c\bar{c}uud$ according to the final state $J/\psi p$, and thus are good candidates of exotic hidden-charm pentaquarks. The further confirmation on these two P_c states from other experiments are needed.

1.3.2.5 A short summary of charmonium-like states

The number of observed charmonium-like states is much more than the prediction according to the potential model. In another hand, many theories are trying to interpret one or few charmonium-like states as the molecular scheme, the tetraquark, the result of a kinematical effect, the radial excitation, the hybrid charmonium, or the bound states and so on.

The further data from the experiments such as BESIII, LHCb, PANDA [89], CMS will help to study more interesting parameters of those observed XYZ states, and to search for the XYZ states in a wider range of decay modes. This enables a systematic study of the XYZ and charmonium states with a new level of precision.

1.3.2.6 Y states at 4.2 GeV in BESIII experiment

The Y-states from the ISR process shows strong coupling to hidden-charm final states in contrast to the vector charmonium states in the same energy region which couples dominantly to open-charm meson pairs. These Y states are good candidates for new types of exotic particles and the predicated particles by some theories [90].

The Y(4260) is the first observed and most interesting Y state, there are some theoretical interpretations for the Y(4260):

- The hybrid charmonium.

The author of Ref. [91] preferred to conclude the Y(4260) as a candidate of the charmonium hybrid state according to QCD sum rule calculations [92, 93] and flux tube model analysis [94, 95], while the final states with one S-wave meson and one P-wave meson are potentially important. Such a

1. THEORETICAL AND EXPERIMENTAL BASES

decay pattern is consistent with the experimental data of the $Y(4260)$ meson, in which the open-charm $D\bar{D}$ decay mode was not observed.

This charmonium hybrid interpretation was also supported or allowed in some other discussions [96, 97, 98].

- Tetraquark state.

The interpretations of tetraquark in Ref. [99] proposed the $Y(4260)$ as the first orbital excitation of a diquark-antidiquark state $[cs][\bar{c}\bar{s}]$ and predicted the decay mode in $D_s\bar{D}_s$ and in B non-leptonic decays in association with a kaon [100]. Besides, a predicted mass of $M_Y = (4330 \pm 70)$ MeV for the $Y(4260)$ was given in Ref. [101]

There are some other tetraquark studies reported in Refs. [102, 103, 104, 105] with different models.

- Molecules state.

There are several molecular interpretations for the $Y(4260)$ state. The $Y(4260)$ was interpreted as an $\omega\chi_{c1}$ molecular in Ref. [106], was studied in the framework of the meson exchange model in Ref. [107], was suggested as a spectroscopy of quasi-molecular states due to the strong S-wave pion exchange effects in Refs. [108, 109], and was interpreted as a $D_1\bar{D}$ molecule in Ref. [110].

- Non-resonant explanations.

According to the idea that the form factor strongly suppresses open channels far above the threshold discussed in Ref. [111], the fit on $Y(4260)$ obtained a good result with a simple nonresonant cusp structure around the $D_s^*\bar{D}_s^*$. In Ref. [112], the $Y(4260)$ structure was reproduced well when proposed a non-resonant explanation and considered the interference of the production amplitudes of the e^+e^- annihilation process and through intermediate charmonia $\psi(4160)/\psi(4415)$. This interpretation can naturally answer the issue of why no evidence of $Y(4260)$ in exclusive open-charm decay channels [113, 114, 115].

Recently, the BESIII experiment reported a series of studies on the new data with the energy up to 4.6 GeV, and found candidates of $Y(4260)$ in four different decay modes:

$$\begin{aligned} e^+e^- &\rightarrow \pi^+\pi^-\text{h}_c \text{ [86, 171]}, \\ e^+e^- &\rightarrow \omega\chi_{c0} \text{ [168, 172]}, \\ e^+e^- &\rightarrow \pi^+\pi^-J/\psi \text{ [173]}, \\ e^+e^- &\rightarrow D^0D^{*-}\pi^+ + \text{c.c} \text{ [174]}, \end{aligned}$$

Each cross section distribution of the channel hints a $J^{PC} = 1^{--}$ resonant signature at around 4.2 GeV that has the mass and width compatible with others. There is no evidence that can clarify whether these Y states are one charmonium-like state, which was called $Y(4260)$ but now we will call it $Y(4220)$ because of improved measurement of the resonant parameters from BESIII. If we try a simultaneous fit on these four cross sections with the assumption that they are one Y state in four

decay modes, we can give more precise resonant parameters due to the higher statistics that would help to understand the properties of $Y(4220)$.

1.4 Particle physics experiment

To understand the properties of a particle we need to see how it interacts with other particles. The typical experiment in nuclear or particle physics involves firing a projectile at a target and then collecting the information from the final stable particles. The stable means the particle can fly a distance before decaying to other particles so that the detectors can detect them.

Generally, the smaller the size of the object we want, the higher energy is needed, in order to overcome the binding energy and take them apart. At the atom level, there is only very low energy needed, around $\sim \text{KeV}$, but if we go to the nucleus level, the binding energy goes up to MeV rapidly. In another hand, there are many reactions interested in particle physics that only occur at high energy but the high energy cosmic rays give quite low statistics, we, therefore, need to build accelerators.

To accelerate the beam of particles, they will need to have interactions with an external field. The only forces which are active over macroscopic length scales are the electromagnetic and gravitational forces. However the gravitational force on subatomic particles is much smaller than the electromagnetic ones, thus the only way to change the momenta of particles is the electromagnetic force. The particles have to be charged to get acceleration from the electromagnetic forces. The electrons that are pulled off from cathode or the protons that are created from kicking the electrons off Hydrogen atom are the most common candidate particles of the beam.

The circular accelerator can provide high energy beams more easily than the linear accelerator since the particles can stay in the ring and be accelerated again and again. It is very difficult to get TeV -scale energies from linear acceleration, which would require constant acceleration over distances of order $\sim 10^4$ m.

There is also a limit on the energy of circular accelerators. The particles blended by the magnetic field will lose energy through the synchrotron radiation at the order of $\sim 1/m^4$, where m is the mass of the blended particle.

The electron-positron circular collider can provide much clean final states, however, it is hard to push energy up because of the synchrotron radiation. On the other hand, the proton-proton circular collider can provide quite high energy beams but with many final state particles from the hadronization of quarks.

The final particles from the collision can be detected by the dedicated designed detectors. Different particles leave different signatures in the detectors because of their properties. General-purpose particle detectors at colliders generally have a series of different layers surrounding the interaction point. The inner part of the detector is used to track the trajectory of charged particles and measure their momenta as they bend in an externally applied magnetic field. Beyond the tracker are layers of calorimeter which are designed to stop the particles and convert their energies into electrical signals.

1. THEORETICAL AND EXPERIMENTAL BASES

Electromagnetic calorimeters rely on cascades caused by sequential Bremsstrahlung and pair creation in the electromagnetic field of an atomic nucleus, the electromagnetic calorimeters are effective at detecting electrons and photons. Hadronic calorimeters lie beyond the electromagnetic calorimeters and are used to measure the energies of the long-lived baryons and mesons. The hadrons interact with the atomic nuclei via the strong interaction, producing inelastic scattering reactions. The final layer in the detector is usually a muon tracker. Muons are highly penetrating, and are the only particles to pass through the calorimeters. Most large muon detectors work by measuring the ionization caused in a gas by the passage of the muon.

There are some high energy physics experiment collaborations around the world, working on the data collected by the accelerators and detectors. They usually analyze the data with different purposes depending on the properties of the hardware. Such as searching for new physics at high mass range using proton-proton high energy circular collider, making a precise measurement on observed particles using electron-positron collider.

The large hadron collider (LHC) and the detector Compact Muon Solenoid (CMS) are good examples of typical collider and detector. The LHC and CMS will be introduced briefly in the following sections.

1.4.1 The Large Hadron Collider (LHC)

As the world's largest and most powerful particle accelerator, the Large Hadron Collider (LHC) was built by the European Organization for Nuclear Research (CERN) between 1998 and 2008 on the France-Swiss border and first started up on 10th September 2008.

It runs about 100 meters underground with the 27 kilometers circumference.

The LHC provides pp collisions at the center-of-mass 13 TeV. There are four main experiments at LHC as shown in figure 1.4, two general-purpose detectors, the CMS and ATLAS, which investigate many different types of physics in order to improve the understanding of Standard Model or search for the clues of new physics. One detector ALICE was built for heavy-ion collisions and focuses on the physics of strongly interacting matter at extreme energy densities. The last detector, LHCb, focuses on the physics programs of heavy flavor in particular the study of B mesons, electroweak and QCD.

1.4.2 The Compact Muon Solenoid (CMS)

The central feature of the CMS detector is a superconducting solenoid providing an axial magnetic field of 3.8 Tesla and enclosing an inner tracker, an electromagnetic calorimeter (ECAL), and a hadron calorimeter (HCAL). The inner tracker is composed of a silicon pixel detector and a silicon strip tracker, and measures charged particle trajectories in the pseudorapidity range $|\eta| < 2.5$. The ECAL and HCAL, each composed of a barrel and two endcap sections, extend over the range $|\eta| < 3.0$. The finely segmented ECAL consists of nearly 76,000 lead tungstate crystals, while the HCAL is constructed from alternating layers of brass and scintillator. Forward hadron calorimeters encompass $3.0 < |\eta| < 5.0$. The muon detection system covers $|\eta| < 2.4$ with up to four layers of gas-ionization

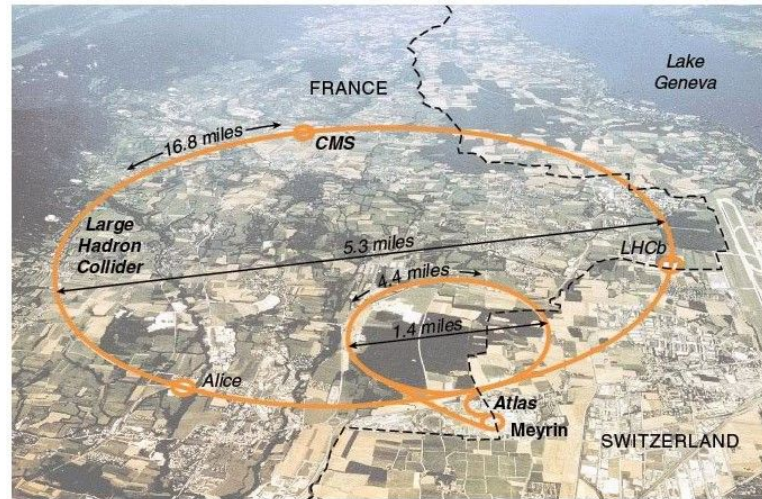


Figure 1.4: The LHC and the correlated detectors

detectors installed outside the solenoid and sandwiched between the layers of the steel flux-return yoke. The overview of CMS is shown in figure 1.5.

1.4.2.1 Superconduction magnet

The superconducting solenoid magnet for CMS is the largest superconducting magnet ever built, and the CMS's heaviest component. It has a diameter of 6 m and a length of 12.5 m. The magnet provides a very strong field of 3.8 Tesla, that bends the trajectories of particles in order to identify the charge and to measure the momentum.

1.4.2.2 Inner tracking system

The inner tracking system is designed to provide a precise and efficient measurement of trajectories of charge particles from LHC beam collision, and precise reconstruction of primary and secondary vertices (from b and τ decays). The CMS tracker is composed of a pixel detector with three barrel layers and a silicon strip tracker with 10 barrel layers outwards. The pixel system is the closest to the interaction region and is essential for the reconstruction of secondary vertices. The CMS tracker is completed with endcaps of two disks in the pixel detector and 3 plus 9 disks in the strip tracker to extend the tracker coverage up to $|\eta| < 2.4$. There are 1440 pixel and 15148 strip detector modules for the CMS tracker in total.

In the extended end-of-year shutdown during winter 2016/2017, the pixel detector was replaced by a new one because of the radiation damage and high occupancy in the readout chip. The main new features of the upgraded pixel detector are an ultra-light mechanical design with four barrel layers and three end-cap disks, digital readout chip with higher rate capability and a new cooling system in order to maintain the excellent tracking and other physics performances.

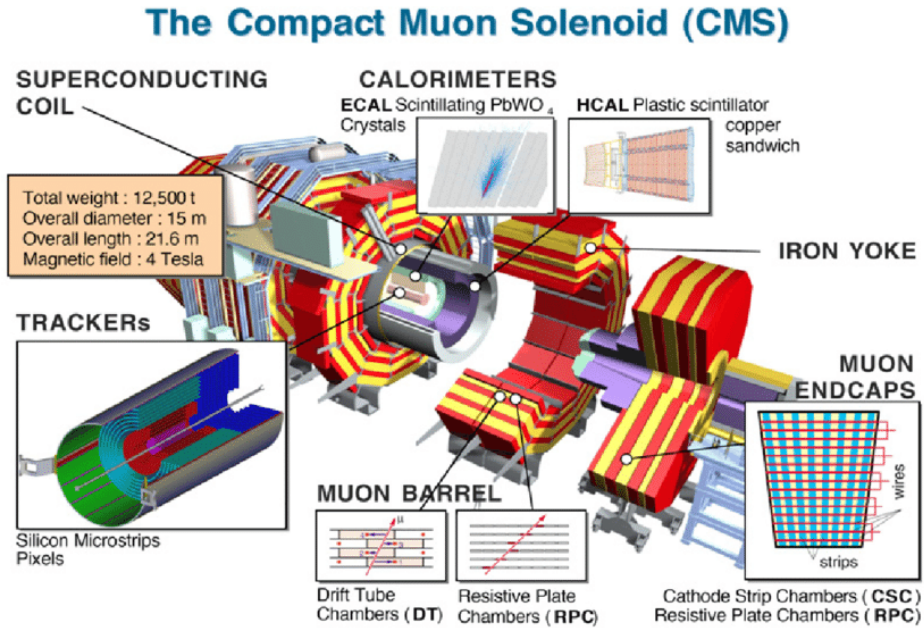


Figure 1.5: The CMS detector

1.4.2.3 Electromagnetic calorimeter

The Electromagnetic Calorimeter (ECAL) is designed to identify electrons and photons. Since most of the energies of electrons and photons are deposited within the ECAL, the ECAL can give measurement with very good resolution on their energy. The ECAL is a hermetic homogeneous calorimeter made of 61200 lead tungstate (PbWO_4) scintillating crystals mounted in the central barrel part, closed by 7324 crystals in each of the 2 endcaps, and one pre-shower detector in front of the endcap crystals. The blue-green scintillation light emitted by the crystals is detected by the photo detectors of silicon avalanche photodiodes (APDs) in the barrel and vacuum phototriodes (VPTs) in the endcaps.

The barrel (EB) and endcaps (EE) parts of the ECAL cover the pseudorapidity range $|\eta| < 1.479$ and $1.479 < |\eta| < 3.0$. The EB(EE) are filled with crystals with volume of $8.14(2.90) \text{ m}^3$ and weight of $67.4(24.0) \text{ t}$.

The pre-shower detector covers the pseudorapidity range $1.653 < |\eta| < 2.6$, which is designed to identify π^0 in the endcaps and electrons against minimum ionizing particles. The pre-shower detector can also help to improve the position determination of electrons and photons.

1.4.2.4 Hadron calorimeter

The Hadron Calorimeter (HCAL) is an important component to measure the energy of charged or neutral hadrons, that surrounds the ECAL system. The HCAL is designed with maximum material inside in order to minimize the non-Gaussian tails in the energy resolution and to provide good

containment and hermeticity for the E_T^{miss} measurement. The HCAL system uses brass as absorber material due to the short interaction length and non-magnetic properties.

In order to build the HCAL without dead areas in ϕ , and cover big enough pseudorapidity, the HCAL system is composed of barrel calorimeter (HB), endcap calorimeter (HE), hadron outer detector (HO) and forward hadron calorimeter (HF).

1.4.2.5 Muon Detector

The muon system is designed with the purpose of identifying muons, measuring their momenta and providing information for event triggering. It is composed of three types of detectors, the drift tubes (DT), the cathode strip chambers (CSC) and the resistive plate chambers (RPC). The DT and the CSC provide the measurement of charged particle momentum with a good spatial resolution. The DT are used in the barrel and the CSC are used in the endcap. The RPC have good timing and thus are used for trigger issues. There are four muon stations in the barrel part of muon system (MB), cover $|\eta| < 1.2$ and four muon stations per endcap (ME), cover $|\eta|$ up to 2.4.

The tracker measurements dominate the resolution for low momenta muons when the momenta of muons go up to around 1 TeV, the momentum resolutions are from both the tracker and the muon system at around 5%.

1.4.2.6 Trigger System

The CMS experiment has been designed with a 2-level trigger system: the Level 1 Trigger (L1), implemented on custom-designed electronics, and the High Level Trigger (HLT), a streamlined version of the CMS offline reconstruction software running on a computer farm [135].

The role of the trigger in a High Energy Physics experiment is to reduce the rate of recorded collisions to a level that is manageable by the following Data Acquisition (DAQ) and reconstruction steps. At LHC the proton beams are organized in bunches. Those bunches were interleaved by 50 ns during the Run1 period and 25 ns at Run2. The maximum acceptable rate for data acquisition and storage is of the order of 1 kHz, and the trigger must be designed to reduce the rate to that level, by accepting the largest possible cross-section of the interesting physics events from the collisions and rejecting efficiently the non-interesting ones.

With the beginning of the LHC Run 2, the CMS experiment has to cope with harsher operating conditions: higher center-of-mass energy of 13 TeV, reading to an enhancement of the production cross section of interesting processes like weak boson and top quark production, and larger occurrence of multiple proton-proton interactions in the same/near bunch crossings (pile-up), ranging from 20 to 60 simultaneous interactions. The High-Level Trigger software has been optimized for these conditions, balancing a high selection efficiency on signal events while keeping the output rate at acceptable levels both for the online data acquisition system and the offline prompt reconstruction center.

1.4.2.7 Electron reconstruction in CMS

The reconstruction of electrons in CMS uses information from the pixel detector, the silicon strip tracker and the electromagnetic calorimetry (ECAL).

The track reconstruction procedure in CMS is described in the following steps. Firstly, a seed is created when two hits compatible with a given beam spot are found in the pixel detector, in order to build a track outward. Then a trajectory is created starting from given seed. The hits outward are searched for until the last tracker layer. All possible trajectories are built and a minimum of five hits is finally required to create a track. Finally, the final fit of the track is performed with the Trajectory Smoother, which uses all the collected hits to estimate the track parameters at each layer through a backward fit. In order to better deal with the non-Gaussian fluctuations induced by bremsstrahlung emission, dedicated algorithms have been developed for the seeding and building steps, as well as for the smoothing step where a Gaussian Sum Filter (GSF) is used instead of the standard Kalman Filtering both for forward and the backward fits.

1.4.2.8 Muon reconstruction in CMS

The muon reconstruction starts to build a trajectory from a start point, called seed, where hits in muon system are found. The track is then extended in the direction specified by the seed to locate compatible hits on the subsequent detector layers. A combinatorial Kalman filter with full knowledge of the track parameters at each detector layer is used in the track finding and fitting. All candidate trajectories are kept and then the ambiguities among the possible trajectories are resolved in the clean stage.

There are three kinds of reconstructions for muon:

- Stand-alone reconstruction: this just uses hits in the muon detectors
- Global Reconstruction: this starts with the muon segment information and then adds tracker information
- Tracker Muon reconstruction: this starts with tracks found in the inner tracker and identifies them as muon by matching expected information from the calorimeters and muon system.

A more detailed description of the CMS detector can be found in Ref. [116].

1.5 Variable definitions

- pseudorapidity, η

In experimental particle physics, pseudorapidity, η , is a commonly used spatial coordinate describing the angle of a particle relative to the beam axis. It is defined as:

$$\eta = -\ln\left[\tan\left(\frac{\theta}{2}\right)\right]$$

where θ is the angle between the particle three-momentum \mathbf{p} and the positive direction of the beam axis. The pseudorapidity can be also written as function of \mathbf{p} :

$$\eta = \frac{1}{2} \ln\left(\frac{|\mathbf{p}| + p_z}{|\mathbf{p}| - p_z}\right) = \operatorname{arctanh}\left(\frac{p_z}{|\mathbf{p}|}\right)$$

The rapidity is Lorentz invariant under boosts along the longitudinal axis, which is defined as:

$$y = \ln\left(\frac{\sqrt{m^2 + p_T^2} \cosh^2 \eta + p_T \sinh \eta}{\sqrt{m^2 + p_T^2}}\right)$$

where $p_T = \sqrt{p_x^2 + p_y^2}$, in the limit where the particle is travelling close to the speed of light, or equivalently in the approximation that the mass of the particle is negligible, one can make the substitution:

$$m \ll |\mathbf{p}| \Rightarrow E \approx |\mathbf{p}| \Rightarrow \eta \approx \text{rapidity}$$

The η is preferred than angle θ in hadron collider physics, where the colliding partons carry different longitudinal momentum fractions, which means that the rest frames of the parton-parton collisions will have different longitudinal boosts.

- ϕ

The angle of particle trajectory in the x-y plane.

- p_T, E_T

The T means transverse, the fraction in the x-y plane of momentum or energy of the object, which is perpendicular to the beam direction.

- E_T^{miss}

The missing transverse energy of the selected object. Missing energy refers to the energy that is not detected in a particle detector, but is expected due to the laws of conservation of energy and conservation of momentum. Missing energy is carried by particles that do not interact with the electromagnetic or strong forces and thus are not easily detectable, most notably neutrinos.

1. THEORETICAL AND EXPERIMENTAL BASES

Chapter 2

Search for lepton flavor violation processes in electron-muon final states with CMS 2016 data

In the Standard Model of particle physics, lepton flavor is conserved, but there is no associated symmetry to support this in the SM. The observation of the lepton flavor violating (LFV) process would be an evidence of physics beyond the SM. There are numerous theories in which LFV processes are incorporated, such as an R-parity violating SUSY model [1], a Quantum Black Hole model [117, 118], the heavy Z' predicted by various grand unified theories [119]. These models have been described in Section 1.2.2. The LFV decay of a heavy state into an $e\mu$ pair would be a clear signature that might be observable at the LHC.

2.1 Data and simulation samples

2.1.1 Data

This analysis is based on the data corresponding to an integrated luminosity of 35.9 fb^{-1} collected in proton-proton (pp) collisions at the energy of 13 TeV in the CMS detector at the CERN LHC.

2.1.2 RPV, Z' , and QBH signal samples

The RPV SUSY $\tilde{\nu}_\tau$, Z' , and QBH signal events are generated at leading order (LO) precision, using the CALCHEP 3.6 [120], PYTHIA 8.203 [121], and QBH 2.0 [122] Monte Carlo (MC) generators, respectively. All simulated signal events use PYTHIA for hadronization and CUETP8M1 provides the underlying-event tune [123]. The RPV and QBH signal events are generated with the CTEQ6L [124] parton distribution functions (PDF) while the Z' boson signal events are simulated using the NNPDF 3.0 PDF sets [125]. The relative width of the Z' signal is taken as 3% of its mass, and interference between the SM Z and Z' bosons is ignored. The LO RPV SUSY $\tilde{\nu}_\tau$ signal event yield is normalized to a next-to-leading order (NLO) calculation of the production cross section; in this calculation, the

2. SEARCH FOR LEPTON FLAVOR VIOLATION PROCESSES IN ELECTRON-MUON FINAL STATES WITH CMS 2016 DATA

factorization and renormalization scales are set to the mass of the $\tilde{\nu}_\tau$. The generated signal events are processed through a full simulation of the CMS detector based on GEANT4 [126, 127, 128], and weighted according to the number of interactions per bunch crossing to match with data. The simulated signal event samples are normalized to the integrated luminosity of the data. The products of the total acceptance and efficiency for the three signal models in this analysis are determined through MC simulation. The corrections of object reconstruction and trigger efficiencies are considered to match with the values measured in data. The selection efficiencies for the RPV $\tilde{\nu}_\tau$, Z' , and QBH signals are $\approx 60\%$, 60% , and 55% when the resonance mass or mass threshold is 1 TeV and $\approx 66\%$, 64% , and 63% when the resonance mass or mass threshold is 4 TeV, respectively.

2.1.3 SM background samples

The SM backgrounds contributing to the $e\mu$ final state are divided into two categories. The first category comprises events with at least two real, isolated leptons; while the second category comprises events that include either jets or photons, misidentified as isolated leptons, or jets with leptons from heavy-flavor decays, both are referred as fake background. The background from the first category is estimated based on Monte Carlo (MC) simulation, while the jet faking electron background is estimated from data and cross-checked with MC.

The expected SM background from processes with two real leptons consists mostly of events from $t\bar{t}$ or WW production. The $t\bar{t}$ process is dominant at lower masses and the WW process becomes equally important above $M_{e\mu} \approx 1$ TeV. Other real lepton backgrounds estimated from MC simulation involve diboson contributions from WZ and ZZ events, single top quark production, and Drell-Yan production in the $\tau\tau$ channel.

The $t\bar{t}$ simulated events are generated with POWHEG generator, in various mass points in order to get enough statistic. The events in single top, Drell-Yan, Diboson processes are generated with POWHEG [129, 130, 131] or GRAPH5_aMC@NLO 2.2.2 [132, 133] generator as well. The Wjets and QCD samples are produced by MADGRAPH and PYTHIA 8, respectively.

2.2 Event selection

The selection is split into three parts and the efficiencies of each part are determined separately. The combination of these individual efficiencies and the acceptance would give the final acceptance times efficiency. The three parts are the reconstruction, the identification + isolation, and the trigger. The efficiencies on the level of the object are all determined on RPV signal samples, and effects due to different acceptances are considered for each signal separately.

2.2.1 Electron reconstruction

Electrons are reconstructed using standard CMS algorithms described in Ref. [137]. The section 1.4.2.7 has already introduced how to reconstruct an electron candidate. The efficiency of reconstruction is defined as:

$$\epsilon_{\text{reco}} = \frac{N(\text{Reconstructed } l)}{N(\text{generated } l)} \quad (2.1)$$

where the reconstructed l is matched to generator level l within $\Delta R < 0.5$.

2.2.2 Electron identification and isolation

The electron candidate must pass the high-energy electron pairs (HEEP) selection, which includes requirements of identification (ID) and isolation (ISO):

- The clusters in ECAL are combined in a way consistent with bremsstrahlung emission, to produce “supercluster” for an electron candidate. The η of supercluster (η_{SC}) and the missing transverse energy ($E_{\text{T}}^{\text{miss}}$) are used for acceptance selection.
- The energy deposition of an electron candidate in the ECAL must be dominant comparing to the sum energy in the HCAL within a cone of $\Delta R = 0.15$.
- The electron candidate must have a well-matched, prompt track in the $\eta - \phi$ plane that has no more than one hit missing in the inner portion of the tracker.
- Cut of an energy-weighted spread value, $\sigma_{\text{in}\eta}$ is applied to endcap electron, which can help to separate electron from jet.
- The energy in the narrow strip ($E_{1 \times 5}$ or $E_{2 \times 5}$) must be higher enough than energy in the wider one ($E_{5 \times 5}$) to suppress hadronic jet.
- The transverse impact parameter relative to the primary vertex must be less than 0.2 (0.5) cm for the electron in calorimeter barrel (endcap).
- The isolation in calorimeter (EM + had depth 1) is required to be less than a value as functions of both E_{T} and pile-up ρ .
- The scalar- p_{T} sum of tracks within a cone of radius $\Delta R = 0.3$ around the candidate direction, excluding the candidate’s track, is less than 5 GeV.

The detailed values of the selections above could be found in Table 2.1.

The ID + ISO efficiency is defined as:

$$\epsilon_{\text{HEEP ID}} = \frac{N(\text{Reconstructed } l + \text{ID} + \text{ISO})}{N(\text{Reconstructed } l)} \quad (2.2)$$

The plot in figure 2.2 shows electron reconstruction and ID + ISO efficiencies as a function of generated electron E_{T} .

Since highly energetic muons can produce bremsstrahlung in the ECAL along the direction of the inner-muon trajectory, such muons can be misidentified as electrons. An electron candidate is therefore rejected if there is a muon candidate with p_{T} greater than 5 GeV whose track has $\Delta R < 0.1$ relative to the electron candidates’ track.

2. SEARCH FOR LEPTON FLAVOR VIOLATION PROCESSES IN ELECTRON-MUON FINAL STATES WITH CMS 2016 DATA

Variable	Barrel	Endcap
Acceptance selections		
E_T	$E_T > 35 \text{ GeV}$	$E_T > 35 \text{ GeV}$
η	$ \eta_{SC} < 1.4442$	$1.566 < \eta_{SC} < 2.5$
Identification selections		
isEcalDriven	true	true
$\Delta\eta_{in}^{seed}$	$ \Delta\eta_{in}^{seed} < 0.004$	$ \Delta\eta_{in}^{seed} < 0.006$
$\Delta\phi_{in}$	$ \Delta\phi_{in} < 0.06$	$ \Delta\phi_{in} < 0.06$
H/E	$H/E < 1/E + 0.05$	$H/E < 5/E + 0.05$
$\sigma_{i\eta i\eta}$	-	$\sigma_{i\eta i\eta} < 0.03$
$\frac{E_{1\times 5}}{E_{5\times 5}}, \frac{E_{2\times 5}}{E_{5\times 5}}$	$\frac{E_{1\times 5}}{E_{5\times 5}} > 0.83$ or $\frac{E_{2\times 5}}{E_{5\times 5}} > 0.94$	-
Inner lost layer hits	lost hits ≤ 1	lost hits ≤ 1
Impact parameter, d_{xy}	$ d_{xy} < 0.02$	$ d_{xy} < 0.05$
Isolation selections		
EM + had depth 1	$iso < 2 + 0.03E_T + 0.28\rho$	$iso < 2.5 + 0.28\rho$ ($E_T < 50 \text{ GeV}$)
isolation, iso		else $iso < 2.5 + 0.03(E_T - 50 \text{ GeV}) + 0.28\rho$
p_T isolation (V7), isopt	isopt $< 5 \text{ GeV}$	isopt $< 5 \text{ GeV}$

Table 2.1: Definitions of HEEP ID V7.0 selection in barrel and endcap region.

2.2.3 Muon reconstruction

Muons are reconstructed using standard CMS algorithms described in Ref. [136]. The section 1.4.2.8 has already introduced how to reconstruct a muon candidate. The efficiency of reconstruction is defined as:

$$\epsilon_{reco} = \frac{N(\text{Reconstructed } l)}{N(\text{generated } l)} \quad (2.3)$$

where the reconstructed l is matched to generator level l within $\Delta R < 0.5$.

The left plot in figure 2.2 shows muon reconstruction efficiency as a function of p_T of the generated muon. While the right one presents a scatter plot for muon reconstruction efficiency inside the acceptance region as a function of muon η and muon ϕ .

2.2.4 Muon identification and isolation

In order to select good and clean enough muon, the reconstructed muon is required to pass the acceptance requirement and the high- p_T muon selection, the detailed cut values are listed as following:

- The muon candidate should have $p_T > 53 \text{ GeV}$ and $|\eta| < 2.4$.
- The hit information in the inner-tracker detector and in the outer-muon system are combined and fitted to obtain the global-muon.

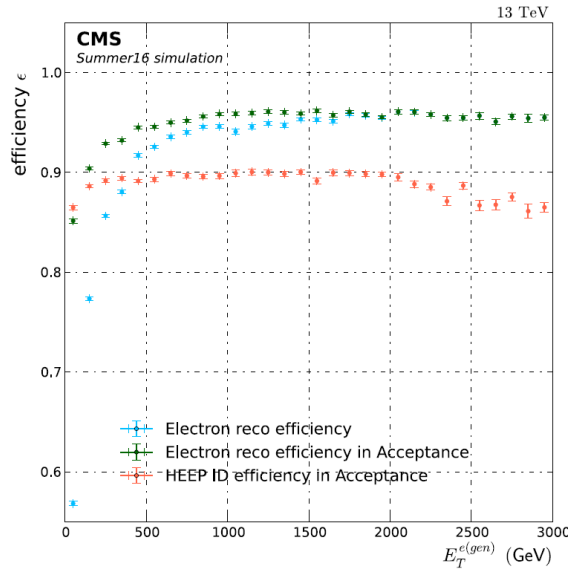


Figure 2.1: Electron reconstruction and ID + ISO efficiencies as a function of generated electron E_T . [134]

- Muon segments should be present in at least two muon stations. This implies that the muon is also a tracker muon and makes the selection consistent with the logic of the muon trigger, which requires segments in at least two muon stations to obtain a meaningful estimate of the muon p_T .
- At least one muon-chamber hit should be included in the global-muon track fit, which can help to suppress hadronic punch-through and muons from decays in flight. Because hadronic punch-through is more likely to produce segments in the inner stations.
- The p_T relative error of the muon best track is less than 30%.
- The transverse and longitudinal impact parameters relative to the primary vertex must be less than 0.2 cm and 0.5 cm, respectively. This requirement suppresses cosmic muons and further suppresses muons from decays in flight.
- The track of the muon candidate must have at least one hit in the pixel detector and at least six hits in silicon-strip layers to guarantee a good p_T measurement and also to suppress muons from decays in flight.
- To suppress backgrounds arising from muons within jets, the scalar- p_T sum of all other tracks in the tracker within a cone of $\Delta R = \sqrt{(\Delta\eta)^2 + (\Delta\phi)^2} = 0.3$ around the muon candidate track, is required to have less than 10% of the p_T of the muon candidate.

The ID + ISO efficiency is defined as:

$$\epsilon_{\text{Muon ID}} = \frac{N(\text{Reconstructed l + ID + ISO})}{N(\text{Reconstructed l})} \quad (2.4)$$

The left plot of figure 2.3 shows the efficiency of muon ID + ISO, as a function of p_T of the generated muon. And the right plot presents a scatter plot showing muon ID + ISO efficiency within the acceptance region as a function of η and ϕ of generated muons.

2. SEARCH FOR LEPTON FLAVOR VIOLATION PROCESSES IN ELECTRON-MUON FINAL STATES WITH CMS 2016 DATA

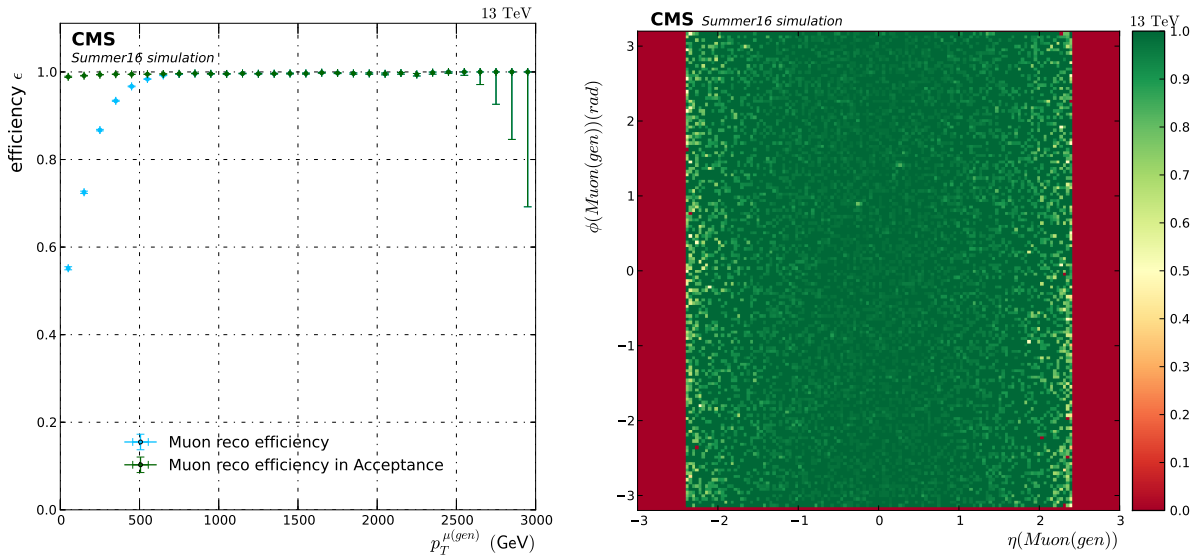


Figure 2.2: Left plot presents muon reconstruction efficiency as a function of p_T of the generated muon in left plot. Right plot presents muon reconstruction efficiency inside acceptance region as a function of muon η and muon ϕ . [134]

2.2.5 Trigger strategy

The High-Level Trigger (HLT) path used to select the events for this analysis is HLT_Mu50 OR HLT_TkMu50 OR HLT_Photon175. The single muon trigger used in this analysis has the lowest p_T threshold among the unpre-scaled single muon trigger paths. The trigger selects the muon candidates over the entire muon detector acceptance. The trigger algorithms are well designed to help the trigger efficiency be less sensitive to the number of pile-up events and be able to cope with the high pile-up conditions of the high-luminosity data taking at 13 TeV. The single muon triggers give some inefficiencies at high mass because of muon track reconstruction. The single photon trigger selects the candidates based on hits in the electromagnetic and hadronic calorimeters. In this analysis, single photon trigger with a threshold of $E_T > 175$ GeV is used to help improve the trigger efficiencies in high mass region. The trigger efficiencies are defined as:

$$\epsilon_{\text{Trig}} = \frac{N(\text{Passed event} + \text{Trigger})}{N(\text{Passed event})} \quad (2.5)$$

and a comparison of the different triggers and their combination is shown in figure 2.4

2.2.6 Event selection

To reduce loss in signal efficiency from misidentification of the sign of the electron's or muon's charge at large p_T , the electron and muon are not required to have opposite charges. Only one $e\mu$ pair is considered per event. When there is more than one $e\mu$ candidate, the pair with the highest invariant mass is selected for analysis. To enhance the sensitivity of the analysis, the analysis is split into four categories depending on the pseudorapidity distribution. The four categories are defined as :

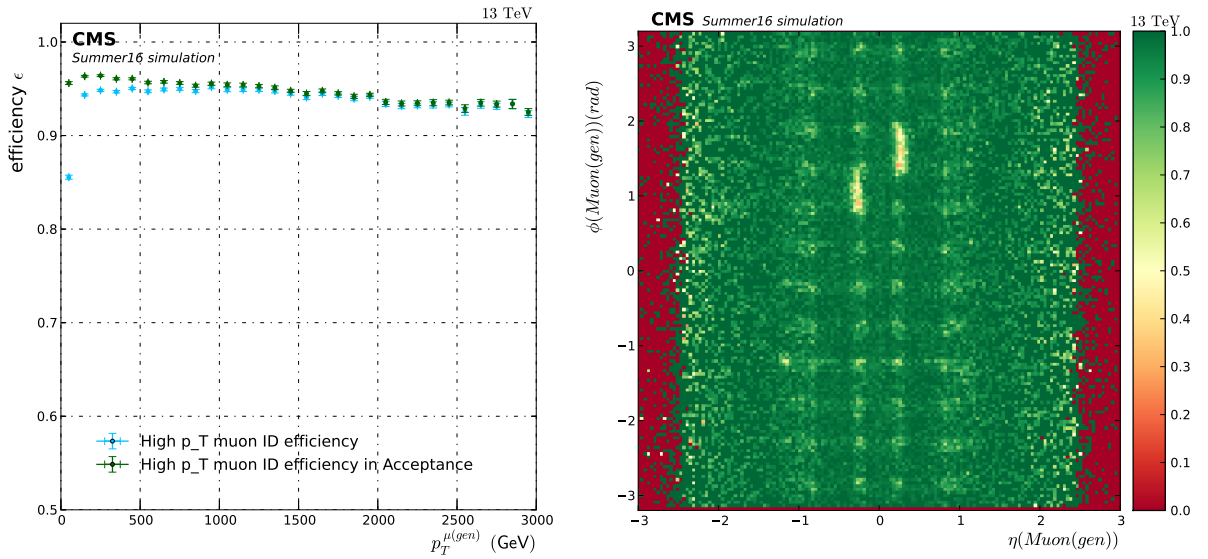


Figure 2.3: Muon identification + isolation efficiency as a function of p_T of the generated muon (left) and as a function of both η and ϕ of generated muons within the acceptance region. [134]

- Barrel-Barrel (BB): $|\eta_e| < 1.4446$ and $|\eta_\mu| < 1.2$
- Barrel-Endcap (BE): $|\eta_e| < 1.4446$ and $1.2 \leq |\eta_\mu| < 2.4$
- Endcap-Barrel (EB): $1.566 < |\eta_e| < 2.5$ and $|\eta_\mu| < 1.2$
- Endcap-Endcap (EE): $1.566 < |\eta_e| < 2.5$ and $1.2 \leq |\eta_\mu| < 2.4$

2.2.7 Event corrections

To account for the differences of the efficiencies in data and MC events, the scale factors and pile-up reweighting are considered on simulation events:

- Electron reconstruction
- Electron identification
- Electron isolation
- Muon identification
- Muon isolation
- Muon trigger

All the scale factors mentioned above have been measured by the muon or egamma group of CMS.

The pile-up reweighting is carried out as recommended by CMS. The systematic uncertainty on the number of pile-up events is taken to be a $\pm 5\%$ shift of the minimum bias cross sections. The comparison between data and simulation for the number of reconstructed primary vertices before and after pile-up reweighting is shown in figure 2.5. As expected, the agreement between data and simulation is better after the reweighting.

2. SEARCH FOR LEPTON FLAVOR VIOLATION PROCESSES IN ELECTRON-MUON FINAL STATES WITH CMS 2016 DATA

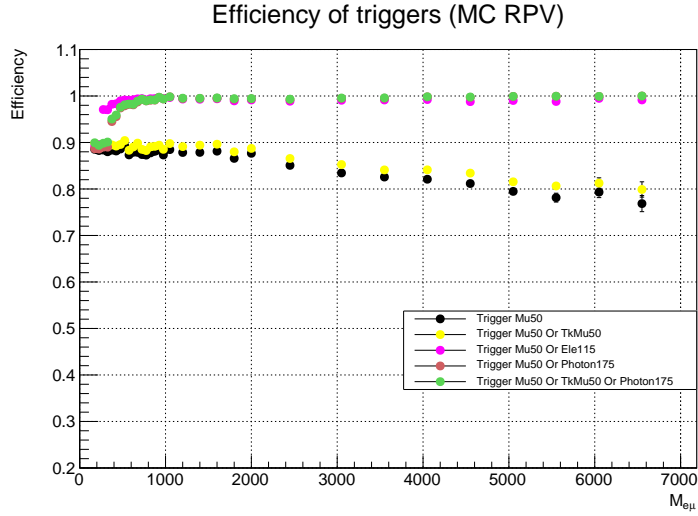


Figure 2.4: Individual trigger efficiencies of passed events as a function of the invariant $e\mu$ mass. Also the combination of different triggers, the dots in green show the combination used in this analysis.

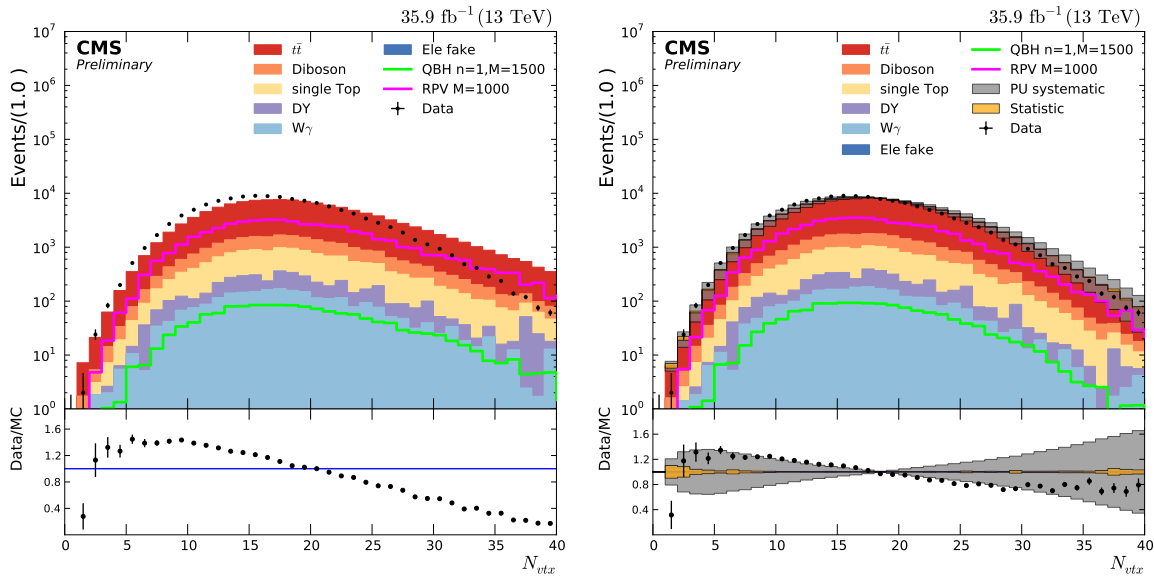


Figure 2.5: Number of reconstructed vertices before (left plot) and after (right plot) pile-up reweighting. After the reweighting the systematic uncertainty due to the $\pm 5\%$ shift of the minimum bias cross section is shown as a gray shaded band. All shown events are required to pass the complete selection described above and contain therefore at least one electron and one muon. [134]

2.3 Background estimation

The backgrounds of this analysis consist of two categories. One is the background from other processes that produce the real electron and/or muon and is called “prompt background”. The other one is called the “jet background” in which a jet is misidentified as an electron (a muon), where the former is much more likely to happen and represents the majority of the spectrum from misidentified leptons.

2.3.1 Prompt background

The prompt background comes from the processes that give two real leptons. We study the prompt background using the Monte Carlo simulation and normalize the contributions to the data luminosity. The contributions are dominated by $t\bar{t}$ events in the lower mass range, while both $t\bar{t}$ and WW events contribute when the mass goes up to 1 TeV. The other background events are from the WZ , ZZ , and single top (and anti-top) production.

This background also includes the DY events decaying to dimuon or dielectron where one of the two lepton is then misidentified as the other lepton flavor, and the $W\gamma$ events where the W decays to a muon and a neutrino and the photon either is misidentified as electron, or converts and gives an electron pair.

2.3.2 Jet background

For the backgrounds which involve a jet misidentified as an electron, a data-driven technique can be used.

The jet background consists of events where a jet is reconstructed as an electron or muon that passes the selection. Since the possibility for a jet to be misidentified as a muon passing the muon selection cuts is much lower than for a jet faking electron case, only the electron fake rate is considered in this analysis.

To estimate the jet background, the “fake rate” method is used in a way similar as in the dielectron resonance search at 13 TeV [138]. We first measure the probability for a jet passing a loose electron selection (pre-selection) to be reconstructed as a good electron, using a multi-jet enriched data control region. Then, we use this result to estimate the contribution of jet background in the signal region. The parametrization of the fake rate is taken from the dielectron resonance search and is given in Table 2.2.

To get an estimation for the jet background, the fake rate is applied to a selected data sample with at least one muon passing the full muon selection and at least one electron passing a fake pre-selection described in Table 2.3 but failing the full electron selection, where both the multi-jet contribution and the dominant contribution from W +jets are accounted for. Further to the selection, a weight with the factor $fakerate/(1 - fakerate)$ is applied on each event which passes the fake electron selection,

2. SEARCH FOR LEPTON FLAVOR VIOLATION PROCESSES IN ELECTRON-MUON FINAL STATES WITH CMS 2016 DATA

Region	E_T range (GeV)	Functional form
Barrel	$35 \leq E_T < 131$	$0.11 - 0.0025 \times E_T + 2.3 \cdot 10^{-5} \times E_T^2 - 7.2 \cdot 10^{-8} \times E_T^3$
	$131 \leq E_T < 356$	$0.014 - 0.00010 \times E_T + 3.6 \cdot 10^{-7} \times E_T^2 - 4.3 \cdot 10^{-10} \times E_T^3$
	$E_T \geq 356$	$0.0028 + 2.4 \cdot 10^{-6} \times E_T$
Endcap $ \eta < 2.0$	$35 \leq E_T < 122$	$0.12 - 0.0013 \times E_T + 4.7 \cdot 10^{-6} \times E_T^2$
	$122 \leq E_T < 226$	$0.035 - 4.8 \cdot 10^{-5} \times E_T$
	$E_T \geq 226$	$0.026 - 9.1 \cdot 10^{-6} \times E_T$
Endcap $ \eta > 2.0$	$35 \leq E_T < 113$	$0.081 - 0.00034 \times E_T$
	$E_T \geq 113$	0.042

Table 2.2: Weight factors of the fake rate for HEEPv7.0 as functions of E_T and η .

Variable	Barrel	Endcap
$\sigma_{i\eta i\eta}$	<0.013	<0.034
H/E	<0.15	<0.10
nr. missing hits	≤ 1	≤ 1
$ dxy $	< 0.02	< 0.05

Table 2.3: The pre-selection criteria in fake rate calculation.

in order to compensate for the lost electrons from the requirement that the electron must fail the full selection.

The selection of one muon passing the selection and one electron passing only the fake rate pre-selection contains still a significant contribution from prompt backgrounds. These contributions are subtracted from MC samples to avoid double counting.

Figure 2.6 shows a cross-check for the jet background from the fake method with a method called the “same sign” method. For the QCD events, there should be equal probabilities to reconstruct the jets with positive or negative charges. Therefore, opposite and same-sign events from the QCD process would give similar distributions. The colored histograms are jet background estimated using fake rate method. The black dots are the jet background estimated using the same-sign method. There can be some fake-background contribution coming from prompt MC, which has been subtracted from data. The agreement between these two kinds of jet distributions is good at high masses, which means that the jet-to-electron rate estimate in data works fine.

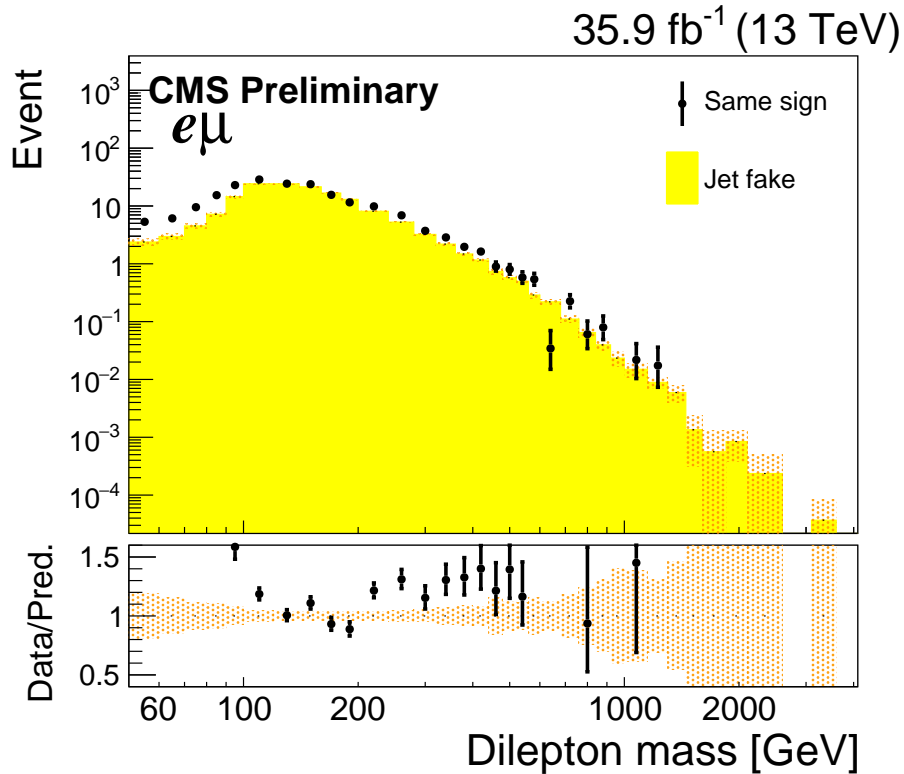


Figure 2.6: Data based closure test for the fake rate method. Data points show the $e\mu$ mass distribution coming from the jet background using data from the same sign region and weight with a factor of 2 to cover both same-sign and opposite-sign regions. The yellow filled histogram shows the jet background derived with the fake rate method which is later used in the analysis. Both methods agree within the assigned uncertainty of 50% on the fake background estimate.

2.4 Systematic uncertainties

In this section, the different systematic uncertainties taken into account for this analysis are presented.

2.4.1 Background systematics

The following systematic uncertainties are taken into account for the background processes

- Muon p_T scale: Systematic uncertainty due to muon p_T scale is taken into account for background event rate. A curvature bias as a function of muon η and ϕ is measured in cosmic data with the endpoint method. The uncertainty is considered like $q/P_T + k$, where q is the charge, p_T is in TeV, and the k is as function of $\eta - \phi$ that is shown in figure 2.7..

- Muon p_T resolution: Systematic uncertainty due to muon p_T resolution is taken into account for background event rate. The uncertainty of the muon p_T resolution has been determined with cosmic ray muons. The muon momentum resolution is smeared by a Gaussian function with a width of 1% in the barrel and 2% in the endcaps to estimate the systematic uncertainty.

- Muon reconstruction plus identification efficiency: A momentum-dependent, downward-only

2. SEARCH FOR LEPTON FLAVOR VIOLATION PROCESSES IN ELECTRON-MUON FINAL STATES WITH CMS 2016 DATA

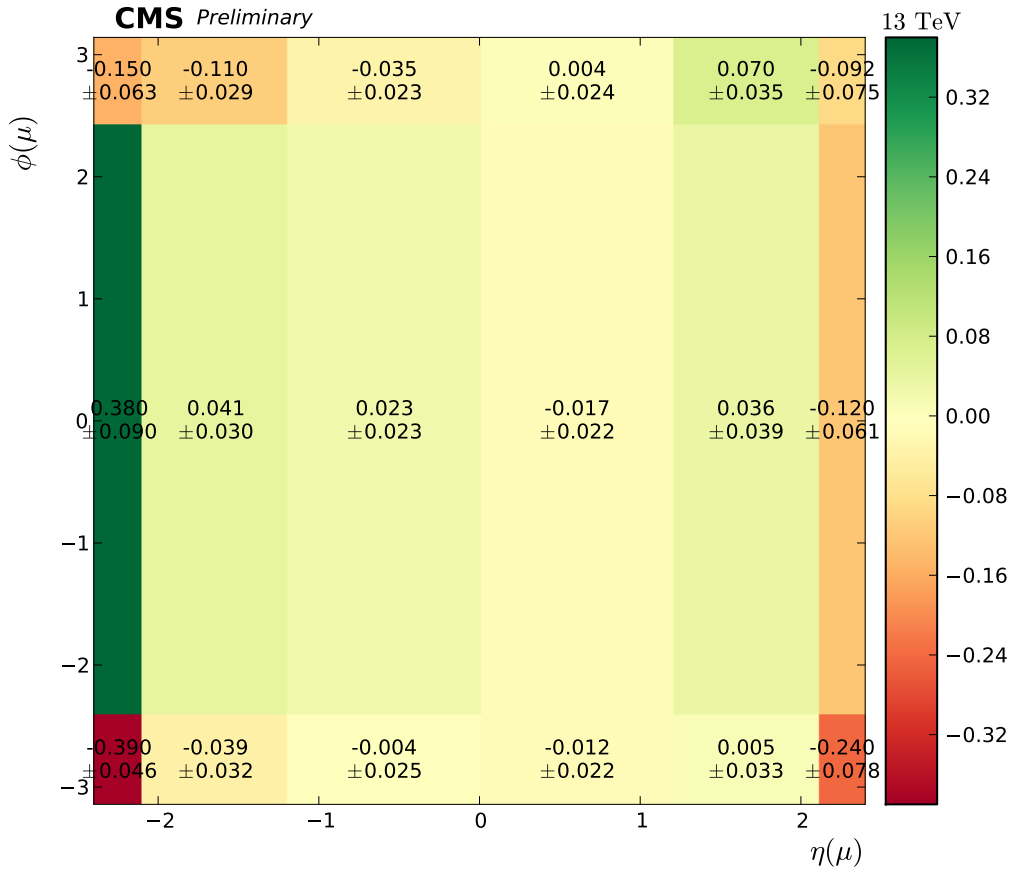


Figure 2.7: Muon p_T scale bias as a function of the muon η and ϕ .

systematic uncertainty is applied on muon reconstruction and identification efficiency to account for the observed trend of smaller number of data events than predicted for high p_T muons. It amounts to -1.6% in the region $|\eta| < 1.6$ and -14.4% in the region $1.6 < |\eta| < 2.4$ for muons with momentum of 4 TeV.

- Muon scale factors: Scale factors are used for muon trigger, isolation, and ID. The trigger, isolation, and ID scale factors are varied by 0.5%, 1%, and 1% to estimate the systematic uncertainty, respectively.

- Electron E_T scale: The electron energy scale is varied by 2% to estimate the systematic uncertainty.

- Electron scale factors: Scale factors are applied for electrons that pass the HEEP ID selection. The scale factors and the corresponding systematic uncertainty are taken from [138]. The uncertainties are varied by 1% for below 90 GeV and 1-3% linearly increase for 90 GeV-1 TeV and 3% for higher energies than 1 TeV in the barrel and 1% for below 90 GeV and 1-4% linearly increase for 90 GeV-300 GeV and 4% for higher than 300 GeV in the endcap.

- Luminosity: A systematic uncertainty of 2.6% is assigned to the integrated luminosity and is used for the background rates.

- Uncertainties on the background cross section are listed as following:

$t\bar{t}$: 5%, WW : 3%, Single (anti-)top : 5%, Drell-Yan : 2%, WZ : 4%, ZZ : 4%.

- $W\gamma$ background and data-driven background: A systematic uncertainty of 50% is assigned for $W\gamma$ background and data-driven background separately.

- Pile-up uncertainty: This uncertainty is estimated by a $\pm 5\%$ shift of the minimum bias cross section of the expected pile-up distribution in data.

- WW shape uncertainty: Uncertainties due to missing differential higher-order corrections for the WW background are taken into account as the WW background is especially at high invariant masses a non-negligible background process. The uncertainty is derived by the differential NLO electroweak corrections to the LO cross section and is calculated as a function of the invariant $e\mu$ mass.

- Top shape uncertainty: Uncertainties associated with the modeling of the shape in the $e\mu$ invariant mass distribution are taken into account for the $t\bar{t}$ background, which leads to the dominant uncertainty in the total background yield of up to 26% at $M_{e\mu} = 1$ TeV. This uncertainty is estimated from the differential distribution of re-summed cross-sections at NLO+NNLO for $M_{t\bar{t}}$ as presented in [139] and the variation of the QCD scale in the simulation. The contribution of both mass dependent uncertainty and QCD scales are shown in figure 2.8.

Figure 2.9 shows relative shape-based uncertainties arising from different sources.

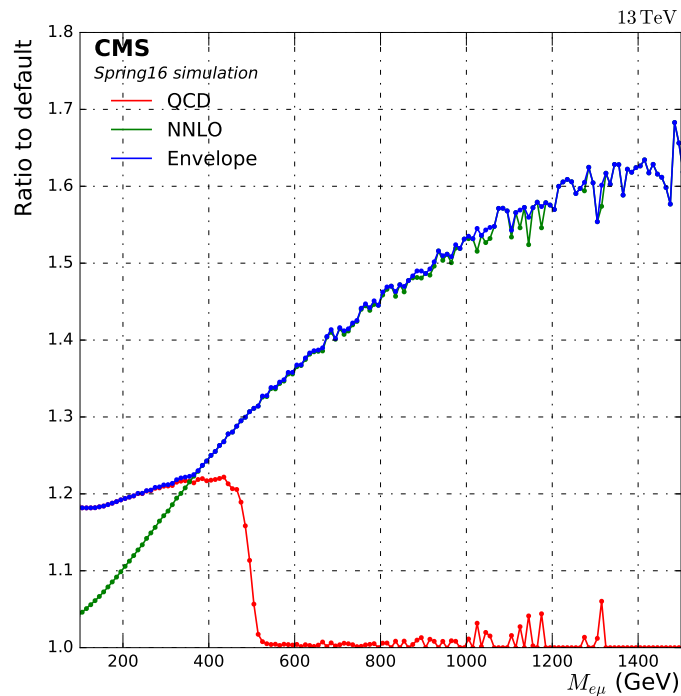


Figure 2.8: Relative uncertainty on the event yield of the $t\bar{t}$ background as a function of $M_{e\mu}$. Both considered sources of uncertainty and the envelope which is used in the analysis are shown. The drop of the QCD scale variation uncertainty at $M_{e\mu} \sim 500$ GeV is due to the high mass $t\bar{t}$ tail samples not containing the corresponding uncertainty information. As we take the envelope of both uncertainties and in this region the higher order uncertainties are clearly dominant this is no problem for the analysis. [134]

2. SEARCH FOR LEPTON FLAVOR VIOLATION PROCESSES IN ELECTRON-MUON FINAL STATES WITH CMS 2016 DATA

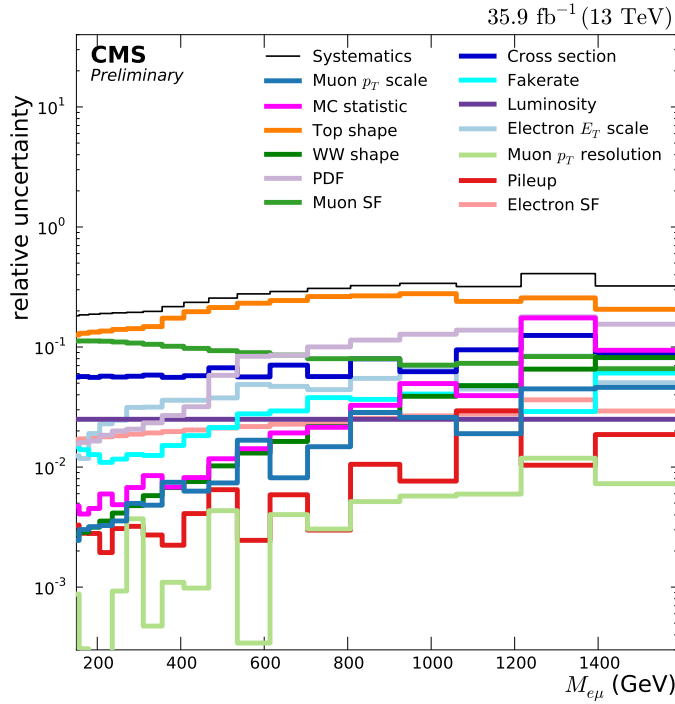


Figure 2.9: Relative shape-based uncertainty on the background yield. Shown are the different contributions to the systematic uncertainty on the background yield. Also shown is the quadratic sum of all systematic uncertainties, labeled 'Systematics'. The statistical uncertainty on the background yield due to the Poisson distribution of the number of events is shown via the 68% confidence Interval of the Poisson distribution corresponding to the expected number of background events. [134]

2.4.2 RPV, QBH, and Z' signal systematics

The following systematic uncertainties are taken into account for the RPV signal:

- Luminosity: A systematic uncertainty of 2.5% is assigned to the integrated luminosity.
- PDF uncertainties are considered for slightly different for the signal than for the background.

For the signal, only the effect on the acceptance is taken into account while the mean variation due to the PDFs is not taken into account. The left plot of figure 2.10 shows the relative influence for PDF uncertainties on the signal yield following the PDF4LHC recommendations. The effect which we account for on the acceptance is shown in figure 2.11 as PDF up and PDF down lines.

- Acceptance \times efficiency: Systematic uncertainty for the acceptance \times efficiency is considered according to the figure 2.12. They are derived by propagating the systematic uncertainties mentioned in the previous subsection onto the acceptance \times efficiency and then parametrizing the shifted distributions. The relative effect on acceptance \times efficiency for all different sources of uncertainty is shown in figure 2.11.

- Mass resolution: Systematic uncertainty on the mass resolution is considered for signal events. The uncertainty is mass-dependent as shown in figure 2.13. This uncertainty does not affect the normalization although it results in small change in the shape of the $e\mu$ invariant mass distribution. They are derived by propagating the systematic mentioned in the previous subsection onto the mass

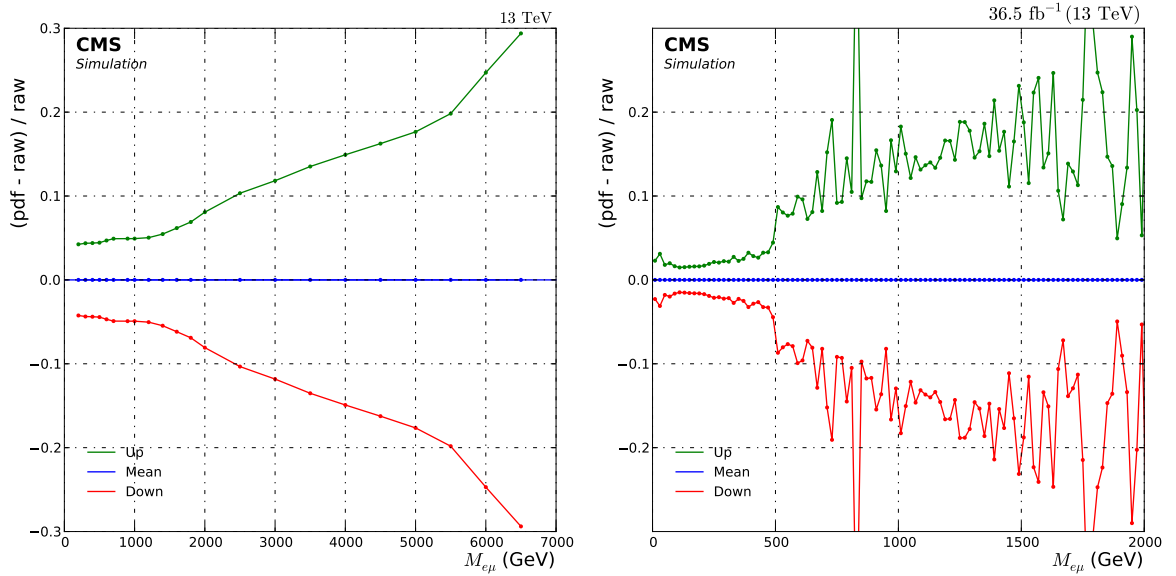


Figure 2.10: Relative uncertainty on the event yield due to PDF uncertainties for signal (left) as a function of the generated τ -sneutrino $\tilde{\nu}_\tau$ mass and for background (right) as a function of the $M_{e\mu}$. Shown is the relative difference between the reweighted sample (called ‘pdf’) and the unweighted sample from the generator (called ‘raw’). Three different reweighted distributions are shown: the mean value, and the up and down variation. [134]

resolution and then parametrizing the shifted distributions.

The same uncertainties as mentioned in the previous subsection are also considered for the Z' and QBH signal. The effect of the pdf variation on both signals is shown in figure 2.14 following the PDF4LHC recommendations.

2. SEARCH FOR LEPTON FLAVOR VIOLATION PROCESSES IN ELECTRON-MUON FINAL STATES WITH CMS 2016 DATA

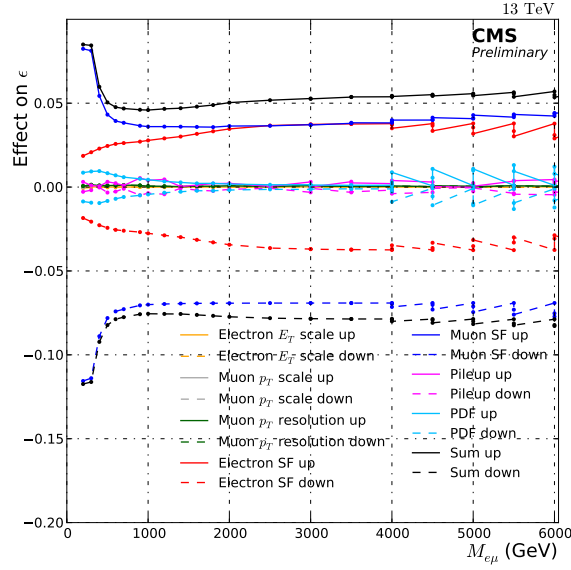


Figure 2.11: Relative effect of the different source of uncertainty on the acceptance times efficiency. They are also included in figure 2.9 as up and down variations and parametrized for the statistical interpretation. The leading uncertainties over the whole mass range are due to the uncertainty on the muon and electron efficiencies. [134]

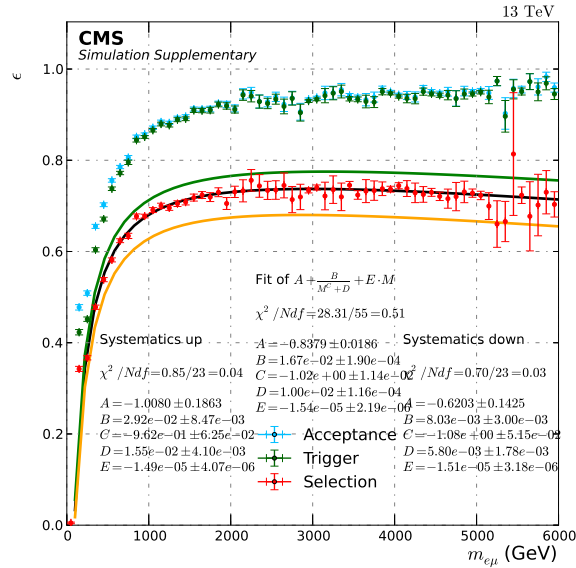


Figure 2.12: Efficiency of the RPV signal for all events [a] after the acceptance requirements (light blue points), [b] after acceptance and trigger requirements (dark green points) and [c] after the full selection including acceptance and trigger criteria (red points). In each case, the reconstruction efficiency is also included. This final acceptance times efficiency is then parametrized for the statistical interpretation by the black line. The systematic uncertainties are derived by propagating the effect of the systematic uncertainties described above towards the efficiency. The relative effect of the different systematic uncertainties is shown in Figure 2.11. The parametrization of systematically shifted upper and lower efficiency are shown in green and orange. [134]

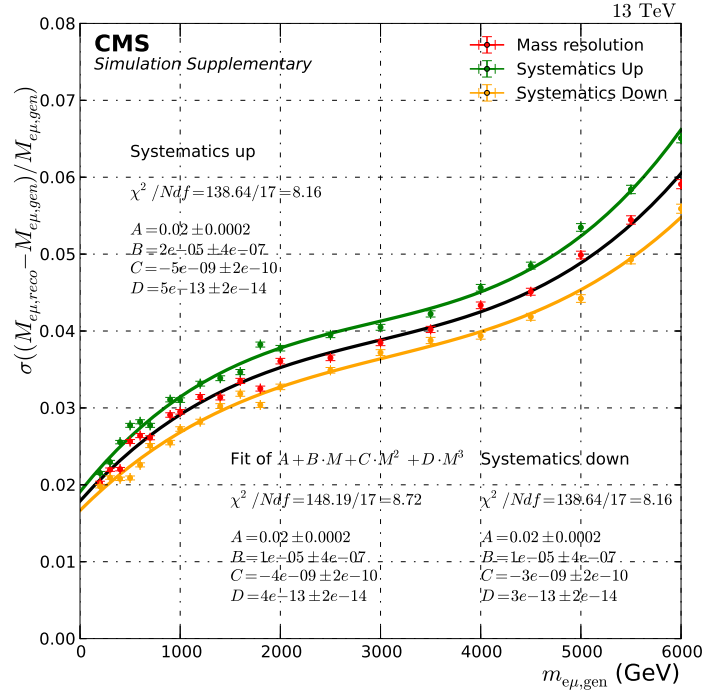


Figure 2.13: Relative invariant mass resolution for all events of $e\mu$ pairs obtained from RPV signal simulation.

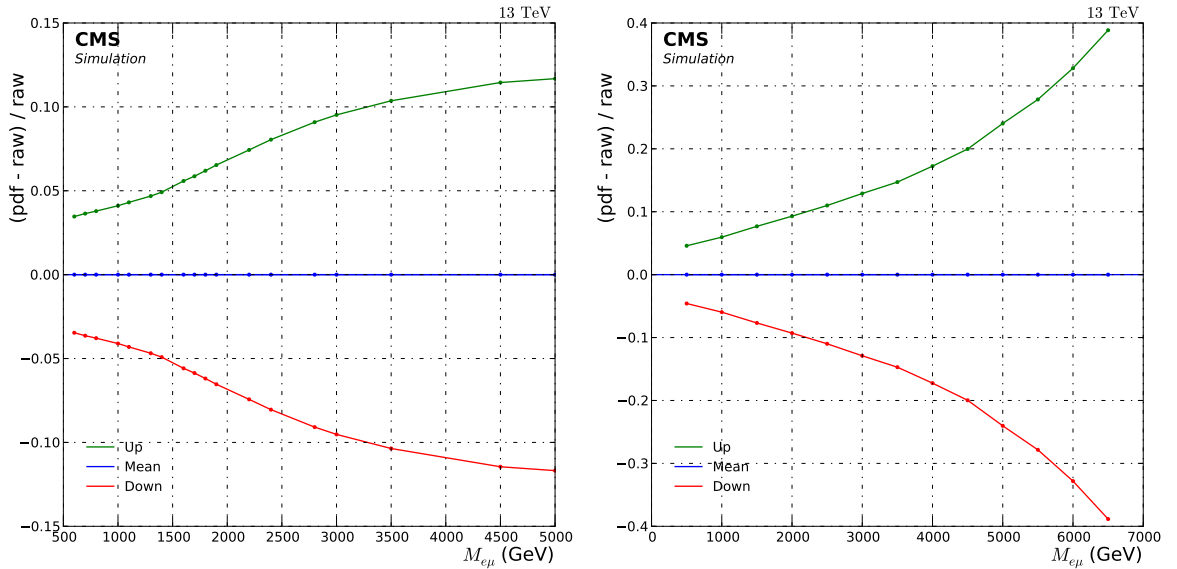


Figure 2.14: Relative uncertainty on the event yield due to PDF uncertainties for Z' signal (left) as a function of the generated Z' mass and for the QBH signal (right) as a function of the threshold mass. Shown is the relative difference between the re-weighted sample (called 'pdf') and the unweighted sample from the generator (called 'raw'). Three different re-weighted distributions are shown: the mean value, and the up and down variation. [134]

2.5 Invariant mass distributions

The kinematic distributions of muon for different analysis categories (barrel-barrel, barrel-endcap, endcap-barrel, and endcap-endcap) are shown in Appendix A.

The invariant mass distributions are shown in figure 2.15, and 2.16 for all selected events. A multidimensional maximum likelihood fit to observed data is performed on the background events in order to constrain the background normalization and the systematic uncertainties. The systematic uncertainties are reduced by a factor of four after the fit.

The numbers of data and MC events are given for different bins of invariant mass in Table 2.4.

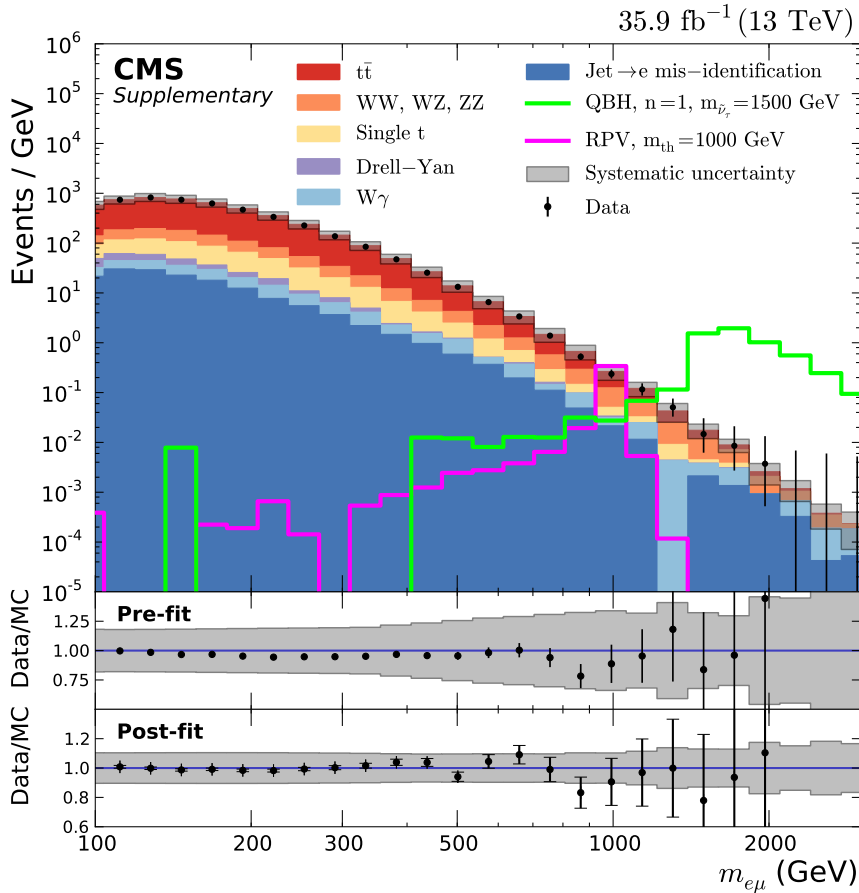


Figure 2.15: Simplified plot of the invariant mass of the $e\mu$ pair. The only difference between this plot and the one shown before is that this one has coarser binning than the other and thus more suitable for presentation purposes by requiring a minimum bin width of 50 GeV. The offset between data and Standard Model expectation is consistent with other measurements and covered by the uncertainties. [134]

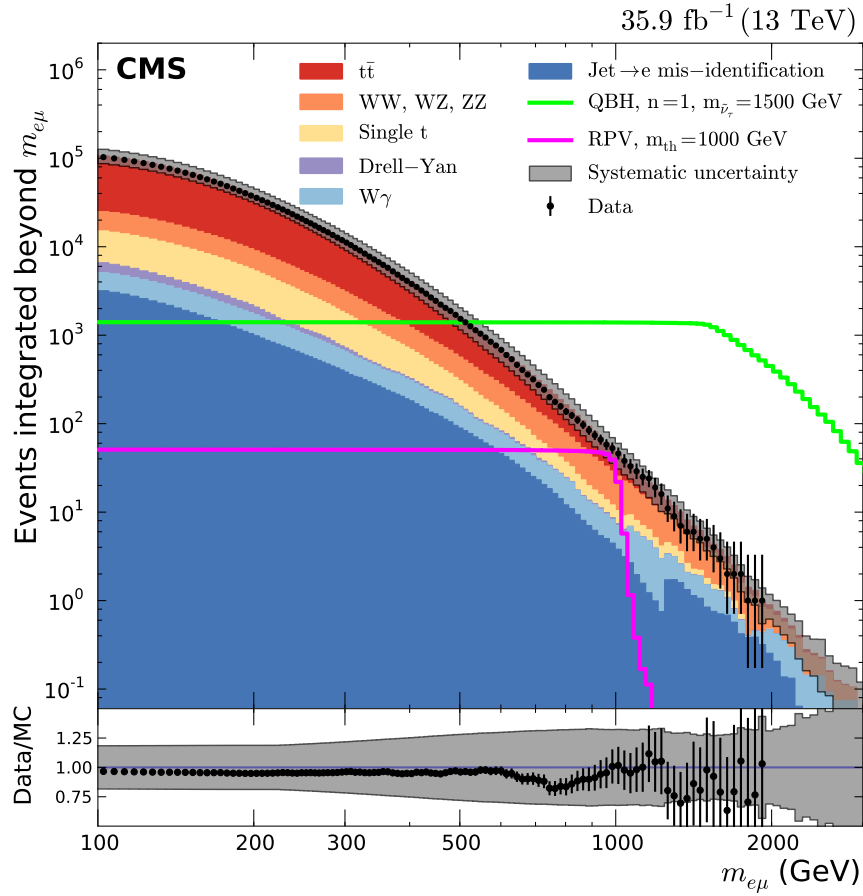


Figure 2.16: Invariant mass (cumulative) distribution of the $e\mu$ pair. [134]

Table 2.4: Numbers of expected and observed events for different bins of $e\mu$ invariant mass. Also the statistical and systematic uncertainties on the number of background events are given.

Mass range (GeV)	Observed events	Expected events \pm (stat.) \pm (sys.)
$M_{e\mu} < 500$	124756	$128062 \pm 198 \pm 18141$
$500 < M_{e\mu} < 1000$	1411	$1506 \pm 13 \pm 399$
$1000 < M_{e\mu} < 1500$	39	$39.9 \pm 2.2 \pm 12.6$
$1500 < M_{e\mu}$	4	$4.7 \pm 0.42 \pm 1.01$

2.6 Invariant mass resolution

The relative per-event mass resolution is defined as $(M_{e\mu,\text{reco}} - M_{e\mu,\text{gen}})/M_{e\mu,\text{gen}}$ and this quantity is evaluated for each signal event that passes the event selection. The resulting distributions are fitted with a Crystal Ball function. One such Crystal Ball fit for RPV signal mass point 700 GeV (1900 GeV and 3500 GeV) is shown in figure 2.17(2.18, 2.19) with the corresponding residual and pull distributions. The Crystal Ball function is defined as:

$$f(x; \alpha, n, \bar{x}, \sigma) = N \cdot \begin{cases} \exp\left(-\frac{(x-\bar{x})^2}{2\sigma^2}\right), & \text{for } \frac{x-\bar{x}}{\sigma} > -\alpha \\ A \cdot (B - \frac{x-\bar{x}}{\sigma})^{-n}, & \text{for } \frac{x-\bar{x}}{\sigma} \leq -\alpha \end{cases} \quad (2.6)$$

with input:

$$\begin{aligned} A &= \left(\frac{n}{|\alpha|}\right)^n \cdot \exp\left(-\frac{|\alpha|^2}{2}\right) \\ B &= \frac{n}{|\alpha|} - |\alpha| \\ N &= \frac{1}{\sigma(C+D)} \\ C &= \frac{n}{|\alpha|} \cdot \frac{1}{n-1} \cdot \exp\left(-\frac{|\alpha|^2}{2}\right) \\ D &= \sqrt{\frac{\pi}{2}} \left(1 + \operatorname{erf}\left(\frac{|\alpha|}{\sqrt{2}}\right)\right) \end{aligned}$$

The σ of the Crystal Ball is chosen as a measure of the mass resolution. The relative invariant mass resolution of the all $e\mu$ pairs obtained from the RPV samples is shown in figure 2.20. A fit is performed to the mass resolution distribution. The fit function is the following:

$$f_{\text{res}} = A + B \cdot M_{e\mu,\text{gen}} + C \cdot M_{e\mu,\text{gen}}^2 + D \cdot M_{e\mu,\text{gen}}^3 \quad (2.7)$$

where $M_{e\mu,\text{gen}}$ is the gen-level invariant mass of the $e\mu$ pair. The values of the coefficients A, B, C, and D are given in the plots shown in figures 2.20. This function is used to model the Gaussian shape of the signal distribution in the limit setting procedure.

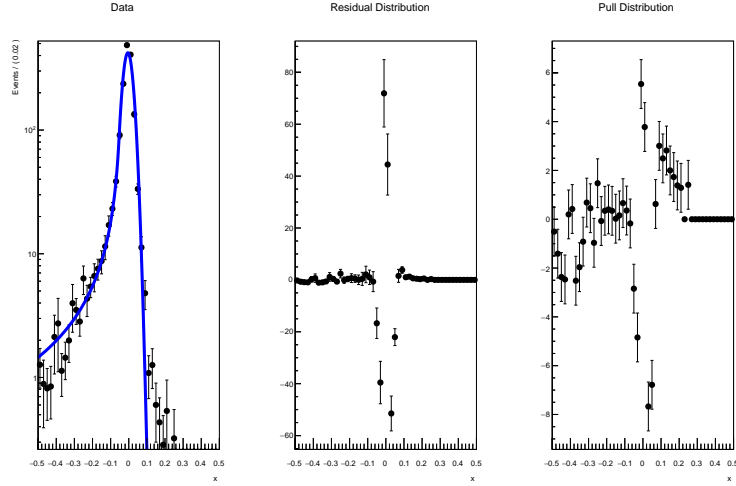


Figure 2.17: Crystal Ball fit of mass resolution for the RPV signal mass point 700 GeV with the corresponding residual and pull distributions. [134]

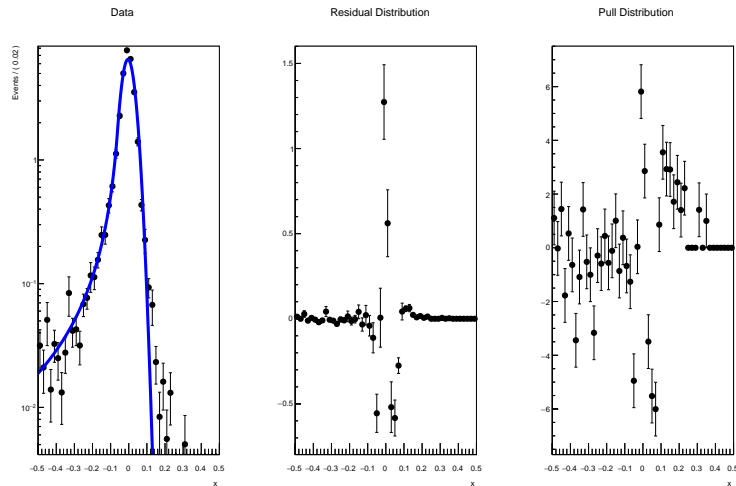


Figure 2.18: Crystal Ball fit of mass resolution for the RPV signal mass point 1900 GeV with the corresponding residual and pull distributions. [134]

2. SEARCH FOR LEPTON FLAVOR VIOLATION PROCESSES IN ELECTRON-MUON FINAL STATES WITH CMS 2016 DATA

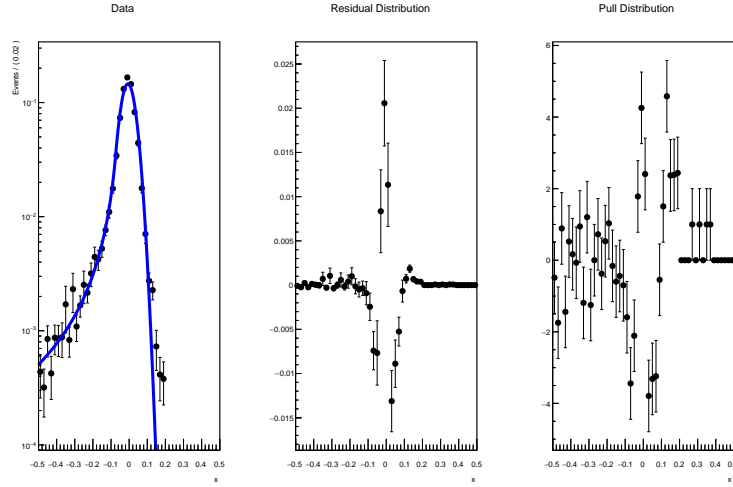


Figure 2.19: Crystal Ball fit of mass resolution for the RPV signal mass point 3500 GeV with the corresponding residual and pull distributions. [134]

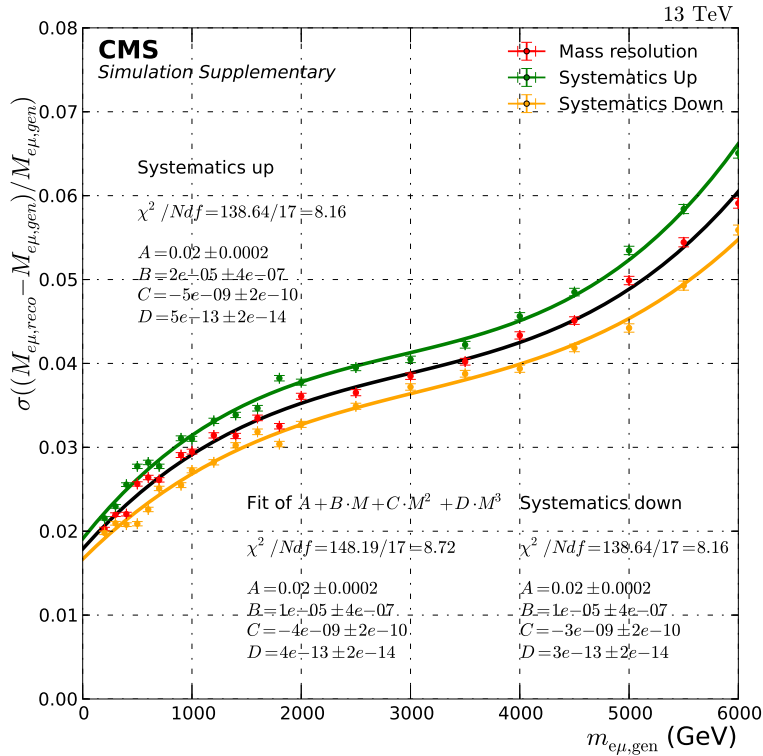


Figure 2.20: Relative invariant mass resolution for all events of $e\mu$ pairs obtained from RPV signal simulation. The systematic uncertainties are derived by propagating the effect of the systematic uncertainties towards the mass resolution. [134]

2.7 Statistical interpretation

The limit setting is done with a Bayesian approach. In the Bayesian approach, the probability of a theory to be true given current data condition is defined:

$$P(\text{theory}|\text{data}) \propto P(\text{data}|\text{theory}) \cdot P(\text{theory}) \quad (2.8)$$

where the $P(\text{data}|\text{theory})$ is the likelihood (L) of data to the theory, $P(\text{theory})$ is the prior probability of the theory. We would like to calculate the limits on the cross section of the theory. From the Eq. 2.8, we get the posterior probability for the limit setting:

$$P(\mathbf{r}|\mathbf{N}) = \frac{L(\mathbf{N}|\mathbf{r}) \cdot \pi(\mathbf{r})}{\int L(\mathbf{N}|\mathbf{r}') \cdot \pi(\mathbf{r}') d\mathbf{r}'} \quad (2.9)$$

Where the $L(\mathbf{N}|\mathbf{r})$ is likelihood for observing \mathbf{N} , given the expectation of background events (b) and signal events (s) from theory, and the signal strength modifier (\mathbf{r}):

$$\mathbf{r} = \frac{\sigma_{\mathbf{r}}}{\sigma_{\text{theory}}} \quad (2.10)$$

The likelihood is given by the Poisson distribution:

$$L(\mathbf{N}|\mathbf{r}) = \frac{(\mathbf{r} \cdot \mathbf{s} + b)^{\mathbf{N}}}{\mathbf{N}!} e^{-(\mathbf{r} \cdot \mathbf{s} + b)} \quad (2.11)$$

The $\pi(\mathbf{r})$ is flat prior with the constraint that the cross section of theory should be positive.

$$\pi(\mathbf{r}) = \begin{cases} 0, \mathbf{r} < 0 \\ 1, \mathbf{r} \geq 0 \end{cases} \quad (2.12)$$

To take the systematic uncertainties into account, additional nuisance parameters (ν) are needed. There are three kinds of systematic uncertainties considered in different ways.

- **Scaling uncertainties.** This includes the uncertainties with only a constant value, such as the luminosity. We introduce factor g and its uncertainty σ_g . For all scaling uncertainties a log-normal distribution is used as the prior. We consider all the uncertainties as independent and therefore the priors can be multiplied with each other. The probability distribution is approximated by a Gaussian and defined as:

$$P_{g,\sigma_g}(x) = \frac{1}{x\sqrt{2\pi}\sigma_g} e^{-\frac{(\ln \frac{x-g}{\sigma_g})^2}{2\sigma_g^2}} \quad (2.13)$$

- **Shape uncertainties.** This includes the uncertainties which have different distribution and can not be considered easily as a constant value. For each of the uncertainties, the central value of background or signal events and the shifted up and down events in each bin x_0, x_{\pm} are know. These values can be transferred into a continuous probability density function by a morphing parameter f ,

2. SEARCH FOR LEPTON FLAVOR VIOLATION PROCESSES IN ELECTRON-MUON FINAL STATES WITH CMS 2016 DATA

where f is a Gaussian with a mean of zero and a width of one. The number of expected events is replaced by a function $x(f)$ defined as:

$$x(f) = \begin{cases} \frac{f(f-1)}{2}x_- - (f-1)(f+1)x_0 + \frac{f(f+1)}{2}x_+ & , |f| < 1 \\ \frac{x_+ + x_-}{2} + f \frac{x_+ - x_-}{2} & , \text{else} \end{cases}$$

For $|f| < 1$ the number of events $x(f)$ is extrapolated quadratically, for values off outside the range it is extrapolated linearly.

- MC statistic uncertainties. We set the MC uncertainties for each bin using Gaussian or Poisson distribution according to the effective number of unweighted background events. The total background n_{tot} and error e_{tot} are used. For a Gaussian-constrained uncertainty the yield scales as $n_{\text{tot}} + x \cdot e_{\text{tot}}$, where x is distributed following a Gaussian with mean zero and width one. For the Poisson-constrained uncertainty, the scaling parameter x is used as a yield multiplier with nominal value one: $n_{\text{tot}} \cdot x$.

The dependence on the nuisance parameters eliminated by integrating over them:

$$P(r|N) = \int P(r, \nu|N) d\nu \quad (2.14)$$

This integration is time consuming because of the high number of dimensions $\nu = (\nu_1, \nu_2, \dots, \nu_n)$, therefore a random walk method, the Markov-Chain Monte Carlo (MCMC), is used.

Then the 95% confidence level upper limit r_{95} is obtained by integrating the probability:

$$0.95 = \int_{-\infty}^{r_{95}} P(r|N) dr \quad (2.15)$$

We use a multi-bin limit to take into account the information of the shape of the signal and background distributions. The inputs for the limit calculation in this case are the invariant mass histograms of signal, background, and data. Multiple bins can be considered into the limit calculation by multiplying the different probabilities in Eq. 2.15, resulting in :

$$0.95 = \int_{-\infty}^{r_{95}} \prod_{i \in \text{bins}} P_i(r|N) \quad (2.16)$$

We finally get the observed limit for each possible signal hypothesis, and we can also calculate the expected limit, which is the cross section that could be excluded if no signal were present in the data.

2.7.1 Signal model

The RPV signals result in a narrow resonance. A crystal ball function is used to model the RPV τ -neutrino signal shape. The resolution σ is taken from the fit to the invariant mass resolution as described in the previous section. Histograms are constructed from the Crystal ball signal PDF and they are normalized to the expected number of signal events, given by the signal cross section, the

integrated luminosity, and the efficiencies. The RPV signal cross section is calculated at NLO in perturbative QCD. The parametrization of the narrow resonance allows for a scan of the invariant mass spectrum with a fine spacing of the signal mass hypothesis that corresponds to the invariant mass resolution.

The QBH signal exhibits a broader shape with a sharp edge at the threshold mass M_{th} , which is smeared out by the detector resolution, and a tail towards higher masses that is shaped by the parton distribution functions of the proton. The QBH signal shapes are obtained directly from simulated samples.

The studied sequential Standard Model Z' has a width larger than the RPV model, resulting in a slightly different shape. The most important part is an increased off-shell production at low masses. The width of the signal as a function of the Z' mass is shown in figure 2.21 as calculated by Pythia8. On the other hand, the extra-dimension Z' model has a narrow width comparable to the RPV signal model. The width of the sequential Standard Model Z' , extra-dimension Z' model and RPV model are compared for various mass points in figure 2.22.

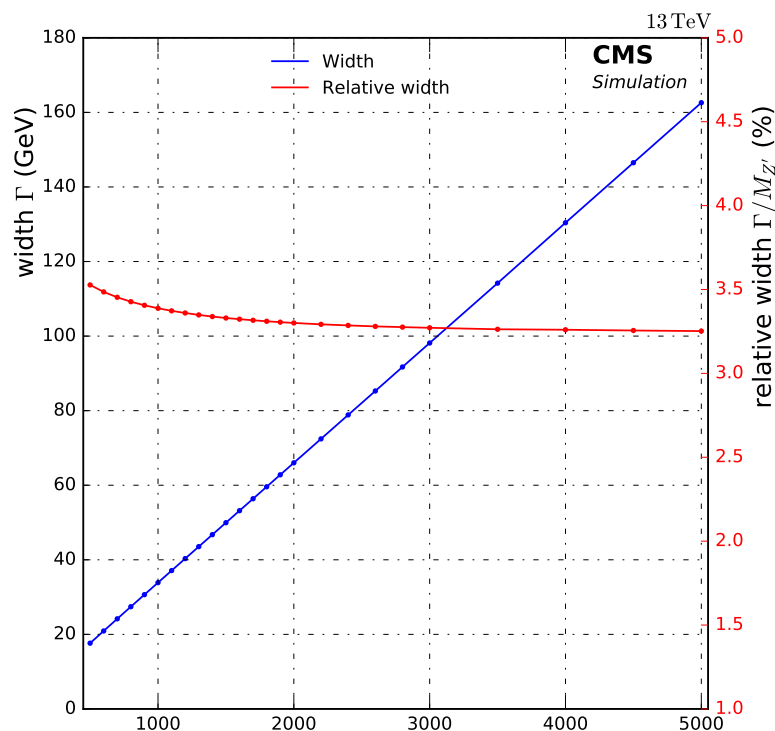


Figure 2.21: Width of the Z' signal as a function of the Z' mass as calculated by pythia8. The total width Γ is shown in GeV and the relative width $\Gamma/M_{Z'}$ is shown in %. [134]

In figure 2.23, the mass distributions under different models of sequential Standard Model Z' , extra-dimension Z' model and RPV model are compared at reconstructed level at the same mass points presented in figure 2.22. It can be seen that the detector resolution almost wash out the effect of a wider width of the sequential Standard Model. A signal shape can work for these three signal

2. SEARCH FOR LEPTON FLAVOR VIOLATION PROCESSES IN ELECTRON-MUON FINAL STATES WITH CMS 2016 DATA

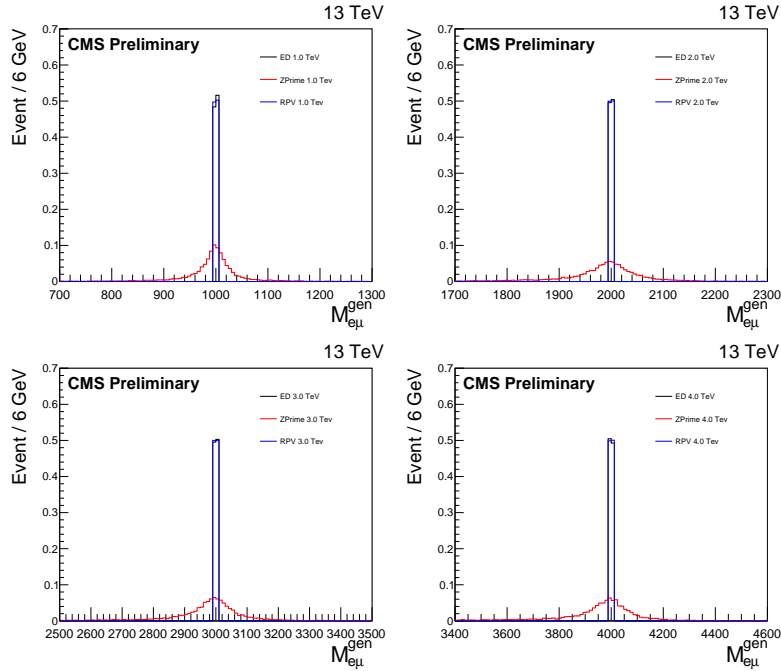


Figure 2.22: The mass distributions of sequential Standard Model Z' , extra-dimension Z' model and RPV model signal in generation level.

models. As it is checked that the acceptance is almost the same for the sequential Standard Model Z' and extra-dimension Z' model, the same upper limit can be used to exclude these two models simultaneously.

2.7.2 Background model

The background model used in the limit setting for the $e\mu$ channel is taken from the MC simulations for the $t\bar{t}$, diboson, single-top, $W\gamma$, and Drell-Yan backgrounds, and is estimated from data for the jet faking electron background.

2.7.3 Limit setting procedure

Since no excess with respect to the expectation is found in the measured invariant mass distribution shown in figure 2.15, the exclusion limits at 95% C.L. on the signal cross section are determined with the multi-bin limit setting tool. The *MarkovChainMC* Bayesian method with a flat prior for the signal cross section is used. For the resonant RPV signal with any mass hypothesis M , the whole invariant mass spectrum that from 0 TeV to 10 TeV is used as a search region. The multi-bin limit is derived in these search regions using binned histograms as input. The nuisance parameters for the uncertainties on the luminosity and background cross sections are modeled with Log-normal distributions in the likelihood function. The uncertainties on the muon p_T scale and resolution, the electron E_T scale, electron ID, muon ID, PDF, and pile-up are accounted for using the template morphing technique.

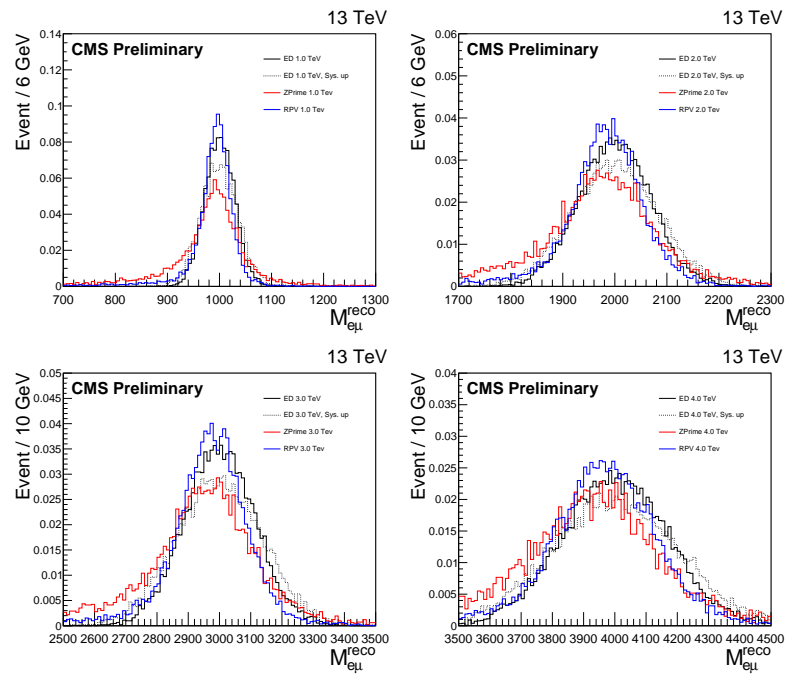


Figure 2.23: The mass distributions of sequential Standard Model Z' , extra-dimension Z' model and RPV model signal in reconstruction level.

2.8 Limit results

The results for different models obtained in this analysis are shown in Table 2.5 as a summary and in the following sub-sections in detail.

Models	Obs. limit	Exp. limit	
RPV	1.7 TeV	1.9 TeV	$\lambda_{132} = \lambda'_{311} = 0.01$
	3.8 TeV	3.8 TeV	$\lambda_{132} = \lambda'_{311} = 0.1$
Z'	4.4 TeV	4.4 TeV	
QBH	3.6 TeV	3.6 TeV	n = 1
	5.3 TeV	5.3 TeV	n = 4
	5.5 TeV	5.5 TeV	n = 5
	5.6 TeV	5.6 TeV	n = 6

Table 2.5: The results of observed and expected lower mass limits for RPV, Z' and QBH models.

2.8.1 RPV τ sneutrino

The expected and observed limit for the RPV τ sneutrino is shown in figure 2.24.

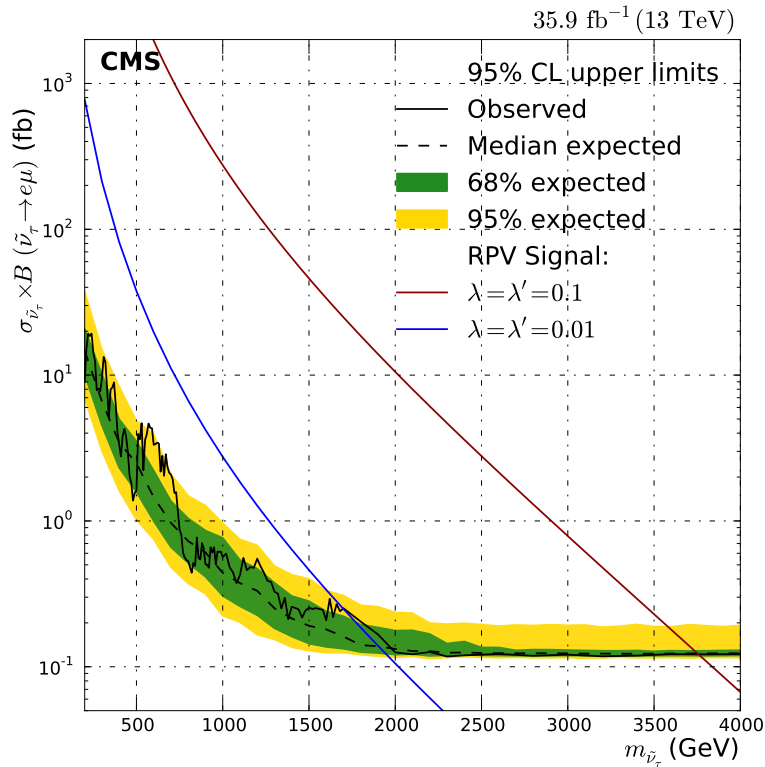


Figure 2.24: 95% C.L. expected limit and observed limit for the RPV signal in $e\mu$ channel. [134]

For RPV couplings $\lambda_{132} = 0.01$ and $\lambda'_{311} = 0.01$, an expected mass limit of 1.9 TeV is obtained, while the observed mass limit is 1.7 TeV. For RPV couplings $\lambda_{132} = 0.1$ and $\lambda'_{311} = 0.1$, the expected

mass limit is 3.8 TeV and the observed mass limit is 3.8 TeV.

The cross section limit in figure 2.24 is valid for any signal with the same signal shape and selection efficiency as the RPV signal with $\lambda_{132} = 0.1$ and $\lambda'_{311} = 0.1$ assumed in the plot. For all RPV coupling values not yet excluded by direct searches, the intrinsic width $\Gamma_{\tilde{\nu}_\tau}$ can be neglected compared to the detector resolution and the two conditions mentioned are always fulfilled. The observed excluded cross section $\sigma \cdot \text{BR}_{\text{obs}}^{\text{excl}}(M_{\tilde{\nu}_\tau})$ shown in figure 2.24 can therefore be used to derive the limit contour in the $M_{\tilde{\nu}_\tau} - \lambda'_{311}$ parameter plane as a function of a given fixed value λ_{132}^{fix} . In the narrow-width approximation, the cross section scales with the RPV couplings as:

$$\sigma \cdot \text{BR}(\tilde{\nu}_\tau \rightarrow e^\pm \mu^\mp) = k(M_{\tilde{\nu}_\tau}) \cdot \frac{(\lambda'_{311})^2 \left((\lambda_{132}^{fix})^2 + (\lambda_{231}^{fix})^2 \right)}{3 (\lambda'_{311})^2 + \left((\lambda_{132}^{fix})^2 + (\lambda_{231}^{fix})^2 \right)}. \quad (2.17)$$

For $\lambda'_{311} \ll \lambda_{132}$, the signal cross section becomes independent of λ_{132} and for $\lambda'_{311} \gg \lambda_{132}$ it reaches the maximal value $\sigma_{max}(M_{\tilde{\nu}_\tau}, (\lambda_{132}^{fix})^2 + (\lambda_{231}^{fix})^2) = k(M_{\tilde{\nu}_\tau}) \cdot \frac{2}{3}((\lambda_{132}^{fix})^2 + (\lambda_{231}^{fix})^2)$. If this maximal cross section is not excluded for a given parameter pair $(M_{\tilde{\nu}_\tau}, \lambda_{132})$, then no limit can be set on the coupling λ'_{311} . Otherwise, the limit on the coupling λ'_{311} is given by

$$\lambda'_{311}{}^{limit} \left(M_{\tilde{\nu}_\tau}, (\lambda_{132}^{fix})^2 + (\lambda_{231}^{fix})^2 \right) = \sqrt{\frac{\left((\lambda_{132}^{fix})^2 + (\lambda_{231}^{fix})^2 \right)}{\frac{k(M_{\tilde{\nu}_\tau})}{\sigma \cdot \text{BR}_{\text{obs}}^{\text{excl}}(M_{\tilde{\nu}_\tau})} \cdot \left((\lambda_{132}^{fix})^2 + (\lambda_{231}^{fix})^2 \right) - 3}}. \quad (2.18)$$

Limit contours for the RPV signal are shown in figure 2.25.

2.8.2 Sequential Standard Model Z'

The expected limit for the sequential Standard Model Z' is shown in figure 2.26 for all selected events. An expected and observed mass limit of 4.4 TeV is obtained.

2.8.3 QBH

In the QBH search we set mass limits on the production threshold for QBH production, M_{th} , in models with $n = 1$ (RS) and $n = 4, 5, 6$ (ADD) extra dimensions. The 95% C.L. limits on the signal cross section times branching ratio for the QBH signal are shown in figure 2.27. For $n = 1$ and 4, 5, 6, the resulting expected (observed) limits on M_{th} are 3.6 TeV (3.6 TeV), 5.3 TeV (5.3 TeV), 5.5 TeV (5.5 TeV), and 5.6 TeV (5.6 TeV) respectively.

2. SEARCH FOR LEPTON FLAVOR VIOLATION PROCESSES IN ELECTRON-MUON FINAL STATES WITH CMS 2016 DATA

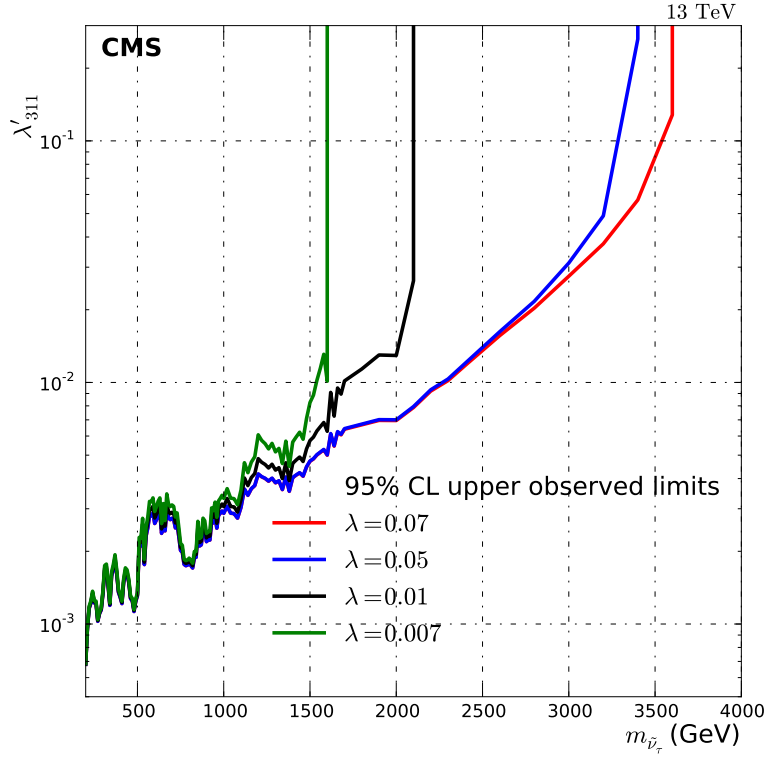


Figure 2.25: 95% CL observed limit contour for the RPV signal in the $M_{\tilde{\nu}_\tau} - \lambda'_{311}$ parameter space. The values of the other coupling λ_{132} are fixed to 0.07, 0.05, 0.01, 0.007, respectively. [134]

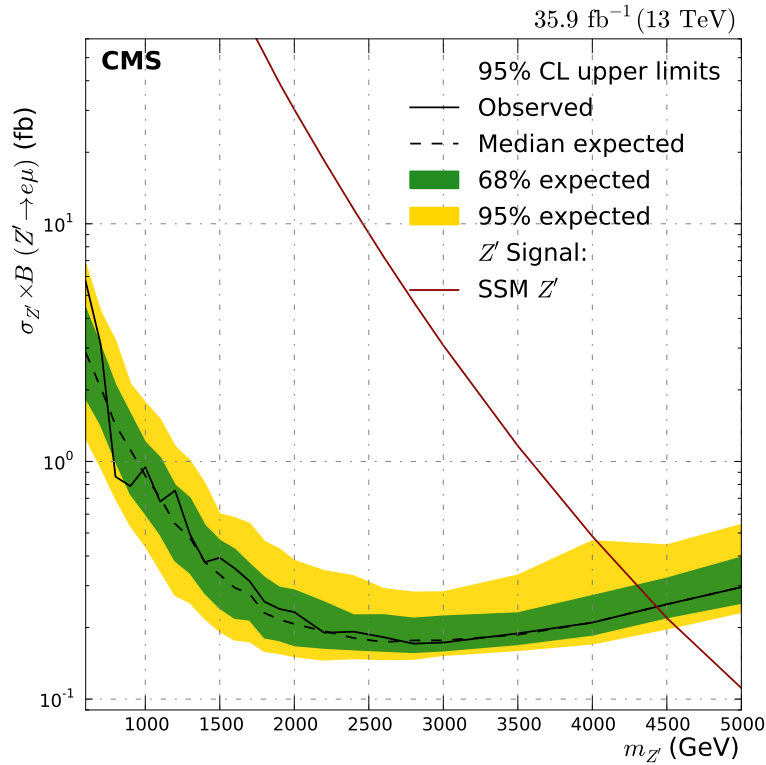


Figure 2.26: 95% C.L. expected limit and observed limit for the SSM Z' signal in the $e\mu$ channel. [134]

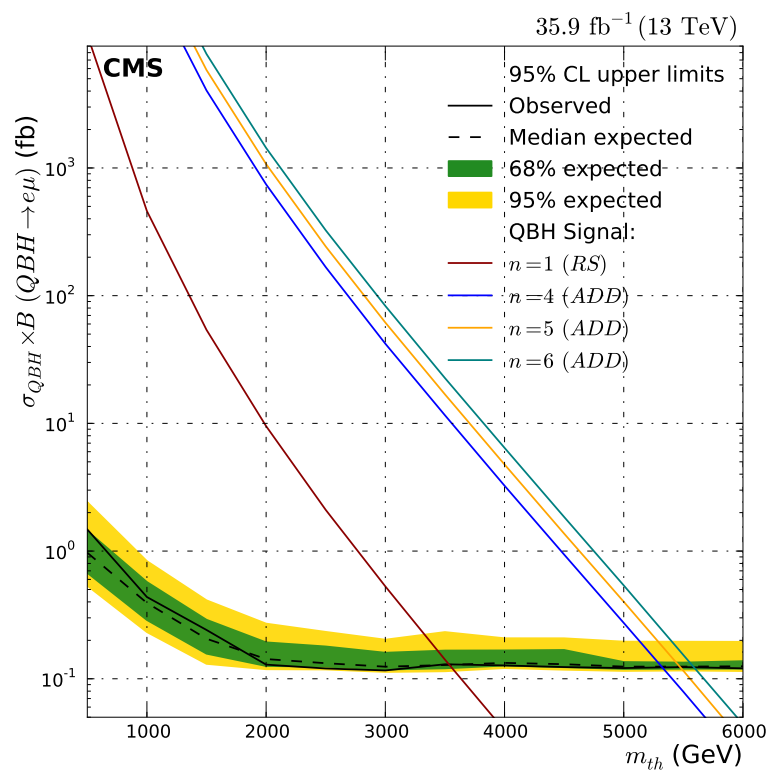


Figure 2.27: 95% C.L. expected limit and observed limit for the QBH signal in the $e\mu$ channel for all events. [134]

2.9 Chapter summary and personal contributions

A search for heavy states decaying into a $e\mu$ pair has been carried out using 35.9 fb^{-1} of proton-proton collision data recorded with the CMS detector at a center of mass energy of 13 TeV. Good agreement is observed between the data and the Standard Model expectation. Limits are set on the resonant production of τ sneutrinos ($\tilde{\nu}_\tau$) in R-parity violating supersymmetric models. For couplings $\lambda_{132} = \lambda'_{311} = 0.01$ and 0.1, a $\tilde{\nu}_\tau$ is excluded for masses below 1.7 and 3.8 TeV respectively, assuming it is the lightest supersymmetric particle. Lower limits of 5.3, 5.5, and 5.6 TeV are set on the threshold mass of quantum black holes in a model with 4, 5, and 6 large extra spatial dimensions, respectively. For the model with a single, warped extra spatial dimension, the lower limit on the threshold mass is 3.6 TeV. Also, a Z' boson with a 10% branching fraction to the $e\mu$ channel is excluded for masses below 4.4 TeV. In all cases, the results of this search improve the previous lower limits by about 1 TeV [140].

In this analysis, I have measured the individual trigger efficiencies and tested the efficiencies with various combinations. I have checked the mass resolutions of signal samples. I have synchronized the final selected event list in the signal region as a cross-check. I have estimated the QCD+jet contribution using the data-driven “fake-rate” and “same-sign” methods.

The analysis described in this Chapter has been published:

“Search for lepton-flavor violating decays of heavy resonances and quantum black holes to $e\mu$ final states in proton-proton collisions at $\sqrt{s} = 13 \text{ TeV}$ ”

CMS Collaboration

Journal of High Energy Physics, 04 (2018) 073

Chapter 3

Search for high mass resonances in dielectron final states with CMS 2016 and 2017 data

High mass neutral resonances decaying to lepton pairs is one of the most striking signatures of the physics beyond the Standard Model. There are a variety of theories that try to address such a process and try to extend the understanding of particle physics at the TeV scale. Examples include a new heavy Z boson-like particle, denoted Z' , such as the Z'_ψ boson of the GUT and Z'_{SSM} boson of the sequential Standard Model. Another example is the Kaluza-Klein graviton (GKK) of the Randall-Sundrum (RS) [8] model which would give a spin-2 dilepton resonance. These models have been described in Section 1.2.2.

3.1 Data and simulation samples

3.1.1 Data

This analysis first uses $\sqrt{s} = 13$ TeV LHC proton-proton collision data collected by the CMS experiment in 2016 and then updates results with CMS 2017 data.

3.1.2 SM background samples

A number of different Monte Carlo (MC) simulation samples are used in this analysis. The dominant background in this search is the Drell-Yan (DY) process. The simulated DY background is generated with POWHEG v2 [144, 145, 146, 147, 148, 149] from next-to-leading order (NLO) matrix elements using the NNPDF3.0 [150] PDF set, and with PYTHIA 8.205 [151] for parton showering and hadronization. The DY cross section at NLO is corrected to next-to-next-leading order (NNLO) in perturbative quantum chromodynamics by using a dilepton invariant mass dependent K -factor according to the predictions of the FEWZ 2.1.b2 program [152]. Another background arises from a $\gamma\gamma$ initial state via t and u channel processes. The photon-induced (PI) process produces two leptons

3. SEARCH FOR HIGH MASS RESONANCES IN DIELECTRON FINAL STATES WITH CMS 2016 AND 2017 DATA

in the final state [153, 154]. This contribution is included in the K -factor that corrects the DY NLO cross section.

The $t\bar{t}$, tW and WW backgrounds are simulated using POWHEG v2, with parton showering and hadronization described by PYTHIA 8.205. The NNPDF3.0 PDF set is used for all these samples. The $t\bar{t}$ cross section is calculated at NNLO with TOP++ [155] assuming a top quark mass of 172.5 GeV. The inclusive diboson processes WZ, and ZZ are simulated at leading order (LO) using the PYTHIA 8.205 program. The productions of $DY\tau^+\tau^-$ and W +jets are simulated at LO with MADGRAPH5_aMC@NLO version 2.2.2 [156] program.

3.1.3 Signal samples

In this analysis, the Z'_ψ signal events are generated at a mass point of 3000 GeV, and the graviton events are generated at different mass points from 250 GeV to 4000 GeV. In all samples the high-mass resonances decay to electron and muon pairs. Both signal samples are generated using the PYTHIA 8.205 program with the NNPDF3.0 PDFs. The Z'_ψ samples are used to create simulated peaks in the dilepton mass plots and the DY samples are used in high masses to model the Z' , since the dilepton behavior in this region is identical in the two cases.

3.2 Tag and probe method

A widely known method called “tag and probe” is used on the $Z \rightarrow ee$ events in order to calculate the efficiency of a certain selection. We first select a good electron as a “tag”, which should pass the criteria to make sure the selected events are pure enough for our measurement. Then we measure the efficiency of interested cut using the second electron called “probe” by calculating the ratio of the passed probe to all probe. In this analysis, we measure the trigger efficiencies for data, the HEEP ID V7.0 efficiencies for both data and MC using the tag and probe method.

3.3 Trigger strategy

The primary trigger for this analysis is a double electron trigger which requires the electron having the transverse energy $E_T > 33$ GeV with loose ID requirement. And for the data-MC efficiency scale factor study, the events are required to pass the single electron trigger with $E_T > 27$ GeV and absolute value of pseudorapidity $|\eta| < 2.1$.

The trigger efficiencies are measured using tag and probe method and fitted using function:

$$f(E_T) = 0.5 \cdot A0 \cdot \left(1 + \operatorname{erf}\left(\frac{E_T - A1}{\sqrt{2} \cdot A2}\right)\right) + 0.5 \cdot B0 \cdot \left(1 + \operatorname{erf}\left(\frac{E_T - B1}{\sqrt{2} \cdot B2}\right)\right)$$

where the A0 and B0 parameters can be interpreted as the efficiency at the plateau, the A1 and B1 as the value where the efficiency reaches half maximum and A2 and B2 as the turn on of the curve.

Figure 3.1 shows the turn on of the cut $E_T > 33$ GeV cut and this is used to weight the Monte Carlo events

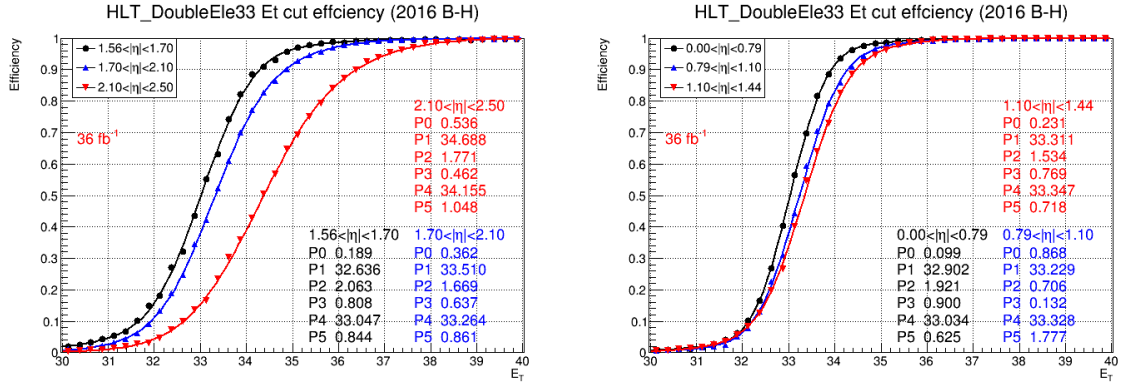


Figure 3.1: The efficiency for electron in the barrel (top) and endcap (bottom) passing HEEP V7.0 to match to pass an online cut $E_T > 33$ GeV on a L1 unseeded HLT supercluster.

3.4 Event selection

Electron candidates are required to pass the high energy electron pairs (HEEP) selection V7.0 already listed in Table 2.1 in the chapter above. We keep only the pair of the two largest E_T electrons in case there are more than two good electron candidates inside one event. In order to reduce the background from multi-jet events, we require at least one of the two selected electron candidates must be in the ECAL barrel region. This also allows the endcap-endcap events to be used as a control sample for the QCD background estimate. Dielectron pairs are not required to be oppositely charged as this leads to a significant efficiency loss at high invariant mass due to charge misidentification at high E_T [157].

3.5 HEEP ID scale factors

In order to make the selection condition of MC events same as that of data, we consider a scale factor for the HEEP ID selection efficiency which is calculated using the tag and probe method.

3.5.1 HEEP ID efficiencies

We select a tag electron with the requirements to pass the HEEP ID V7.0, to be in barrel, and to match to a trigger path that requires an electron to have $E_T > 27$ GeV and to pass tight ID.

We select only the tag and probe pair in the mass range $[70, 110]$ GeV, where we get a very clear peak around Z mass. Most of the selected events have real electrons from the decay of Z boson.

We define the efficiency as following:

$$\epsilon_{\text{HEEP}} = \frac{N(\text{probes passing HEEP ID})}{N(\text{probes all})},$$

3. SEARCH FOR HIGH MASS RESONANCES IN DIELECTRON FINAL STATES WITH CMS 2016 AND 2017 DATA

where $N(\text{probes all})$ is the total number of all selected probes, $N(\text{probes passing HEEP ID})$ is the total number of selected probes which pass the HEEP V7 selection criteria.

All Standard Model contributions are estimated from MC except for the QCD process that is estimated using the data-driven “same-sign” method, which has been described in Section 2.3.2.

We also separate the events to different η -categories because of the different ID efficiencies in barrel and endcaps.

3.5.2 HEEP ID and scale factors

The HEEP ID efficiencies for data and MC are shown as functions of probe E_T in figure 3.2, the efficiencies as functions of other variables can be found in Appendix C. The ratio of data to MC efficiencies is shown in the bottom pad. In order to check if the DY events give a smooth curve as expected, the DY efficiency is compared to data where the non-DY contributions are subtracted in the right plot of figure 3.2.

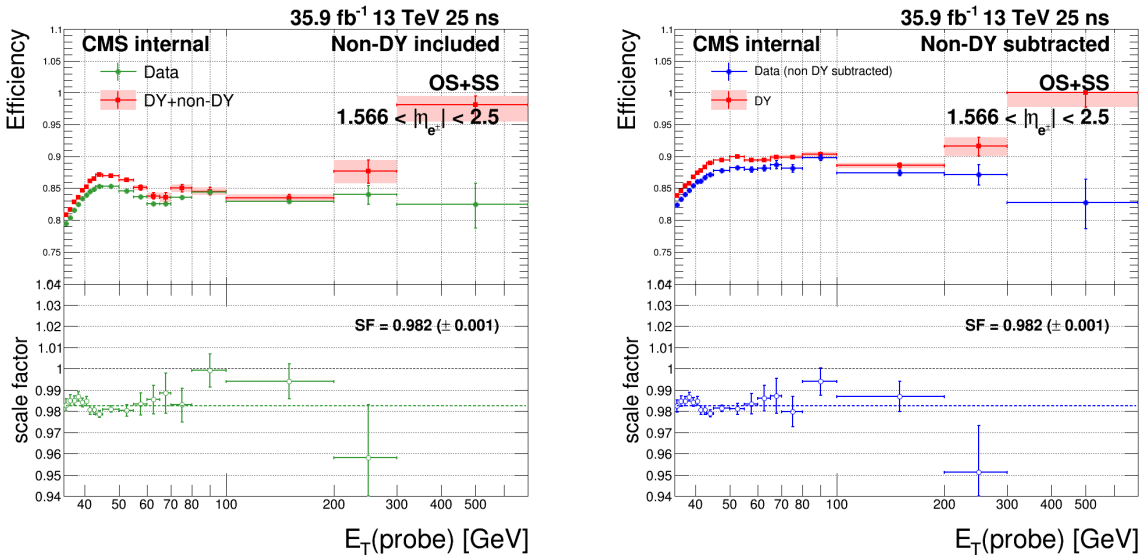


Figure 3.2: The HEEP ID efficiencies get from data and MC as functions of probe E_T . The left plot is for non-DY included case while the right plot is for the non-DY excluded case. [141]

The non-DY processes contribute to the dominant systematic uncertainty on the scale factor. We consider 10% for $t\bar{t}$ and 50% for $W + \text{jets}$ on the cross sections, respectively. We consider a large uncertainty of 50% for the QCD process. Besides, we still consider the uncertainty of the pile-up weights although it is negligible. Table 3.1 gives the efficiencies and scale factors for HEEP ID in both non-DY included/ excluded cases.

	Barrel	Endcap
Data	$86.13\% \pm 0.01\%(stat.)$	$83.38\% \pm 0.03\%(stat.)$
DY + non-DY	$88.65\% \pm 0.03\%(stat.)$	$84.85\% \pm 0.09\%(stat.)$
Scale factor	$0.972 \pm 0.000(stat.) \pm 0.006(syst.)$	$0.983 \pm 0.001(stat.) \pm 0.007(syst.)$
Data - non-DY	$87.92\% \pm 0.03\%(stat.)$	$85.83\% \pm 0.09\%(stat.)$
DY	$90.50\% \pm 0.01\%(stat.)$	$87.35\% \pm 0.03\%(stat.)$
Scale factor	$0.971 \pm 0.000(stat.) \pm 0.006(syst.)$	$0.983 \pm 0.001(stat.) \pm 0.007(syst.)$

Table 3.1: The HEEP ID efficiencies from data and MC and the scale factors. The top part is for non-DY included case while the bottom part is for the non-DY excluded case. [141]

3.6 Mass resolution and scale

We estimate the mass resolution which is used for the signal model definition by two steps: a data-MC comparison at Z peak mass range ($60 \text{ GeV} < m_{ee} < 120 \text{ GeV}$), and an MC-only study at high mass range. In this section, we use the events that pass the event selection described above.

In the first step, we compare the invariant mass distributions of the electron pairs m_{ee} between the data and MC simulation at the Z peak mass range. We fit both distributions using a Breit-Wigner (BW) function convoluted with a double-sided crystal ball function (dCB). The dCB function is defined as a Gaussian core connected with two power-law functions on both sides. Then we obtain the dCB σ parameters from data and MC in different η -categories. We subtract the σ_{MC} which is from the fit to MC distribution off the σ_{data} which is from the fit to data in quadrature, the value is defined as $\sigma_{extra} = \sqrt{\sigma_{data}^2 - \sigma_{MC}^2}$. We also define a parameter (σ^{eff}) as the minimum window around the mean of the distribution which contains 68% of the total events in the distribution. The values of the parameter for barrel-barrel and barrel-endcap categories are shown in Table 3.2 and expressed in percentage of the PDG Z mass, where $M_Z = 91.187 \text{ GeV}$. Detailed figures could be found in Appendix.

Category	$\frac{\Delta M}{M} [\%]$	$\sigma_{data} [\%]$	$\sigma_{MC} [\%]$	$\sigma_{extra} [\%]$	$\sigma_{data}^{eff} [\%]$	$\sigma_{MC}^{eff} [\%]$	$\sigma_{extra}^{eff} [\%]$
BB	-0.19 ± 0.02	1.45 ± 0.00	1.20 ± 0.03	0.81 ± 0.04	3.72	3.44	1.42
BE	-0.40 ± 0.02	2.49 ± 0.01	2.15 ± 0.03	1.26 ± 0.05	4.63	4.07	2.19

Table 3.2: The fit results and the calculated data-MC correction factors for barrel-barrel (BE) and barrel-endcap (BE) channels. [141]

In the second step of the study, we use only the MC events in the generated mass range m_{ee}^{gen} 50 - 4500 GeV. We define a variable $resolution = \frac{m_{reco} - m_{gen}}{m_{gen}}$ to count the difference between the reconstructed and generated invariant mass. We fit the distribution of $resolution$ as a function of m_{gen} with a ‘‘Cruiff function’’ using a binned maximum-likelihood method, The Cruiff function is a function with Gaussian core, connected with an exponential tail on each side. The sigma parameter of the Cruiff function σ_{fit} is added in quadrature with the σ_{extra} parameter. Results in different

3. SEARCH FOR HIGH MASS RESONANCES IN DIELECTRON FINAL STATES WITH CMS 2016 AND 2017 DATA

categories are shown in figure 3.3, the binning of the x-axis is chosen to have a reasonable amount of statistics and a good quality of fits.

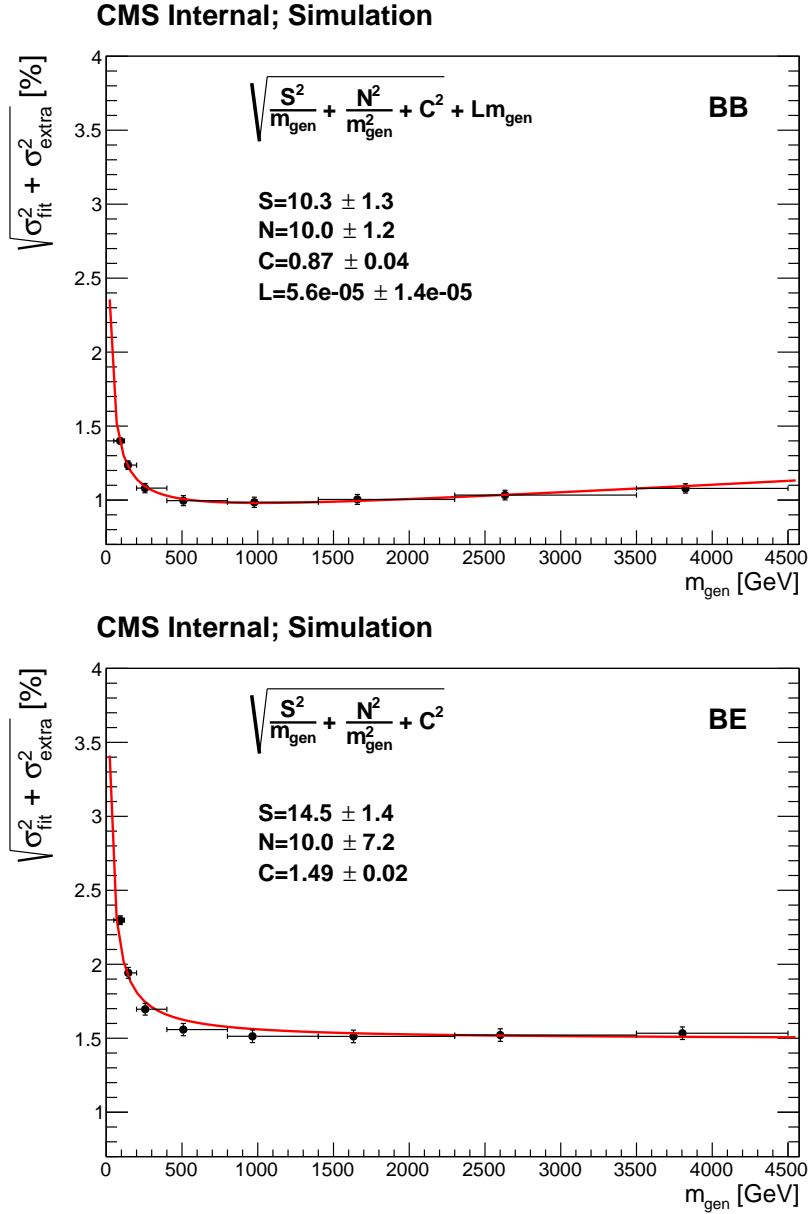


Figure 3.3: Mass resolution as a function of the m_{gen} for the barrel-barrel (top) and barrel-endcap (bottom) channels. [141]

3.7 Standard model backgrounds

The dominant backgrounds from the Standard Model prediction in this analysis are listed and checked in this section.

The most significant background is from the Drell-Yan process, which is irreducible because the new physics could interfere with this process.

The second most important background can also provide two real electrons but decay from different parent particles, such as the $t\bar{t}$, WW , WZ , ZZ , tW and $Z/\gamma^* \rightarrow \tau^+\tau^-$ events.

The third background is the jet background, mainly arising from W +jets and multi-jets, where the reconstruct algorithm misidentifies the jets as electrons.

3.7.1 SM Drell-Yan background

The Standard Model Drell-Yan background events are simulated by the POWHEG event generator and corrected with the trigger efficiency and the electron energy scale/smearing. The MC events are weighted corresponding to the luminosity of 35.9 fb^{-1} , the ee invariant mass distributions in barrel-barrel region and barrel-endcap region are shown in figure 3.13.

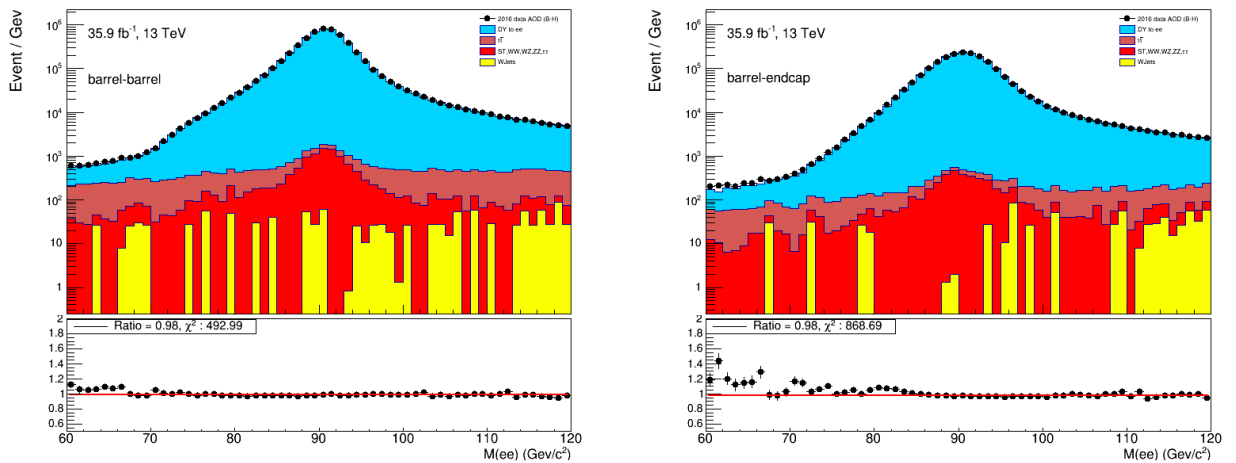


Figure 3.4: Dielectron invariant mass distributions for data and MC, for the barrel-barrel (left) and barrel-endcap (right) channels. The MC events are corrected with all scale factors and are normalized to the luminosity of data.

A cross section measurement on the Drell-Yan process is shown in Table 3.3, which is in good agreement with the theoretical value.

Variable	Barrel-barrel	Barrel-endcap
Nr data events (E corr)	5760345 ± 2400	2051759 ± 1432
Nr expect bkg	32805	11336
MC acc \times eff	0.0880 ± 0.001	0.0315 ± 0.001
Data/MC ID RECO SF	0.979 ± 0.001	0.985 ± 0.001
Data/MC ID Eff SF	0.943 ± 0.001	0.953 ± 0.001
Luminosity	35867 pb^{-1}	35867 pb^{-1}
Cross-sec (E corr)	$1967 \pm 3 \text{ (stat)} \pm 51 \text{ (lumi)} \text{ pb}$	$1922 \pm 3 \text{ (stat)} \pm 50 \text{ (lumi)} \text{ pb}$

Table 3.3: The measured cross section of Drell-Yan process using the events $[60 < M_{ee} < 120] \text{ GeV}$.

3. SEARCH FOR HIGH MASS RESONANCES IN DIELECTRON FINAL STATES WITH CMS 2016 AND 2017 DATA

The uncertainty due to the PDFs is found to be from 1.2% to 20% as dielectron mass increases from 0.2 to 6 TeV.

3.7.2 $t\bar{t}$ and $t\bar{t}$ -like background

We study the $t\bar{t}$ and $t\bar{t}$ -like background from MC simulations as well. They are all flavor-symmetric processes which mean that the branching ratio to a pair of leptons with different flavors, $e\mu$, should be twice as large as the branching ratio to a pair of electrons, e^+e^- . Thus we can validate the $t\bar{t}$ and $t\bar{t}$ -like simulations using the distributions of $e\mu$ pairs.

We select the electron and muon using the same criteria described in the Chapter 2, and keep only the highest invariant mass $e\mu$ pair.

The $e\mu$ invariant mass distribution is shown in figure 3.5. All the backgrounds are from MC simulation except for the jet+QCD, which is estimated using the “fake rate” data-driven method, which is introduced in Section 2.3.2. The predictions from data and simulation are in agreement.

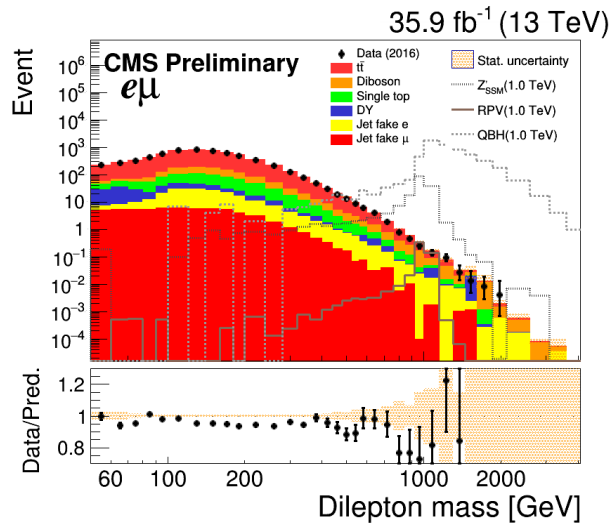


Figure 3.5: The $e\mu$ invariant distribution.

3.7.3 Jet background

The jet background where the jets are misidentified as electrons is the smallest one of the significant Standard Model backgrounds in this search and is estimated using the “fake rate” method described in the chapter above already.

There are the possibilities that one or both electrons come from the misidentified jet(s). The $1FR$ estimate includes the backgrounds from W +jets, γ +jets, and dijet, but due to combinatorial effects, the $1FR$ estimate overestimates the dijet contribution by a factor of 2. The dijet contribution can be estimated by selecting the events with both electrons passing the FR pre-selection but failing the HEEP selection. This is referred to as the $2FR$ estimate and the events are weighted by $FR_1/(1 -$

$FR_1) \times FR_2 / (1 - FR_2)$. This estimate is then subtracted off the $1FR$ estimate to avoid the double counting.

The contribution of misidentified jets to the total background is only around (1-3%), therefore even with large uncertainties up to 50%, it has still a negligible effect on the statistical analysis of the data.

3.8 Invariant mass plot and limit plot

The electron pair mass spectra and the integral of the mass spectra are shown in figures 3.6, 3.7, and 3.8 for the barrel-barrel, barrel-endcap, and combined channels, respectively. The distribution of data is consistent with the prediction of MC simulations.

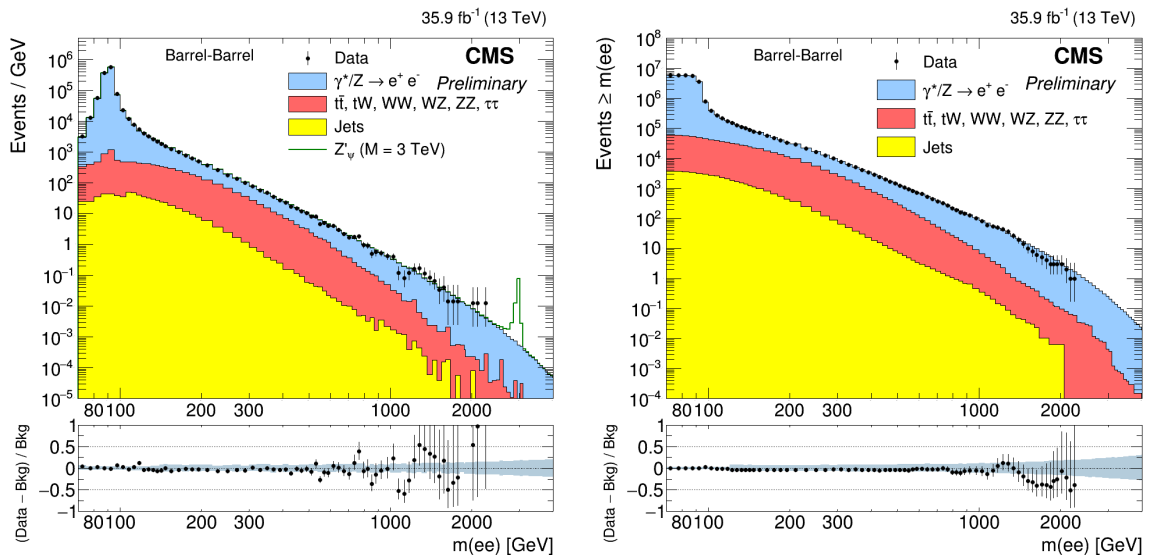


Figure 3.6: The observed dielectron mass spectrum (left) and the integral of the measured dielectron mass spectrum (right) for the barrel-barrel region together with the predicted Standard Model backgrounds. [141]

3.8.1 Systematic uncertainties

Results are presented as a ratio of cross sections at high mass to those at the Z peak. The main uncertainties are from the simulation by MC to the electron efficiency at high E_T and NLO and PDF effects on the Drell-Yan background. In the figure of HEEP ID efficiency, the data/MC efficiency appears flat in both the barrel and the endcap, where uncertainties of 3% and 5% are assigned for the electron ID efficiency. The PDF uncertainties range from 1.5% at 400 GeV to 19.9% at 6 TeV. The jet background uncertainty is 50% and the uncertainty on the non DY background is taken to be 7% based on cross-section uncertainties. The normalization to the Z peak is estimated to have an uncertainty of 2%. The energy scale uncertainty is assigned at 1% to 2%.

3. SEARCH FOR HIGH MASS RESONANCES IN DIELECTRON FINAL STATES WITH CMS 2016 AND 2017 DATA

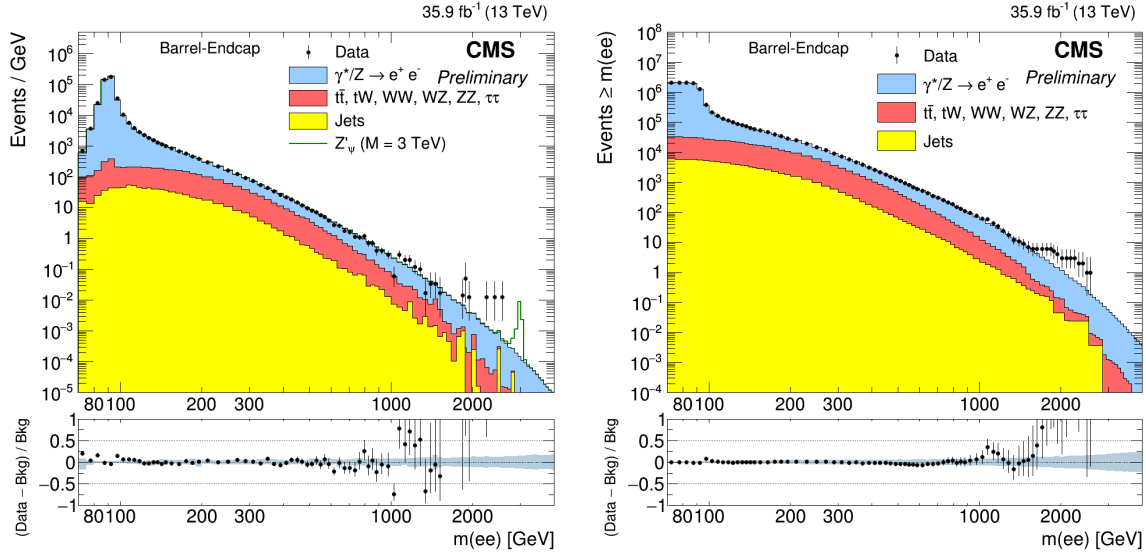


Figure 3.7: The observed dielectron mass spectrum (left) and the integral of the measured dielectron mass spectrum (right) for the barrel-endcap region together with the predicted Standard Model backgrounds. [141]

3.8.2 Statistical methods

A framework known as ExoSt has been developed to estimate the limit of the dilepton searches at CMS, allowing combinations of different final states and different center of mass energies. This is based on the RooStats and RooFit framework [159] and it is fully described in Ref. [160]. The model considers a zero width resonance convoluted with a resolution function.

The limit setting method is a Bayesian unbinned likelihood with a flat prior for the signal cross section and log normal priors for the signal and background uncertainties, which is similar to the one introduced in Section 2.7. The integration uses the Metropolis-Hasting algorithm [161, 162]. Due to different resolutions and background relative compositions, the barrel-barrel and barrel-endcap regions are treated as separate channels in the likelihood.

3.8.3 Limit inputs

The limit input requires parametrization of the resolution function, the acceptance \times efficiency and the background shape. Additionally, the number of events in the Z peak together with the acceptance \times efficiency are required to obtain the luminosity. Since the limits are normalized to the Z peak, any E_T independent effects on the efficiency cancel and are not included in the acceptance \times efficiency parametrization nor the Z peak acceptance \times efficiency. The effects not included are the E_T dependent effects such as the trigger efficiency. Figure 3.9 shows the acceptance \times efficiency fits and figure 3.10 shows the parametrization of the background shape. Table 3.4 shows the other inputs to the limits such as the number of data events and acceptance at the Z peak.

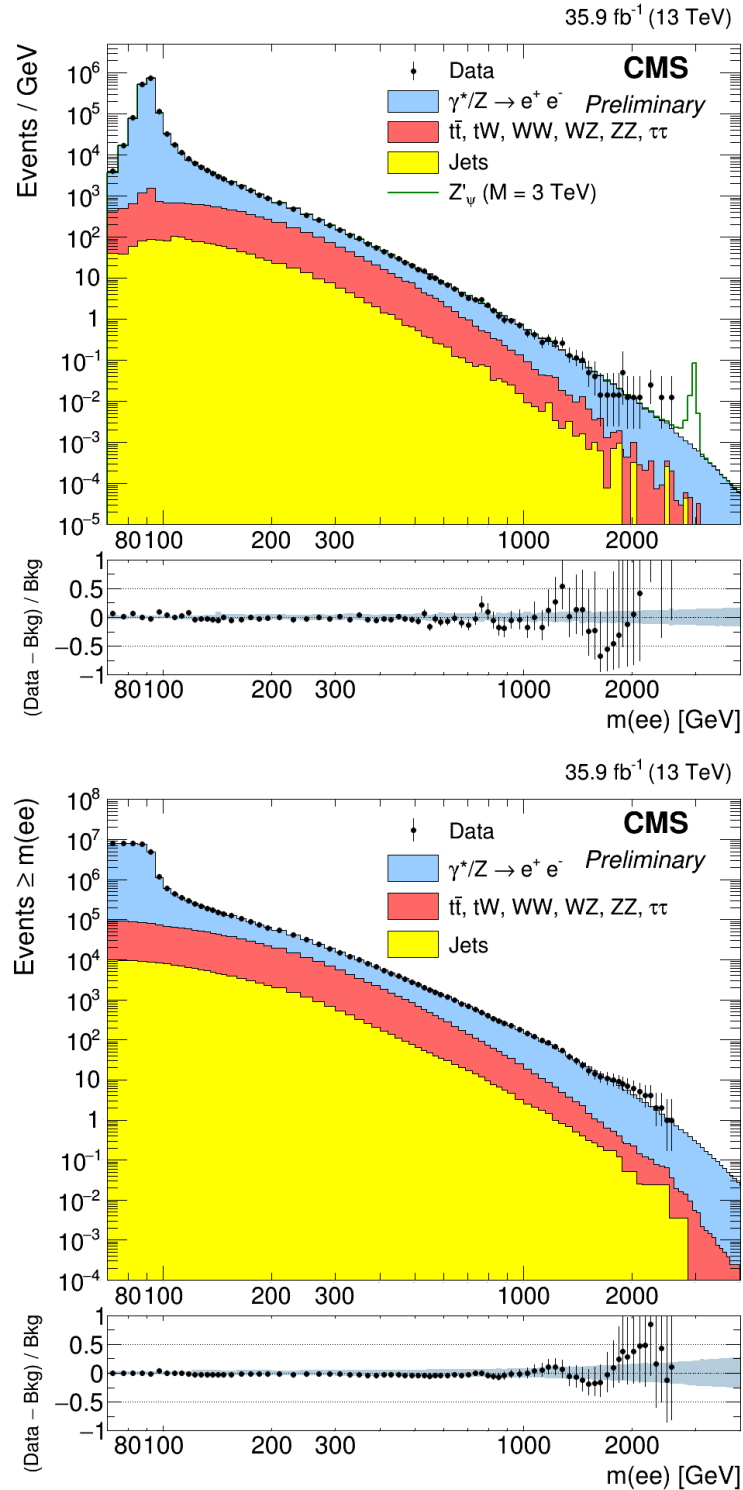


Figure 3.8: The observed dielectron mass spectrum (top) and the integral of the measured dielectron mass spectrum (bottom) for the sum of barrel-barrel and barrel-endcap regions together with the predicted Standard Model backgrounds. [141]

3. SEARCH FOR HIGH MASS RESONANCES IN DIELECTRON FINAL STATES WITH CMS 2016 AND 2017 DATA

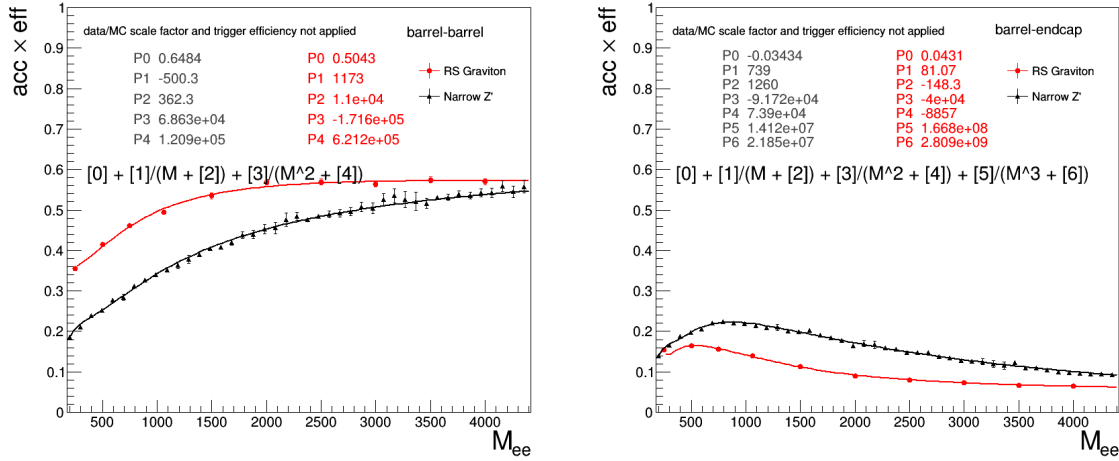


Figure 3.9: The acceptance \times efficiency for a spin-1 or spin-2 particle selected by the analysis in the barrel-barrel region (left) and barrel-endcap region (right) as a function of E_T .

Variable	EB-EB	EB-EE
N_Z (60-120 GeV)	5730975	2042478
Z acc \times eff (60-120 GeV)	0.0895	0.0318
Z' acc \times eff / Z acc \times eff err	6%	8%
$N_{data} > 150$ GeV	70685	55096
$N_{data} > 200$ GeV	28784	25581
Energy scale uncertainty	2%	1%

Table 3.4: The input parameters to the limit setting code. All masses are in units of GeV/ c^2 . All E_T independent effects on the MC efficiencies are excluded.

3.8.4 Results

A search for high mass resonances in the dielectron final state with 2016 CMS data corresponding to the integrated luminosity 35.9 fb^{-1} is performed, all selected events perform within the prediction of Standard Model. The upper limit of the cross section ratio of $Z' \rightarrow ee$ to $Z \rightarrow ee$ is calculated and compared to several predictions provided by new-physics scenarios.

Figure 3.11 shows the observed and expected 95% C.L. on the on-shell cross sections for the Z'_{SSM} and Z'_{ψ} , and figure 3.12 for the graviton, respectively, with the combined barrel-barrel and barrel-endcap categories. The observed and expected lower limits on the new particle masses are shown in Tables 3.5 and 3.6.

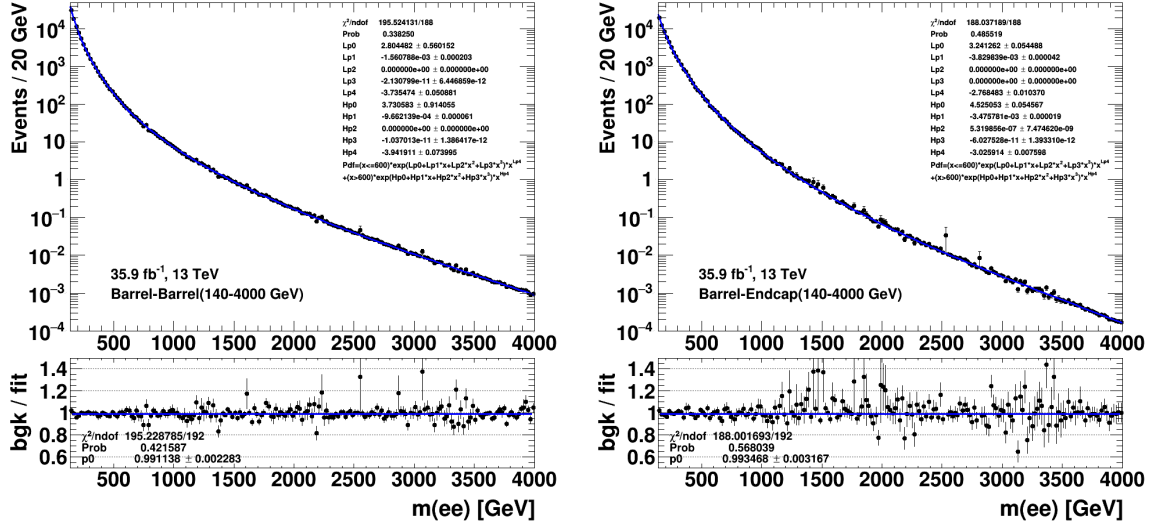


Figure 3.10: The total SM background together with the fitted functional form used to enter it into the limit setting tools for the barrel-barrel (left) and barrel-endcap (right) channels. [141]

Channel	Z'_{SSM}		Z'_ψ	
	Obs. [TeV]	Exp. [TeV]	Obs. [TeV]	Exp. [TeV]
ee	4.1	4.1	3.45	3.45
ee + $\mu\mu$	4.5	4.5	3.9	3.9

Table 3.5: The observed and expected 95% C.L. lower limits on the masses of spin-1 Z'_{SSM} and Z'_ψ bosons, assuming a signal width of 0.6% (3.0%) of the resonance mass for Z'_ψ (Z'_{SSM}). The results of only ee channel (top) and combination of ee and $\mu\mu$ channels are (bottom) are presented respectively.

Channel	$k/\overline{M}_{Pl} = 0.01$		$k/\overline{M}_{Pl} = 0.01$		$k/\overline{M}_{Pl} = 0.01$	
	Obs. [TeV]	Exp. [TeV]	Obs. [TeV]	Exp. [TeV]	Obs. [TeV]	Exp. [TeV]
ee	1.85	1.85	3.30	3.30	3.90	3.90
ee + $\mu\mu$	2.10	2.05	3.65	3.60	4.25	4.25

Table 3.6: The observed and expected 95% C.L. lower limits on the masses of spin-2 resonances with widths equal to 0.01, 0.36 and 1.42 GeV corresponding to coupling parameters k/\overline{M}_{Pl} of 0.01, 0.05, and 0.10. The results of only ee channel (top) and combination of ee and $\mu\mu$ channels are (bottom) are presented respectively.

3. SEARCH FOR HIGH MASS RESONANCES IN DIELECTRON FINAL STATES WITH CMS 2016 AND 2017 DATA

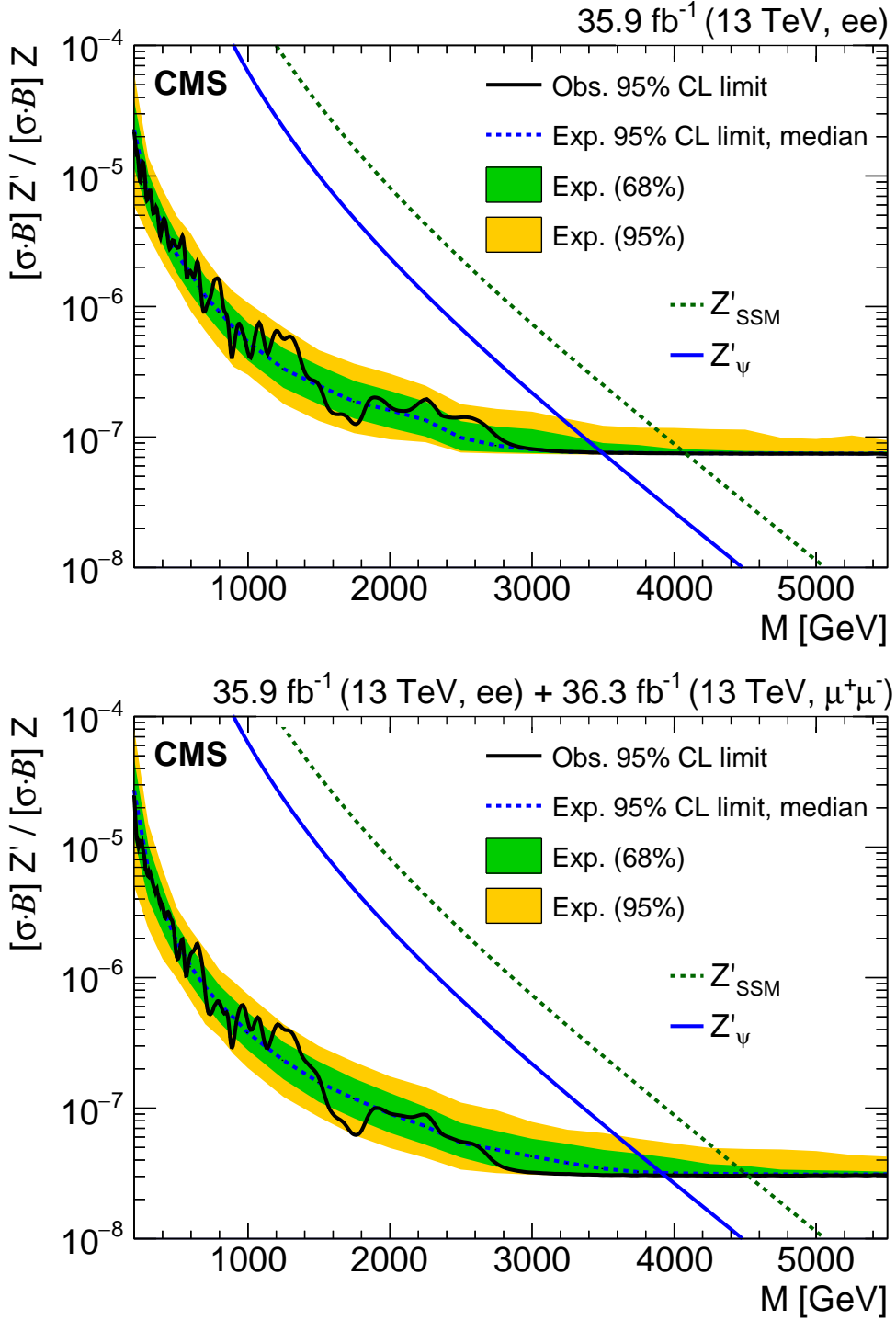


Figure 3.11: The expected limits obtained at a 95% confidence level on the on-shell cross section for a Z' assuming a signal width of 0.6% of the resonance mass. The results of only ee channel (top) and combination of ee and $\mu\mu$ channels (bottom) are presented. [141]

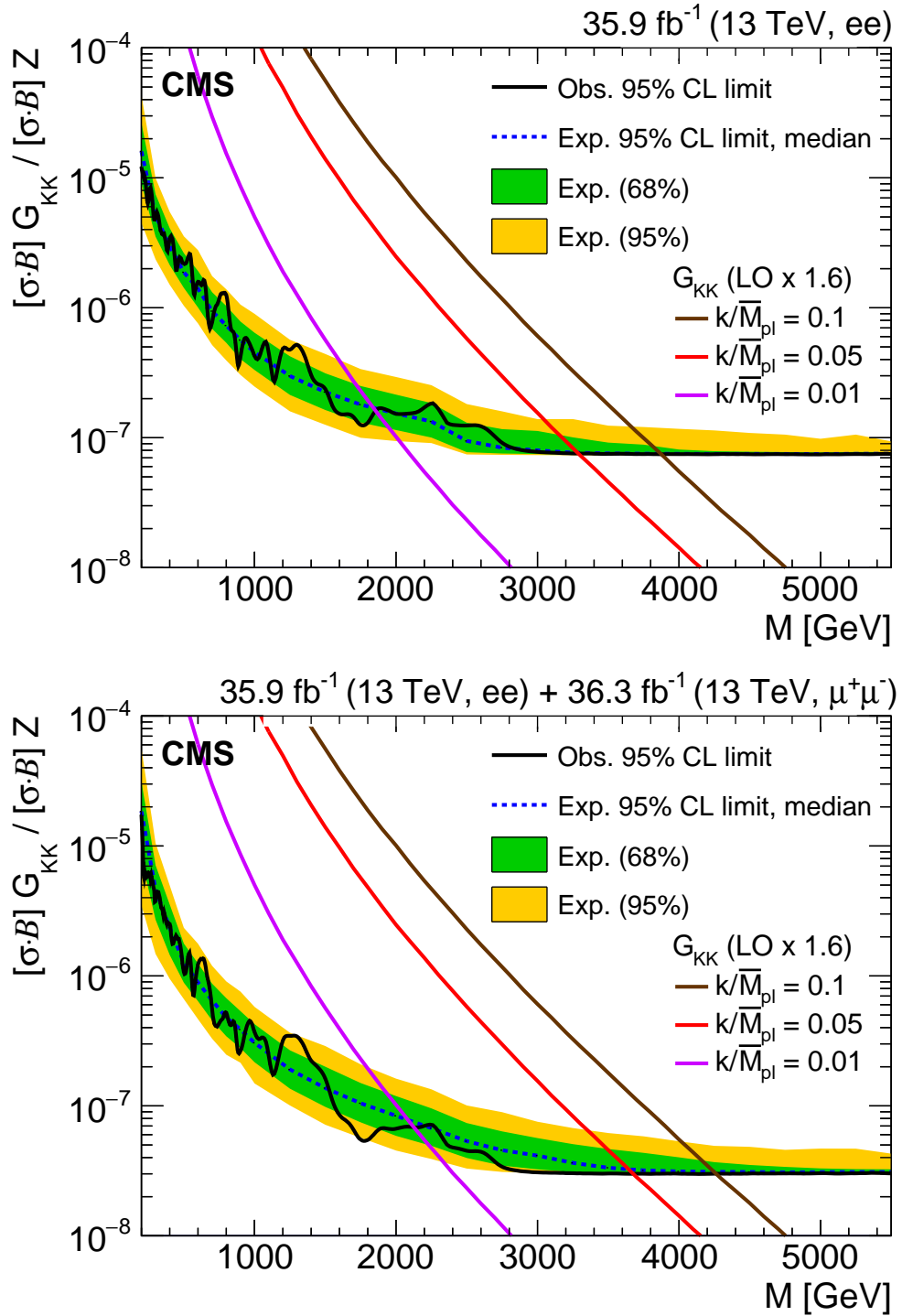


Figure 3.12: The expected limits obtained at a 95% confidence level on the on-shell cross section for spin-2 graviton with widths equal to 0.01, 0.36, and 1.42 GeV corresponding to coupling parameters k/\bar{M}_{Pl} of 0.01, 0.05, and 0.10. The results of only ee channel (top) and combination of ee and $\mu\mu$ channels (bottom) are presented. [141]

3. SEARCH FOR HIGH MASS RESONANCES IN DIELECTRON FINAL STATES WITH CMS 2016 AND 2017 DATA

3.9 Update with CMS 2017 data

A search for high mass resonances in the dielectron final state with 2017 CMS data corresponding to the integrated luminosity 41.4 fb^{-1} is performed as well. The analysis strategy is similar to the 2016 analysis and no evidence for a significant deviation from the Standard Model expectation is observed. The mass spectrum is shown in figure 3.13. Upper bounds are set on the masses of hypothetical particles that arise in new-physics scenarios for only electron channel with 2017 data and combination of electron channel with 2016, 2017 data and muon channel with 2016 data in figure 3.14 and Table 3.7.

Channel	Model	Obs. limit (TeV)	Exp. limit (TeV)
ee (2017)	Z'_{SSM}	4.10	4.15
	Z'_{ψ}	3.35	3.55
ee (2016 and 2017) + $\mu\mu$ (2016)	Z'_{SSM}	4.7	4.7
	Z'_{ψ}	4.1	4.1

Table 3.7: The observed and expected 95% CL lower limits on masses of the spin-1 Z'_{SSM} and Z'_{ψ} bosons for 2017 dataset and combination with 2016. The limits are rounded to the nearest 50 GeV.

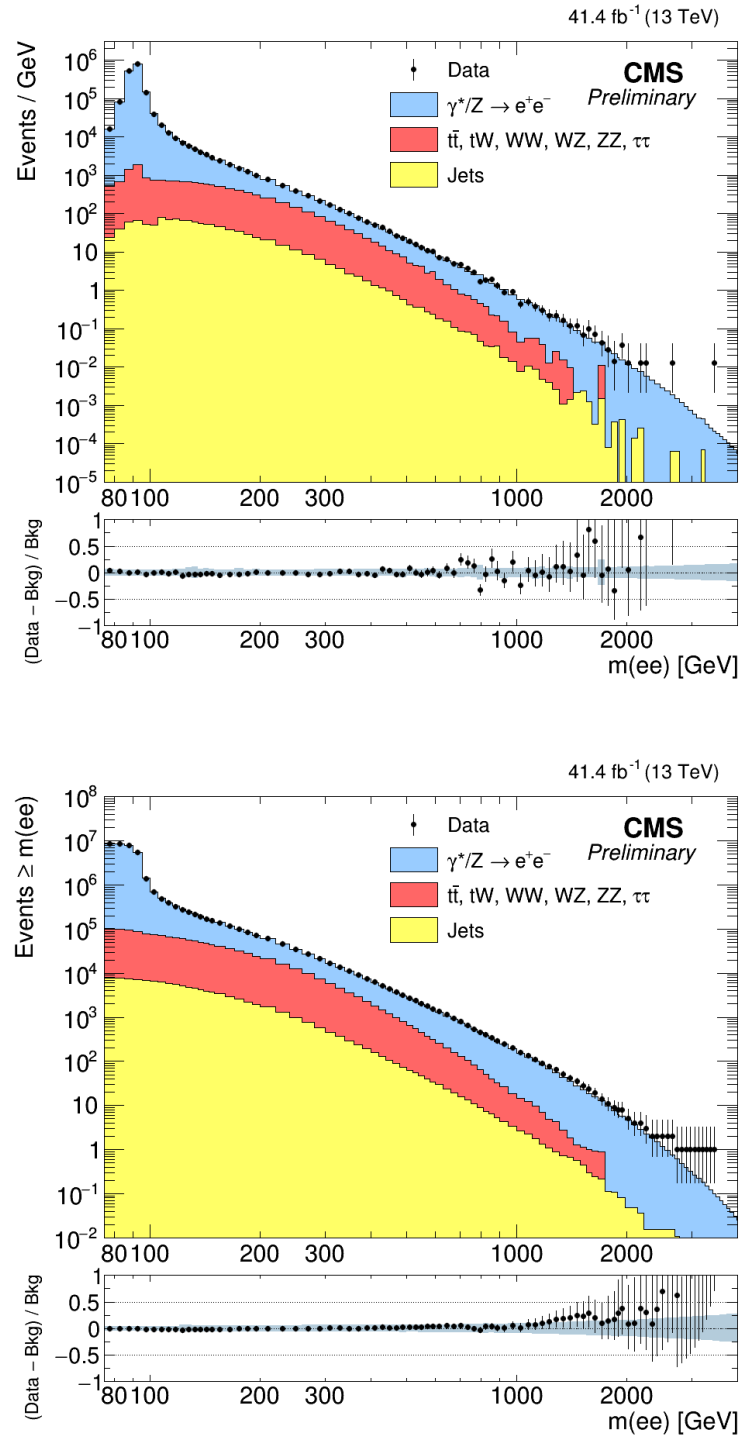


Figure 3.13: The observed dielectron mass spectrum (top) and the integral of the measured dielectron mass spectrum (bottom) for the sum of barrel-barrel and barrel-endcap regions together with the predicted Standard Model backgrounds. [142]

3. SEARCH FOR HIGH MASS RESONANCES IN DIELECTRON FINAL STATES WITH CMS 2016 AND 2017 DATA

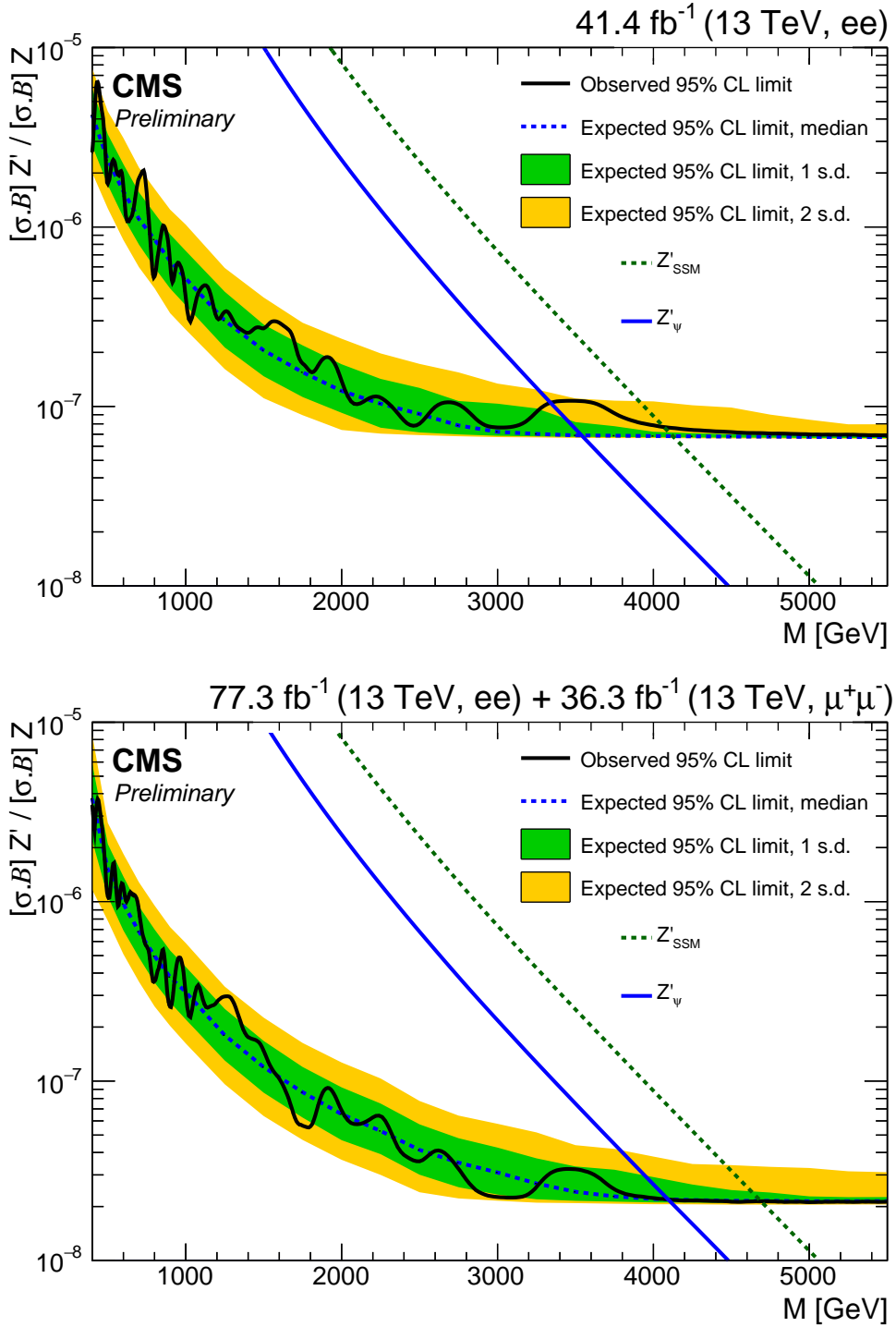


Figure 3.14: The expected and observed limits obtained at 95% confidence level on the on-shell cross section for a Z' for dielectron channel with 2017 dataset (top) and in combination with 2016 results for dimuon and dielectron channels (bottom) [142].

3.10 Chapter summary and personal contributions

A search for narrow resonances in dielectron invariant mass spectra has been performed using data recorded in 2016 and 2017 from proton-proton collisions at $\sqrt{s} = 13$ TeV. The integrated luminosity for the 2016 sample is 35.9 fb^{-1} and for 2017 sample is 41.4 fb^{-1} . We also combined the dimuon channel data collect in 2016 corresponding to 36.3 fb^{-1} . Observations are in agreement with Standard Model expectations. Upper limits at 95% confidence level on the product of a narrow-resonance production cross section and branching fraction to dileptons have been calculated in a model-independent manner to enable interpretation in the framework of models predicting a narrow dielectron or dimuon resonance.

Limits are set on the masses of various hypothetical particles. For the Z'_{SSM} particle which arises in the sequential Standard Model, and for the superstring-inspired Z'_{ψ} particle, 95% confidence level lower mass limits for the combination between 2016 + 2017 ee and 2016 $\mu\mu$ channels are found to be 4.7 TeV and 4.1 TeV, respectively. These limits extend the previous ones from CMS by 1.3 TeV in both models. The corresponding limits for Kaluza-Klein gravitons arising in the Randall-Sundrum model of extra dimensions with coupling parameters k/\bar{M}_{Pl} of 0.01, 0.05, and 0.10 are 2.10, 3.65, and 4.25 TeV, respectively. The limits extend previous published CMS results by 0.6 (1.1) TeV for a k/\bar{M}_{Pl} value 0.01 (0.10) [163].

In this analysis, I have measured the individual trigger efficiencies and provided the trigger turn on curve to weight MC simulated events. I have checked the contribution and shape of standard backgrounds from the Drell-Yan process and $t\bar{t}$ (-like) processes. I have provided the acceptance \times efficiency function of the signal samples.

The analysis described in this Chapter has been published:

“Search for high-mass resonances in dilepton final states in proton-proton collisions at $\sqrt{s} = 13$ TeV”

CMS Collaboration

Journal of High Energy Physics, 06 (2018) 120

3. SEARCH FOR HIGH MASS RESONANCES IN DIELECTRON FINAL STATES WITH CMS 2016 AND 2017 DATA

Chapter 4

Study exotic state $Y(4220)$ with BESIII data

4.1 $Y(4220)$ state in BESIII

The high precision cross section measurements and the study of these states in different final states in direct e^+e^- annihilation in the charmonium energy region from the BESIII experiment supply new insight into the Y-states properties.

In 2013, in the $e^+e^- \rightarrow \pi^+\pi^-h_c$ process, BESIII reported the cross section measurement at 13 center-of-mass (c.m.) energies from 3.9 to 4.2 GeV and found the magnitude of the cross sections is at the same order as that of $e^+e^- \rightarrow \pi^+\pi^-J/\psi$ but with a different line shape. The resonant structure at around 4.22 GeV is obvious but no observation on it [86]. A combined fit to the BESIII data together with CLEO-c measurement at 4.17 GeV [165] results in a resonant structure, $Y(4220)$, with a mass of (4216 ± 18) MeV and a width of (39 ± 32) MeV [166], different from any of the known Y and excited ψ states in this mass region [167].

In 2014, in the $e^+e^- \rightarrow \omega\chi_{c0}$ process, BESIII reported the cross section measurement at 9 c.m. energies from 4.21 to 4.42 GeV. By assuming the $\omega\chi_{c0}$ signals come from a single resonance, BESIII reported a resonant structure with the mass and width of $(4230 \pm 8 \pm 6)$ MeV and $(38 \pm 12 \pm 2)$ MeV, respectively, with the statistical significance that is more than 9σ [168]. This structure is in good agreement with the $Y(4220)$ observed in $e^+e^- \rightarrow \pi^+\pi^-h_c$ [166]. After that, a combined fits assuming the structures at 4.22 GeV are the same have been tried in Refs. [169, 170].

In 2016 and 2017, BESIII updated the measurements with higher energy data up to 4.6 GeV included, in both $e^+e^- \rightarrow \pi^+\pi^-h_c$ [171] and $e^+e^- \rightarrow \omega\chi_{c0}$ [172] processes. In addition, more data points are added even at low energy, although with low integrated luminosity, to further constrain the line shape in $e^+e^- \rightarrow \pi^+\pi^-h_c$ process. In the $e^+e^- \rightarrow \pi^+\pi^-h_c$ mode, the $Y(4220)$ was observed with improved significance together with a new structure, the $Y(4390)$. The resonant parameters are $M = (4218.4 \pm 4.0 \pm 0.9)$ MeV and $\Gamma = (66.0 \pm 9.0 \pm 0.4)$ MeV for the $Y(4220)$, and $M = (4391.6 \pm 6.3 \pm 1.0)$ MeV and $\Gamma = (139.5 \pm 16.1 \pm 0.6)$ MeV for the $Y(4390)$.

4. STUDY EXOTIC STATE Y(4220) WITH BESIII DATA

In 2005, the process $e^+e^- \rightarrow \pi^+\pi^-J/\psi$ at c.m. energies up to 5.0 GeV was first studied by the *BABAR* experiment [78], where the Y(4260) was observed. Then in 2007, Belle measured the cross sections of the same process at c.m. energies from 3.8 to 5.0 GeV, and reported that only the Y(4260) cannot describe the line shape satisfactorily [64]. Improved measurements with both *BABAR* [67] and Belle [66] full data samples confirmed the existence of non-Y(4260) component in $e^+e^- \rightarrow \pi^+\pi^-J/\psi$ process.

In 2017, in the $e^+e^- \rightarrow \pi^+\pi^-J/\psi$ process, BESIII reported a precise measurement at c.m. energies from 3.77 to 4.60 GeV using data samples with an integrated luminosity of 9 fb^{-1} [173]. The dominant resonant structure that called Y(4260) was found to have a mass of $(4222.0 \pm 3.1 \pm 1.4) \text{ MeV}$ and a width of $(44.1 \pm 4.3 \pm 2.0) \text{ MeV}$, in good agreement with the Y(4220) observed in $e^+e^- \rightarrow \pi^+\pi^-h_c$ [171] and $e^+e^- \rightarrow \omega\chi_{c0}$ processes. In addition, a new resonance with a mass of around 4.32 GeV is needed to describe the high precision data.

In 2017, in the $e^+e^- \rightarrow D^0D^{*-}\pi^+ + \text{c.c}$ process, BESIII reported a measurement at c.m. energies from 4.05 to 4.60 GeV with the samples [174], which is a significant improvement over the previous measurement reported by Belle in 2009 [175]. Two resonant structures in good agreement with the Y(4220) and Y(4390) observed in the $e^+e^- \rightarrow \pi^+\pi^-h_c$ process [171] are identified over a smoothly increasing non-resonant term which can be parametrized with a three-body phase space amplitude.

The cross sections of above four processes reported by BESIII are shown in figure 4.1.

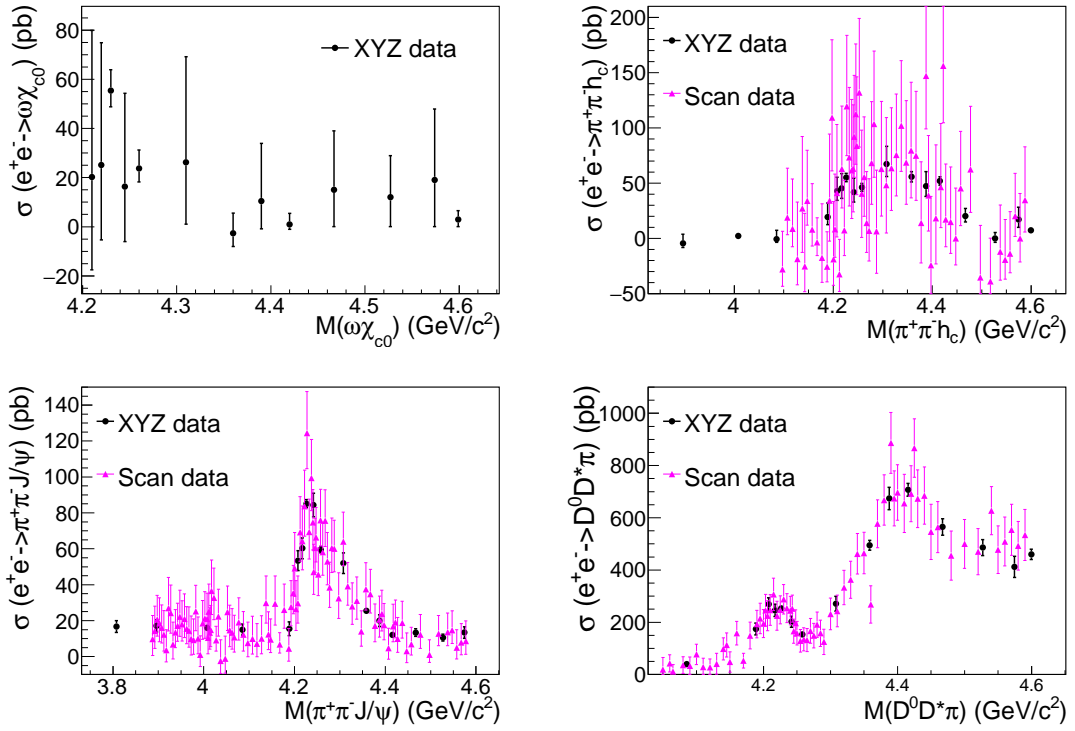


Figure 4.1: The measured cross sections of $e^+e^- \rightarrow \omega\chi_{c0}$, $\pi^+\pi^-\text{h}_c$, $\pi^+\pi^-\text{J}/\psi$, and $\text{D}^0\text{D}^*\pi + \text{c.c.}$ by the BESIII experiment. The dots are from the XYZ data sample and the triangles are from the R -scan data sample. The error bars are the sum in quadrature of the statistical and uncommon systematic errors. Here, for each process the common systematic errors are not shown.

4.2 Motivation

There is a common structure at around 4.22 GeV, called Y(4220) found among those four channels, $e^+e^- \rightarrow \pi^+\pi^-h_c$, $e^+e^- \rightarrow \omega\chi_{c0}$, $e^+e^- \rightarrow \pi^+\pi^-J/\psi$ and $e^+e^- \rightarrow D^0D^{*-}\pi^+ + c.c.$. As such a state is still not observed in other open charm final states [176], these four final states are probably the dominant decay modes of the Y(4220). We may obtain the best knowledge on the Y(4220), such as mass, width, coupling to lepton, and decay branching fractions, by applying constraints to the resonant parameters in a simultaneous fit to the cross sections of these four processes. In addition, we may have a better understanding of its nature [90], especially whether it is an exotic state, such as a tetraquark state in the diquark-antidiquark model [177], a vector molecular state of $D\bar{D}_1(2420)$ [178], a mixture of two hadrocharmonium states [179], an $\omega\chi_{cJ}$ molecule [180, 181], or a charmonium-hybrid state [182].

4.3 The data and the fit formalism

We use the measured cross section of $e^+e^- \rightarrow \pi^+\pi^-h_c$, $e^+e^- \rightarrow \omega\chi_{c0}$, $e^+e^- \rightarrow \pi^+\pi^-J/\psi$ and $e^+e^- \rightarrow D^0D^{*-}\pi^+ + c.c.$ processes by BESIII experiment [172, 171, 173, 174] only for the simultaneous fit. The data are shown in figure 4.1, where the dots with error bars are from the XYZ data sample and the triangles with error bars are from the R-scan data sample. The error bars are the sum in quadrature of the statistical and uncommon systematic uncertainties, the systematic uncertainties common to the energy points in each process are removed since they have no effect on the fitted resonant parameters.

We assume that the cross section could be parametrized with the coherent sum of a few amplitudes, either resonance represented by a Breit-Wigner (BW) function or non-resonant background term represented by a phase space term. The BW function used in this fit is

$$\text{BW}(\sqrt{s}) = \frac{\sqrt{12\pi\Gamma_{e^+e^-}\mathcal{B}_f\Gamma}}{s - M^2 + iM\Gamma} \sqrt{\frac{\text{PS}_n(\sqrt{s})}{\text{PS}_n(M)}},$$

where M is the mass of the resonance; Γ and $\Gamma_{e^+e^-}$ are the total width and partial width to e^+e^- , respectively; \mathcal{B}_f is the branching fraction of the resonance decays into final state f ; and PS_n is the n -body decay phase space factor.

We also assume that in the data shown in figure 4.1, the observed structures at around 4.22 GeV in all four processes and structures at around 4.39 GeV in $e^+e^- \rightarrow \pi^+\pi^-h_c$ and $D^0D^{*-}\pi^+ + c.c.$ are due to the same resonant states, that is,

$$\sigma_{\omega\chi_{c0}}(\sqrt{s}) = |\text{BW}_1(\sqrt{s})|^2, \quad (4.1)$$

$$\sigma_{\pi^+\pi^-h_c}(\sqrt{s}) = |\text{BW}_1(\sqrt{s}) + \text{BW}_3(\sqrt{s}) \cdot e^{i\phi_1}|^2, \quad (4.2)$$

$$\sigma_{\pi^+\pi^-J/\psi}(\sqrt{s}) = |\text{BW}_0(\sqrt{s}) + \text{BW}_1(\sqrt{s}) \cdot e^{i\phi_2} + \text{BW}_2(\sqrt{s}) \cdot e^{i\phi_3}|^2, \quad (4.3)$$

$$\sigma_{D^0D^{*-}\pi^++c.c.}(\sqrt{s}) = |\sqrt{\text{PS}_3(\sqrt{s})} + \text{BW}_1(\sqrt{s}) \cdot e^{i\phi_4} + \text{BW}_3(\sqrt{s}) \cdot e^{i\phi_5}|^2, \quad (4.4)$$

where BW_0 , BW_1 , BW_2 and BW_3 represent the $Y(4008)$, $Y(4220)$, $Y(4320)$ and $Y(4390)$, respectively, and ϕ is the relative phase between the amplitudes.

By using the MINUIT packages in the CERN Program Library [183], we perform a combined fit using a least squares method, where the χ^2 function is constructed as

$$\chi^2 = \sum_{j=1}^4 \sum_{i=1}^n \frac{(\sigma_{ij}^{data} - \sigma_{ij}^{fit})^2}{\delta_{ij}^2},$$

where σ_{ij}^{data} and σ_{ij}^{fit} are the measured and fitted cross sections of the i th energy point in the j th mode, δ_{ij} is the corresponding total uncertainty with common systematic uncertainties removed. The sum is performed over all the measured cross section points from the above mentioned four modes. The χ^2 is minimized to obtain the best estimation of the resonant parameters.

4.4 Fit results

We do the fit using BESIII data on the cross sections of the four processes, $e^+e^- \rightarrow \pi^+\pi^-h_c$, $e^+e^- \rightarrow \omega\chi_{c0}$, $e^+e^- \rightarrow \pi^+\pi^-J/\psi$ and $e^+e^- \rightarrow D^0D^{*-}\pi^+ + c.c$ simultaneously. Because of the amplitude interference between the resonances, there are one solutions, two solutions, four solutions, and four solutions with the same minimum values of χ^2 for $e^+e^- \rightarrow \omega\chi_{c0}$, $e^+e^- \rightarrow \pi^+\pi^-h_c$, $e^+e^- \rightarrow \pi^+\pi^-J/\psi$ and $e^+e^- \rightarrow D^0D^{*-}\pi^+ + c.c$, respectively. Among the solutions, the masses and the widths of the resonances are identical but the partial widths to e^+e^- and relative phases are different for each process.

The fit results with a goodness-of-fit of $\chi^2/ndf = 241/273 = 0.9$ are obtained from the simultaneous fit and showed in figure 4.2, where the solid curves show the projections from the best fit, the dashed curves show the fitted resonance components from different solutions. In Table 4.1, the corresponding mass, width, and the product of the branching fraction to specific mode and the e^+e^- partial width for each resonance are listed.

From the fit we obtain $M = (4219.6 \pm 3.3)$ MeV and $\Gamma = (56.0 \pm 3.6)$ MeV for the state $Y(4220)$, with only statistical uncertainties.

4. STUDY EXOTIC STATE $Y(4220)$ WITH BESIII DATA

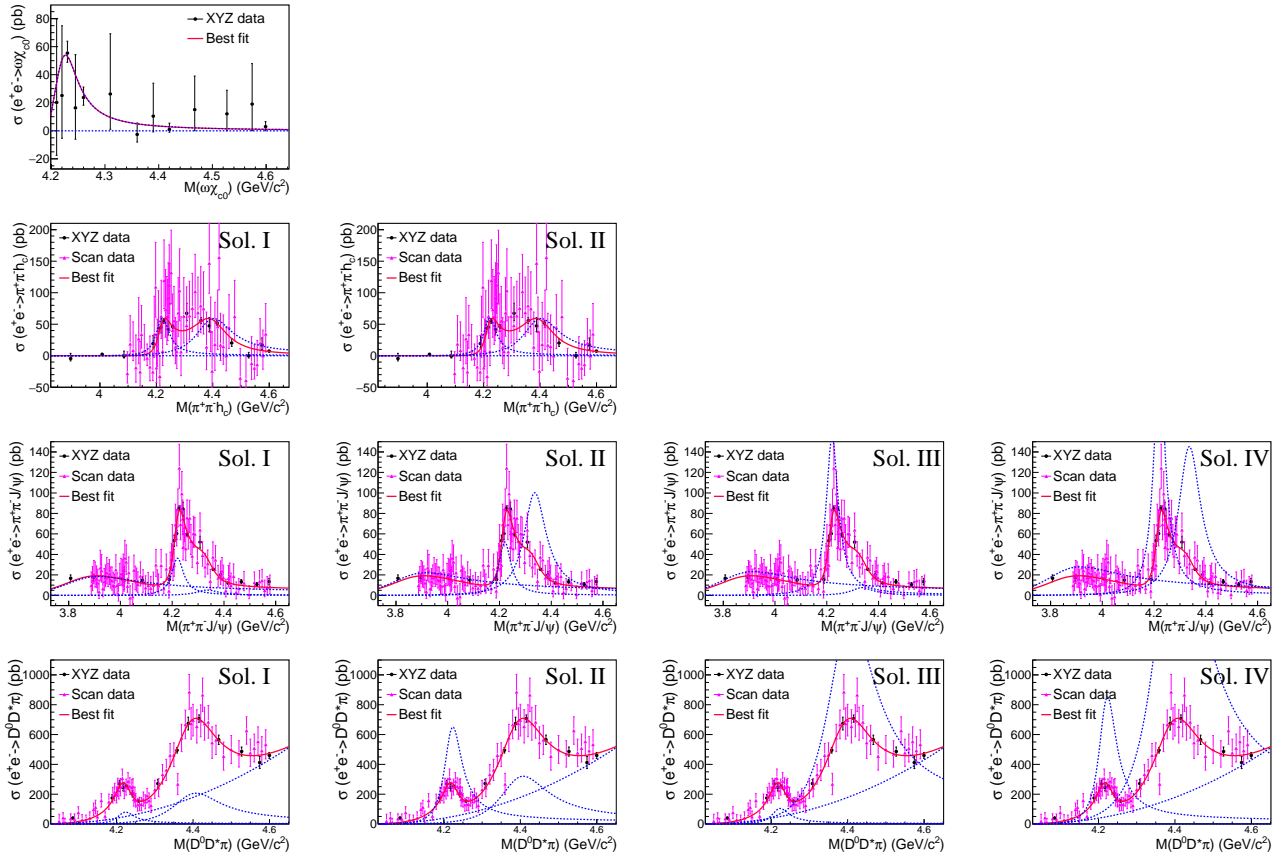


Figure 4.2: The results of the combined fit to $e^+e^- \rightarrow \omega\chi_{c0}$, $\pi^+\pi^-h_c$, $\pi^+\pi^-J/\psi$, and $D^0D^{*-}\pi^+ + c.c.$ (from the top to the bottom row). The dots and the triangles with errors bars are data as described in Fig. 4.1 caption. The solid curves are the projections from the best fit. The dashed curves show the fitted resonance components from different solutions indicated in the top right corner in each plot. The numerical results of all the solutions are presented in Table 4.1.

	Y(4008)	Y(4220)	Y(4320)	Y(4390)
M	3846.3 ± 45.5	4219.6 ± 3.3	4333.2 ± 19.9	4391.5 ± 6.3
Γ	345.6 ± 58.2	56.0 ± 3.6	104.3 ± 44.9	153.2 ± 11.4

	Solution I	Solution II	Solution III	Solution IV
$(\mathcal{B}_{\omega\chi_{c0}} \times \Gamma_{e^+e^-})_{Y(4220)}$	3.4 ± 0.4			
$(\mathcal{B}_{\pi^+\pi^-h_c} \times \Gamma_{e^+e^-})_{Y(4220)}$	4.0 ± 1.1	4.0 ± 1.1		
$(\mathcal{B}_{\pi^+\pi^-h_c} \times \Gamma_{e^+e^-})_{Y(4390)}$	11.7 ± 2.4	11.7 ± 2.5		
ϕ_1	3.1 ± 0.4	-3.2 ± 0.4		
$(\mathcal{B}_{\pi^+\pi^-J/\psi} \times \Gamma_{e^+e^-})_{Y(4008)}$	5.5 ± 0.3	6.6 ± 0.7	6.9 ± 0.7	8.3 ± 0.7
$(\mathcal{B}_{\pi^+\pi^-J/\psi} \times \Gamma_{e^+e^-})_{Y(4220)}$	2.5 ± 0.2	3.5 ± 0.7	10.5 ± 1.1	15.1 ± 1.3
ϕ_2	0.1 ± 0.1	0.8 ± 0.3	-1.8 ± 0.2	-1.0 ± 0.1
$(\mathcal{B}_{\pi^+\pi^-J/\psi} \times \Gamma_{e^+e^-})_{Y(4320)}$	0.7 ± 0.2	13.3 ± 3.8	1.0 ± 0.5	19.4 ± 3.2
ϕ_3	2.2 ± 0.2	-2.0 ± 0.2	1.4 ± 0.6	-2.7 ± 0.1
$(\mathcal{B}_{D^0D^{*-}\pi^++c.c.} \times \Gamma_{e^+e^-})_{Y(4220)}$	5.3 ± 0.6	43.3 ± 3.2	6.9 ± 0.8	56.7 ± 4.2
ϕ_4	2.2 ± 0.1	-2.2 ± 0.1	-2.7 ± 0.1	-0.8 ± 0.1
$(\mathcal{B}_{D^0D^{*-}\pi^++c.c.} \times \Gamma_{e^+e^-})_{Y(4390)}$	39.7 ± 4.3	61.6 ± 6.6	265.5 ± 16.6	412.0 ± 26.0
ϕ_5	1.9 ± 0.1	1.5 ± 0.2	4.7 ± 0.1	4.2 ± 0.1

Table 4.1: The resonant parameters from the combined fit to $e^+e^- \rightarrow \omega\chi_{c0}$, $\pi^+\pi^-h_c$, $\pi^+\pi^-J/\psi$, and $D^0D^{*-}\pi^++c.c.$. Here M , Γ , and $(\mathcal{B}_i \times \Gamma_{e^+e^-})_j$ are the mass (in MeV), total width (in MeV), and the product of the branching fraction to specific final state and the e^+e^- partial width (in eV), respectively, where i presents a final state and j indicates a resonance added in the fit in different processes. The fitted mass and width for each resonance are shown in the upper table separately. All the errors are statistical from fit only. ϕ is the relative phase (in rad).

4.5 Systematic uncertainties

The systematic uncertainties in the resonant parameters from the simultaneous fit to the cross sections of the above four processes are mainly due to the absolute c.m. energy measurement, the c.m. energy spread, parametrization of the resonances, background shape, and the cross section measurements.

The systematic uncertainties from the absolute c.m. energy measurement, the c.m. energy spread and the cross section measurements on the resonant parameters can be taken from the original BESIII publications directly [172, 171, 173, 174].

The uncertainty from the cross section measurement in each process is common for all data points, which only affects the $\mathcal{B} \times \Gamma_{e^+e^-}$ measurement and is 13.3%, 14.8%, 5.8%, and 4.6% for $\omega\chi_{c0}$, $\pi^+\pi^-\text{h}_c$, $\pi^+\pi^-J/\psi$, and $D^0D^{*-}\pi^+ + \text{c.c.}$, respectively.

For the systematic uncertainty from the resonances parametrization, we assume a mass dependent width instead of using a constant total width to estimate the signal parametrization uncertainty. We use an exponential function as used in Ref. [173] to model the $\pi^+\pi^-J/\psi$ cross section near 4 GeV, instead of using the Y(4008) resonance. We also consider the systematic bias introduced by possible additional resonances in the processes under study. The fit scenarios include adding an additional phase space term for $\omega\chi_{c0}$; using three resonances, the Y(4220), Y(4320) and Y(4390), to fit $\pi^+\pi^-\text{h}_c$, $D^0D^{*-}\pi^+ + \text{c.c.}$, or both of them. The shifts of the masses and widths are taken as systematic uncertainties.

The overall systematic uncertainties are obtained by adding all the sources of systematic uncertainties in quadrature assuming they are independent, which are 16.7 MeV and 31.6 MeV for the mass and width of the Y(4008), respectively; 5.1 MeV and 6.9 MeV for the mass and width of the Y(4220), respectively; 20.9 MeV and 23.1 MeV for the mass and width of the Y(4320), respectively; and 20.8 MeV and 16.4 MeV for the mass and width of the Y(4390), respectively.

4.6 Chapter summary and discussion

From a combined fit to the cross sections of $e^+e^- \rightarrow \omega\chi_{c0}$, $e^+e^- \rightarrow \pi^+\pi^-\text{h}_c$, $e^+e^- \rightarrow \pi^+\pi^-J/\psi$ and $e^+e^- \rightarrow D^0D^{*-}\pi^+ + \text{c.c.}$ that are measured by BESIII, we determine the mass of the Y(4220) as $(4219.6 \pm 3.3 \pm 5.1)$ MeV and the width of $(56.0 \pm 3.6 \pm 6.9)$ MeV, and the relative production rates in these four decay modes.

The leptonic decay width for a vector state is an important quantity, that can help to discriminate various theoretical interpretations for the nature of it. The magnitude of the leptonic decay width determines how the strong decay widths sum up to the total width. Smaller leptonic decay width means that the strong decay widths will be relatively enhanced and vice versa. As the Y(4220) is the dominant component in $e^+e^- \rightarrow \pi^+\pi^-J/\psi$, we assume the theoretical interpretations on the Y(4260) apply for the Y(4220).

The recent estimation of Lattice QCD for the Leptonic decay width of the $Y(4220)$ is about 40 eV [184] as a feature of the hybrid scenario; the predicted upper limit of the $Y(4220)$ leptonic decay width is about 500 eV if the $Y(4220)$ is a hadronic molecule dominated by $DD_1(2420)$ [185]; while the leptonic decay width is only about 23 eV for the $\omega\chi_{c0}$ molecule interpretation [186] with no contributions from the open charm decay channel are included in the analysis.

By considering the isospin symmetric modes of the measured channels, we can estimate the lower limit on the leptonic partial width of the $Y(4220)$ decays. For an isospin-zero charmonium-like state [184], we expect

$$\begin{aligned}\mathcal{B}_{\pi\pi h_c} &= \frac{3}{2} \times \mathcal{B}_{\pi^+\pi^- h_c}, \\ \mathcal{B}_{\pi\pi J/\psi} &= \frac{3}{2} \times \mathcal{B}_{\pi^+\pi^- J/\psi}, \\ \mathcal{B}_{D\bar{D}^*\pi} &= 3 \times \mathcal{B}_{D^0 D^{*-} \pi^+ + c.c.}.\end{aligned}$$

So we have

$$\begin{aligned}\Gamma_{e^+e^-} &= \sum_i \mathcal{B}_i \times \Gamma_{e^+e^-} \\ &= \mathcal{B}_{\omega\chi_{c0}} \times \Gamma_{e^+e^-} + \mathcal{B}_{\pi\pi h_c} \times \Gamma_{e^+e^-} + \mathcal{B}_{\pi\pi J/\psi} \times \Gamma_{e^+e^-} + \mathcal{B}_{D\bar{D}^*\pi} \times \Gamma_{e^+e^-} + \dots\end{aligned}$$

By plugging in the numbers in Table 4.1, and only taking the Solutions with the smallest $\mathcal{B} \times \Gamma_{e^+e^-}$, we obtain

$$\begin{aligned}\Gamma_{e^+e^-} &= (3.4 \pm 0.4 \pm 1.8) + \frac{3}{2} \times (4.0 \pm 1.1 \pm 3.2) + \frac{3}{2} \times (2.5 \pm 0.2 \pm 0.8) \\ &\quad + 3 \times (5.3 \pm 0.6 \pm 1.5) + \dots \\ &= (29.1 \pm 2.5 \pm 7.0) + \dots \text{ eV} \\ &> (29.1 \pm 2.5 \pm 7.0) \text{ eV},\end{aligned}$$

where the first errors are from fit and the second are the systematic errors. The lowest value of the $\Gamma_{e^+e^-}$ of the $Y(4220)$ is around 30 eV. This lower limit on the leptonic partial width of the $Y(4220)$ is close to the prediction from Lattice-QCD for a hybrid vector charmonium state.

On the other hand, if we take the Solutions with the largest $\mathcal{B} \times \Gamma_{e^+e^-}$ in Table 4.1, we can obtain $\Gamma_{e^+e^-} = (202 \pm 13 \pm 23) + \dots$ eV. The other combinations of the Solutions result in $\Gamma_{e^+e^-}$ values between $(30+\dots)$ and $(200+\dots)$ eV. This means that the leptonic partial width of the $Y(4220)$ can be as large as 200 eV or even higher based on current information, to be compared with the predicted upper limit of 500 eV from the molecular scenario [185].

If we assume these modes saturate the $Y(4220)$ decays, we determine the $Y(4220)$ decay branching fractions to the above four modes. For the most interesting mode, $Y(4220) \rightarrow \pi\pi J/\psi$, if we consider the case of smallest $\mathcal{B} \times \Gamma_{e^+e^-}$, we obtain $\mathcal{B}_{\pi\pi J/\psi} = (12.9 \pm 1.3 \pm 3.9)\%$ (or a partial width of $(7.2 \pm 0.8 \pm 2.2)$ MeV); and if consider the case of highest $\mathcal{B} \times \Gamma_{e^+e^-}$, we obtain $\mathcal{B}_{\pi\pi J/\psi} = (11.2 \pm 1.1 \pm 1.9)\%$ (or a partial width of $(6.3 \pm 0.7 \pm 1.1)$ MeV). In these two particular cases, the branching fraction of

4. STUDY EXOTIC STATE $Y(4220)$ WITH BESIII DATA

the $Y(4220) \rightarrow \pi\pi J/\psi$ is very big. We may also calculate the $\mathcal{B}_{\pi\pi J/\psi}$ in the most extreme case, i.e., taking the smallest $\mathcal{B} \times \Gamma_{e^+e^-}$ for $\pi\pi J/\psi$ and largest $\mathcal{B} \times \Gamma_{e^+e^-}$ for the other modes, we find $\mathcal{B}_{\pi\pi J/\psi} = (2.1 \pm 0.3 \pm 0.7)\%$ (or a partial width of $(1.2 \pm 0.2 \pm 0.4)$ MeV).

However, the assumption that the $\omega\chi_{c0}$, $\pi^+\pi^-h_c$, $\pi^+\pi^-J/\psi$, and $D^0D^{*-}\pi^+ + \text{c.c.}$ modes saturate the $Y(4220)$ decays may not be true. Being well above the thresholds of many final states with η_c , such as $\pi\rho\eta_c$, $\omega\eta_c$, and $\phi\eta_c$, and final states like ηh_c , $\pi\pi\psi(2S)$, and $K\bar{K}J/\psi$, $Y(4220)$ may decay into such final states with substantial rates. In addition, the decays into open charm final states other than $D\bar{D}^*\pi$ such as $D\bar{D}$, $D\bar{D}^* + \text{c.c.}$, D^*D^* , $D_s^+D_s^-$, $D_s^+D_s^{*-} + \text{c.c.}$ are also possible, although the charmed mesons are in relative P-wave. The $Y(4220)$ is very close to the $D_s^{*+}D_s^{*-}$ threshold, the possible coupling to this model should also be investigated.

Further information on these final states will be important for a deeper understanding of the nature of the $Y(4220)$.

The analysis described in this Chapter has been published:

“Resonant parameters of the $Y(4220)$ ”

Gao X.Y, Shen C.P, Yuan, C.Z

PHYSICAL REVIEW D, Vol: 95, Num: 9, 2017

Chapter 5

Conclusion

Although the last standard model predicted particle, the Higgs scalar boson, has been observed in LHC, there are still some important questions on the basic forces and matter that drive physicists to search for physics beyond the standard model. Some of those BSM theories predict signatures observable in current large-scale scientific facilities. Considering the properties of particle and detectors, the lepton final states are much cleaner and clear than the other final states with hadrons, there are thus many theoretical predictions and experimental searches on lepton channels.

One of those favored predictions would be the lepton flavor violation process, since there is no relevant symmetry for the lepton flavor conservation. Various models give predictions of signature in $e\mu$ final states, such as supersymmetry R-parity violation model, quantum black hole model and GUT Z' boson model. The Chapter 2 details the search for lepton flavor violation processes in $e\mu$ final states with an integrated luminosity of 35.9 fb^{-1} collected in 2016 by the CMS. Good agreement is observed between the data and the standard model expectation. Therefore upper limits on the cross section are calculated and lower limits on the mass of heavy resonance decaying to $e\mu$ are set to the corresponding models at 95% C.L. Lower mass limit on the τ sneutrinos in R-parity violating supersymmetric model is found to be 3.8 TeV (couplings $\lambda_{132} = \lambda_{231} = \lambda'_{311} = 0.1$). Lower mass limits on the quantum black holes model are found to be 3.6 (5.3, 5.5, 5.6) TeV with the 1 (4, 5, 6) large extra spatial dimensions. Lower mass limit on the Z' boson is found to be 4.4 TeV assuming a 10% branching fraction to the $e\mu$ channel. Comparing to previous results in CMS with 2.7 fb^{-1} at 13 TeV, which is found to be 1.0 TeV and 2.7 TeV for τ sneutrinos with couplings $\lambda_{132} = \lambda_{231} = \lambda'_{311} = 0.01$ and 0.1, and 2.5 to 4.5 TeV for QBH from $n = 1$ to 6, they are significant improvements.

Another kind of BSMs gives predictions to a high mass resonance in dilepton final states, coming from a heavy Z' boson predicted by sequential standard models and GUTs or a spin-2 graviton candidate predicted by Randall-Sundrum model. The Chapter 3 details a search for high mass resonances in ee final states with 2016 CMS data and a similar search updated with 2017 CMS data. No evidence is observed and the 95% C.L. mass lower limit is found to be 4.7 TeV (4.1 TeV) for the predicted Z'_{SSM} (Z'_ψ) boson.

5. CONCLUSION

The LHC has collected data in 2018 at $\sqrt{s} = 13$ TeV corresponding to the integrated luminosity of $\sim 50 fb^{-1}$ and is presently in a shut down phase up to spring 2021. Considering the limits improvement on 2016 + 2017 data comparing to which on only 2016 data of the ee analysis, if we consider the combination of full 2016, 2017, and 2018 data, there is a possibility to extend the lower mass limits up to higher values, which would be important references for such theoretical interpretations in the future years. In another hand, since the search for Z' in dilepton final has combined the decay channels ee and $\mu\mu$, we may consider combining the $e\mu$ channel with $e\tau$ and $\mu\tau$ channels. Although the τ is quite heavy that leads to many different properties compared to the e and μ , it would be a possible way to extend the lower mass limits significantly with increased data size.

In another hand, the Standard Model gives a very loose law for the possible combinations of quarks, the quark model not only describes the mesons and baryons, but also permits the combinations such as tetraquarks, pentaquarks, and glueballs. In the past decade, many experiments report observations of resonances decaying into $c\bar{c} + X$ final states but out of any theoretical predictions, which are referred to be exotic XYZ states. One of the dominant limits on the study of those states in detail is from the statistical uncertainty due to the data size. If we consider some resonances observed in different decay modes come from the same state, we would be able to study that state with much larger data size. In the Chapter 4, we assume the resonant structure near 4.2 GeV in $e^+e^- \rightarrow \omega\chi_{c0}$, $\pi^+\pi^-h_c$, $\pi^+\pi^-J/\psi$, and $D^0D^{*-}\pi^+ + c.c.$ processes are from the same state Y(4220) and perform a combined fit to the cross sections measured by BESIII. We determine the mass of the Y(4220) as $(4219.6 \pm 3.3 \pm 5.1)$ MeV and the width as $(56.0 \pm 3.6 \pm 6.9)$ MeV, where the first uncertainties are statistical and the second ones systematic, and the relative production rates in these four decay modes.

Although there are a lot of XYZ states observed in various experiments up to now, the statistic is still the challenge against the study of the charmonium-like states. BESIII is planning to collect data at a higher center of mass energy of 4.6 GeV, which would extend the invariant mass spectra with more data points and help to constrain the shapes of cross sections. The initial state radiation is another important way to study the XYZ states, Belle II, the super B factory has already started to collect data at the energy of Υ production threshold, with the striking target data size of $50 ab^{-1}$ in 10 years. This data size would help to push the study of observed states and the search for new XYZ states up to higher precision. Therefore we could expect further study on these four final states and the further search in other more final states will provide more information for a deeper understanding of the nature of the Y(4220).

Chapter 6

Appendix

A Lepton kinematics

Here are the plots of the kinematic distributions for the events passed all selections in the $e\mu$ analysis in Chapter 2. The plots are split in terms of four categories according to the pseudorapidities of electron and muon.

- Barrel-Barrel (BB): $|\eta_e| < 1.4446$ and $|\eta_\mu| < 1.2$
- Barrel-Endcap (BE): $|\eta_e| < 1.4446$ and $1.2 \leq |\eta_\mu| < 2.4$
- Endcap-Barrel (EB): $1.566 < |\eta_e| < 2.5$ and $|\eta_\mu| < 1.2$
- Endcap-Endcap (EE): $1.566 < |\eta_e| < 2.5$ and $1.2 \leq |\eta_\mu| < 2.4$

The kinematic distributions of muon for different analysis categories (barrel-barrel, barrel-endcap, endcap-barrel, and endcap-endcap) are shown in figures 6.1 (6.2, 6.3, and 6.4) respectively.

The kinematic distributions of electron for different analysis categories (barrel-barrel, barrel-endcap, endcap-barrel, and endcap-endcap) are shown in figures 6.5 (6.6, 6.7, and 6.8) respectively.

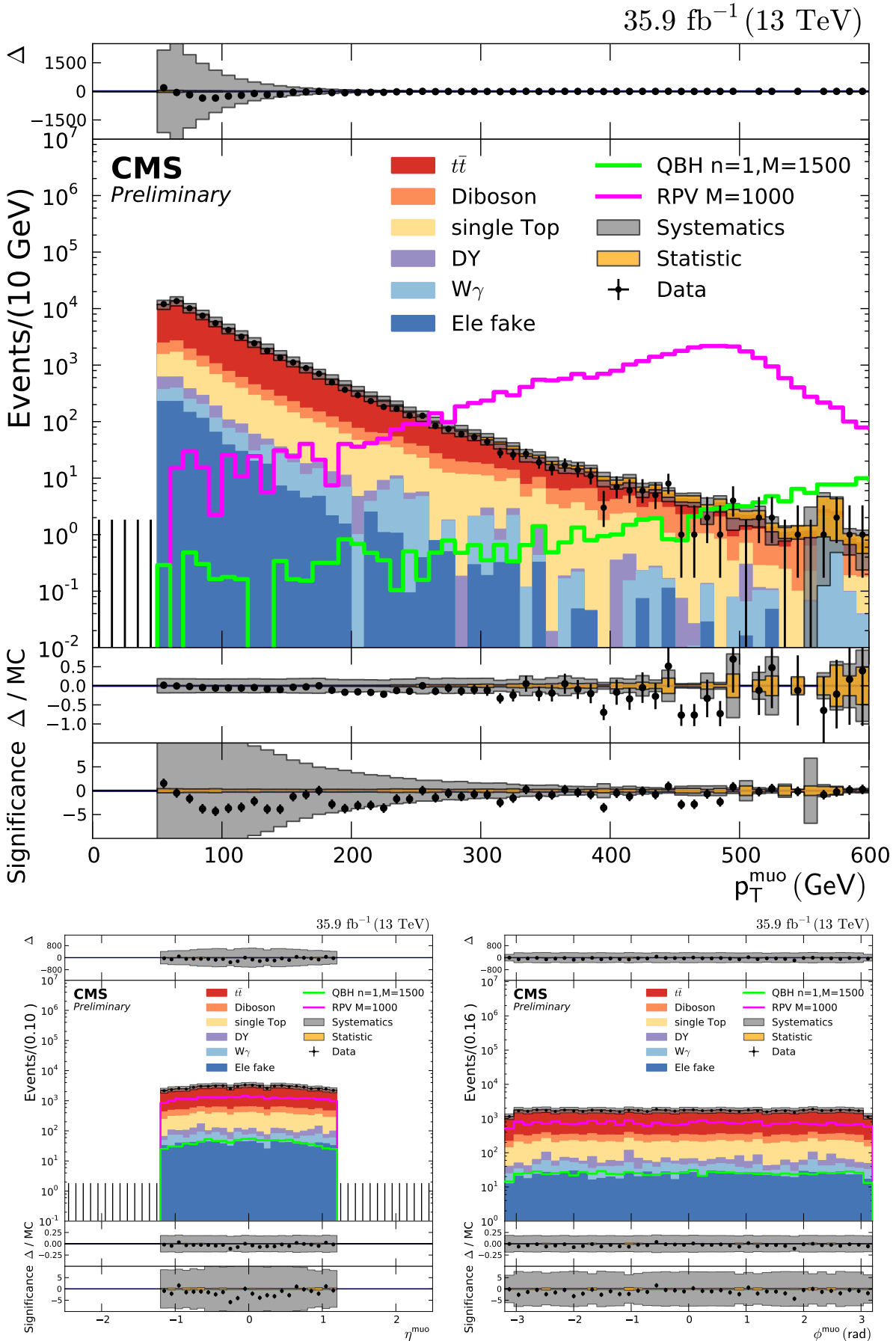


Figure 6.1: p_T (top), η (bottom left), and ϕ (bottom right) distributions of all selected muon candidates in barrel-barrel events. All shown events are required to pass the complete selection and contain therefore at least one electron and one muon.

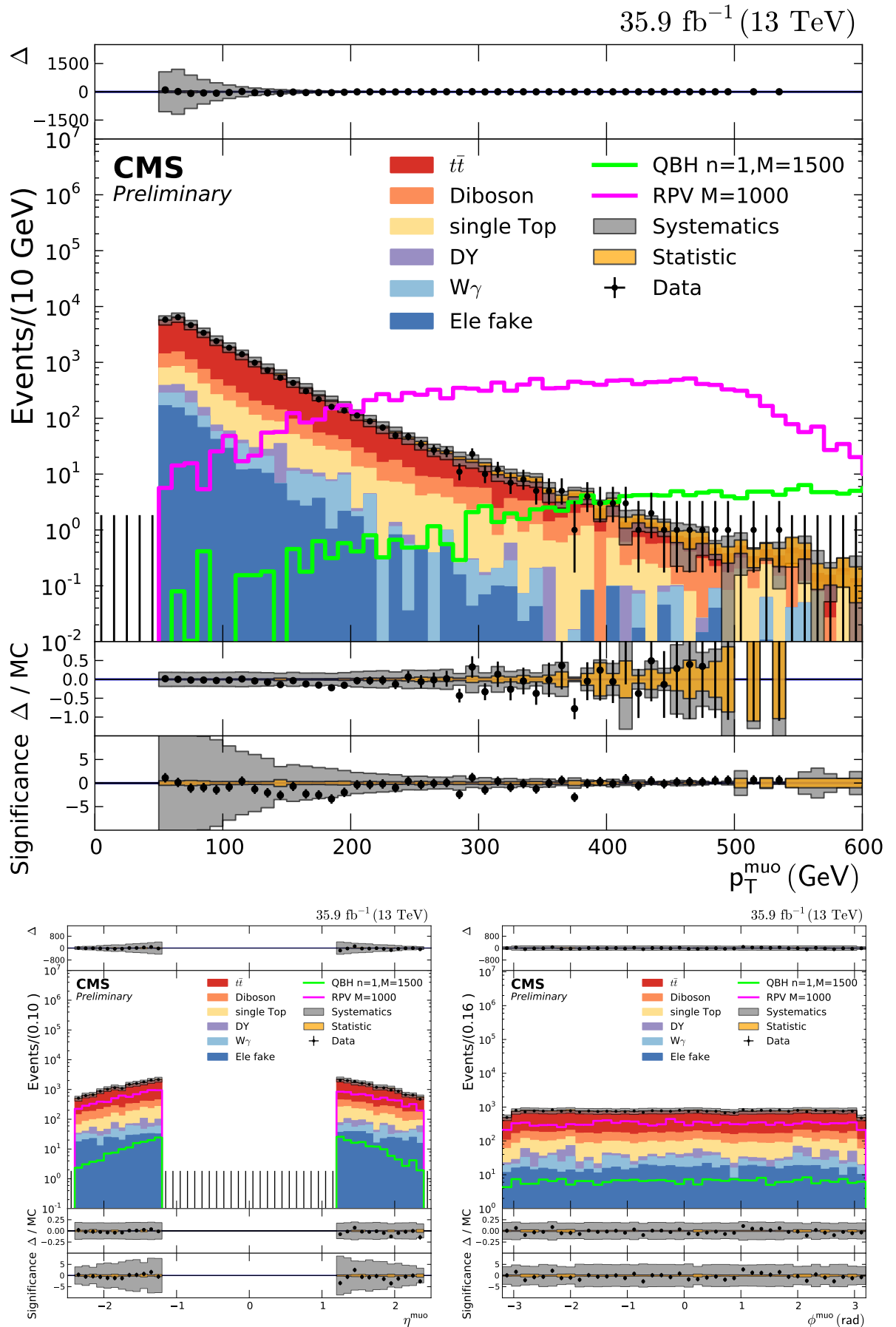


Figure 6.2: p_T (top), η (bottom left), and ϕ (bottom right) distributions of all selected muon candidates in barrel-endcap events. All shown events are required to pass the complete selection and contain therefore at least one electron and one muon.

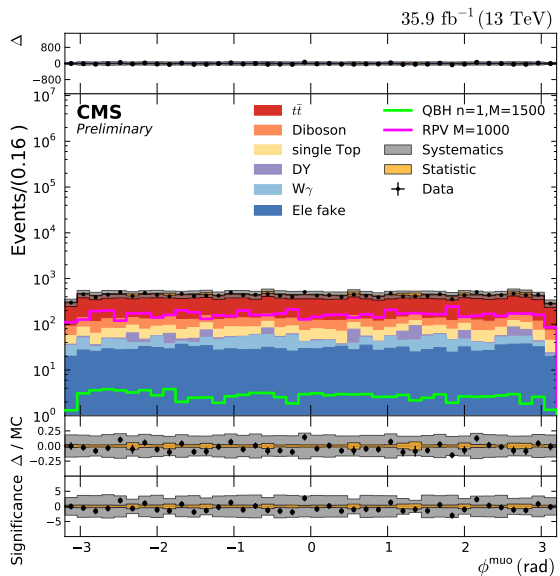
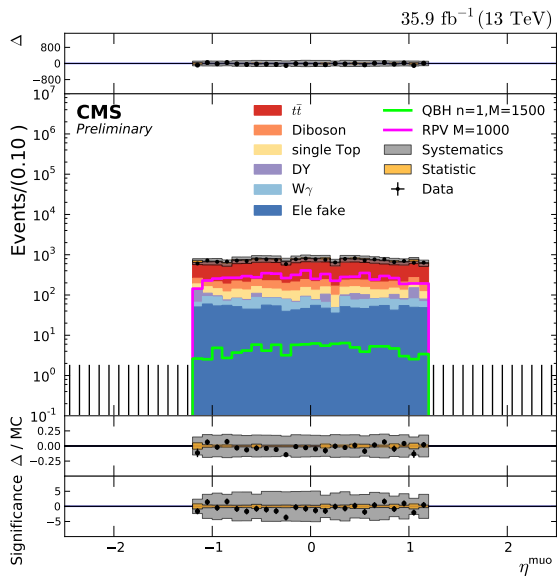
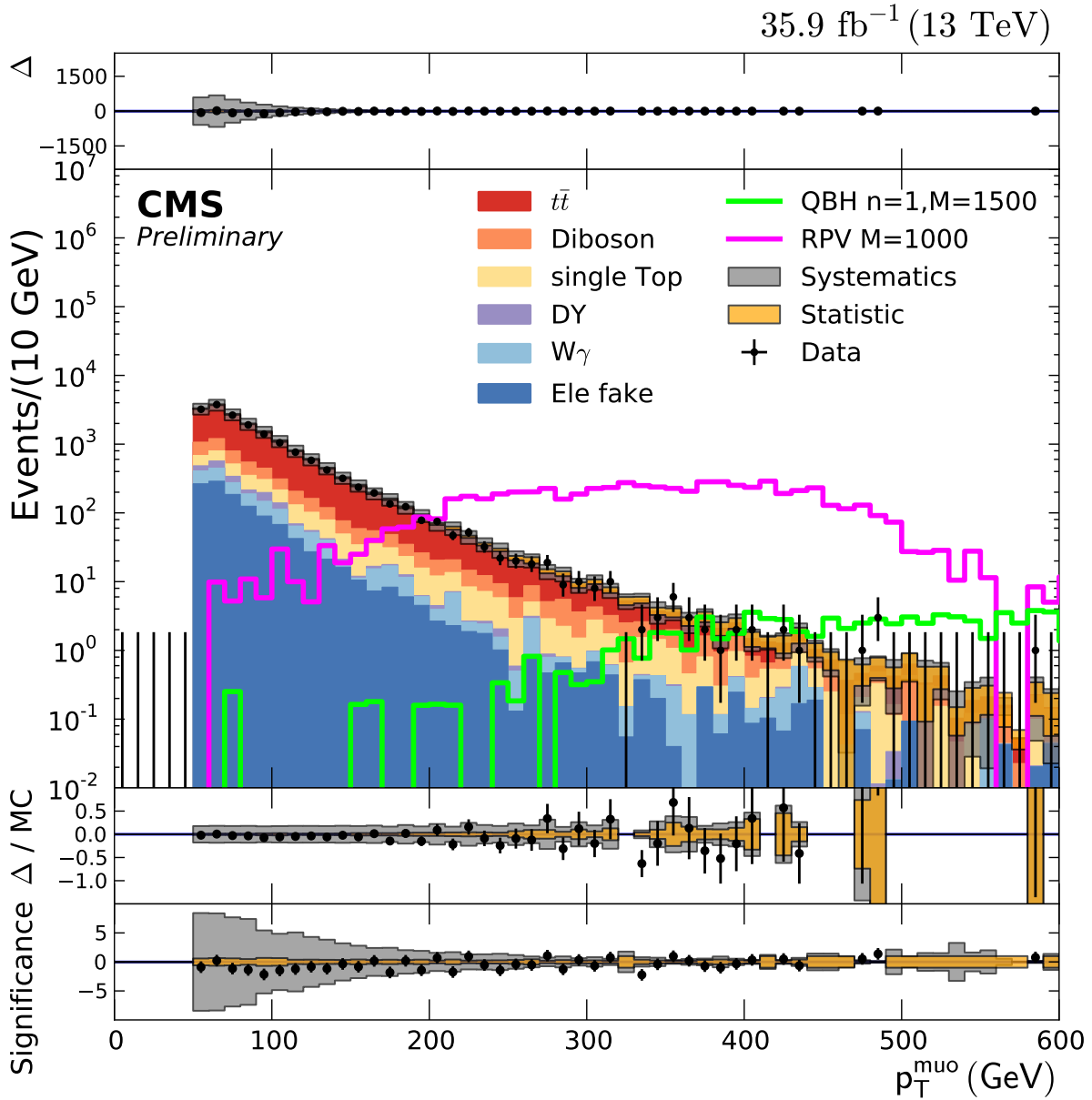


Figure 6.3: p_T (top), η (bottom left), and ϕ (bottom right) distributions of all selected muon candidates in endcap-barrel events. All shown events are required to pass the complete selection and contain therefore at least one electron and one muon.

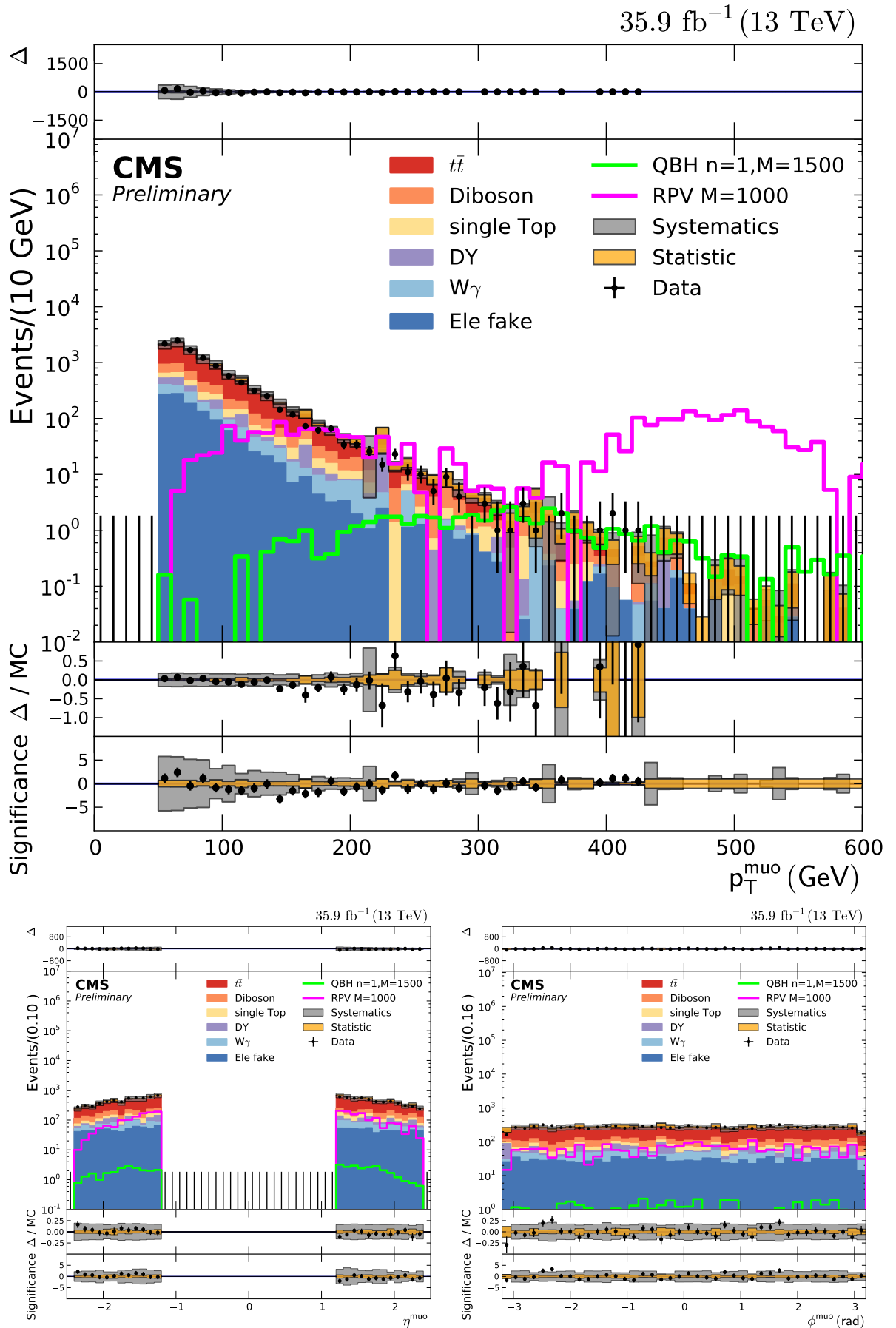


Figure 6.4: p_T (top), η (bottom left), and ϕ (bottom right) distributions of all selected muon candidates in endcap-endcap events. All shown events are required to pass the complete selection and contain therefore at least one electron and one muon.

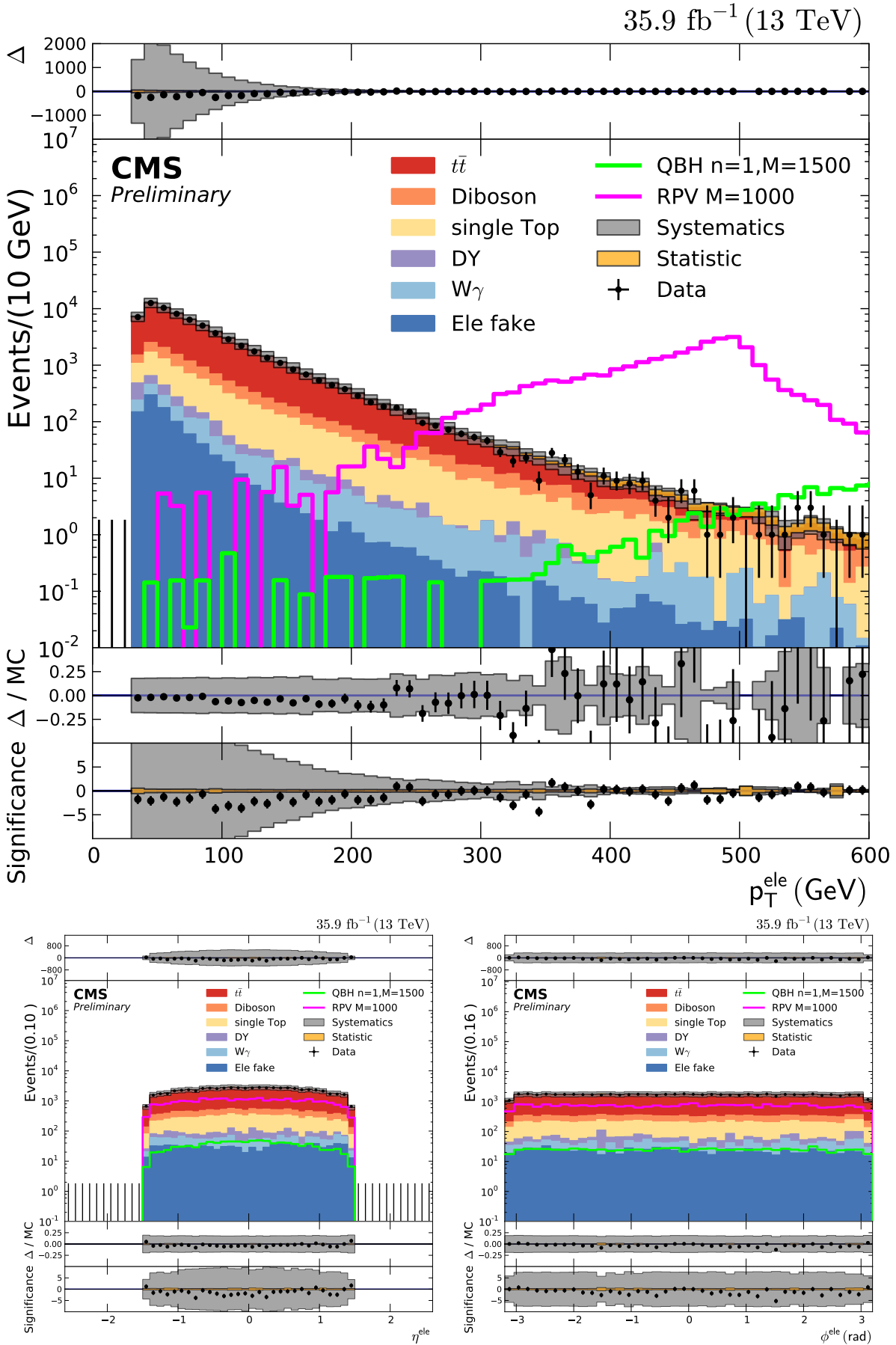


Figure 6.5: p_T (top), η (bottom left), and ϕ (bottom right) distributions of all selected electron candidates in barrel-barrel events. All shown events are required to pass the complete selection and contain therefore at least one electron and one muon.

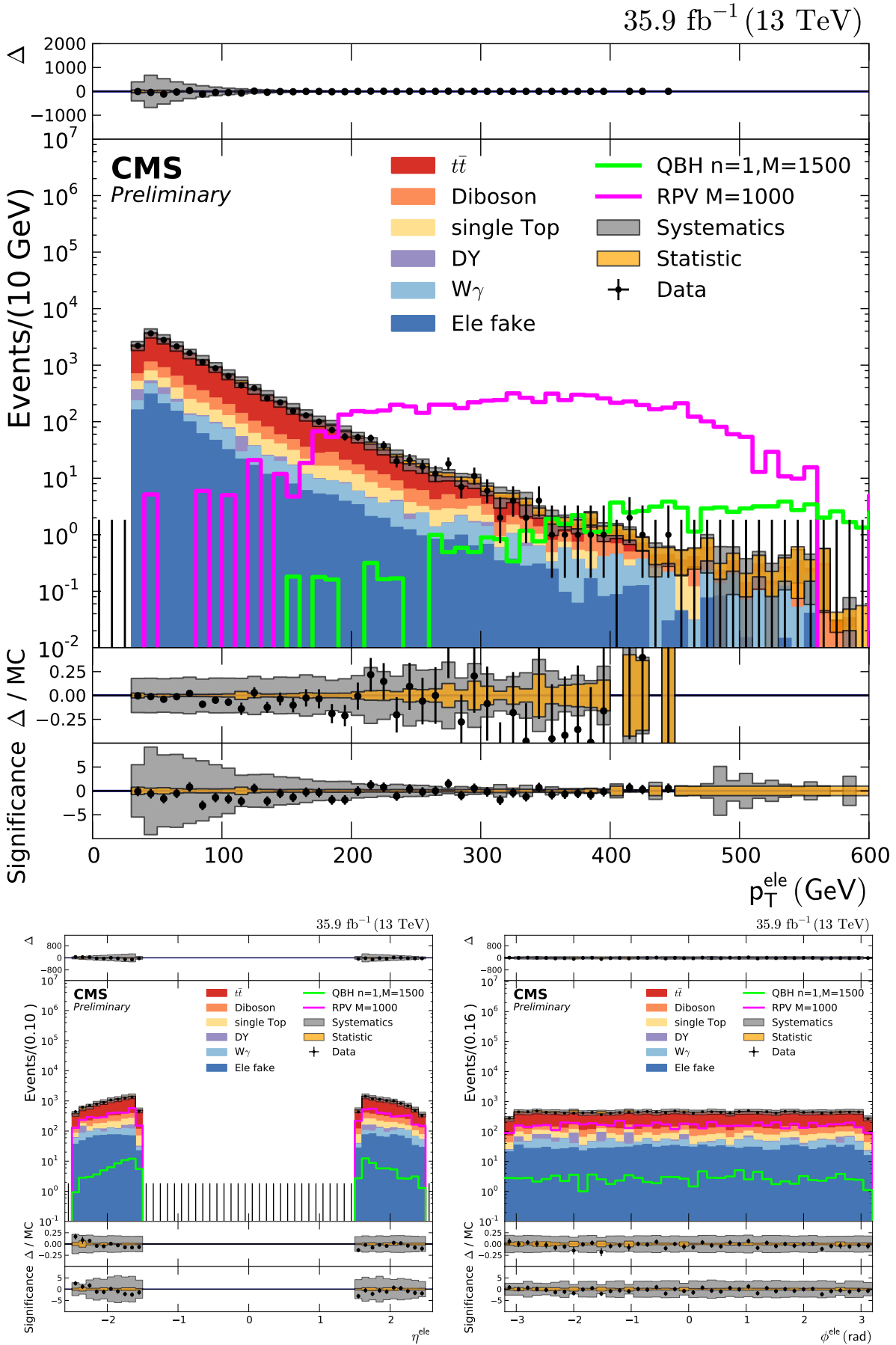


Figure 6.7: p_T (top), η (bottom left), and ϕ (bottom right) distributions of all selected electron candidates in endcap-barrel events. All shown events are required to pass the complete selection and contain therefore at least one electron and one muon.

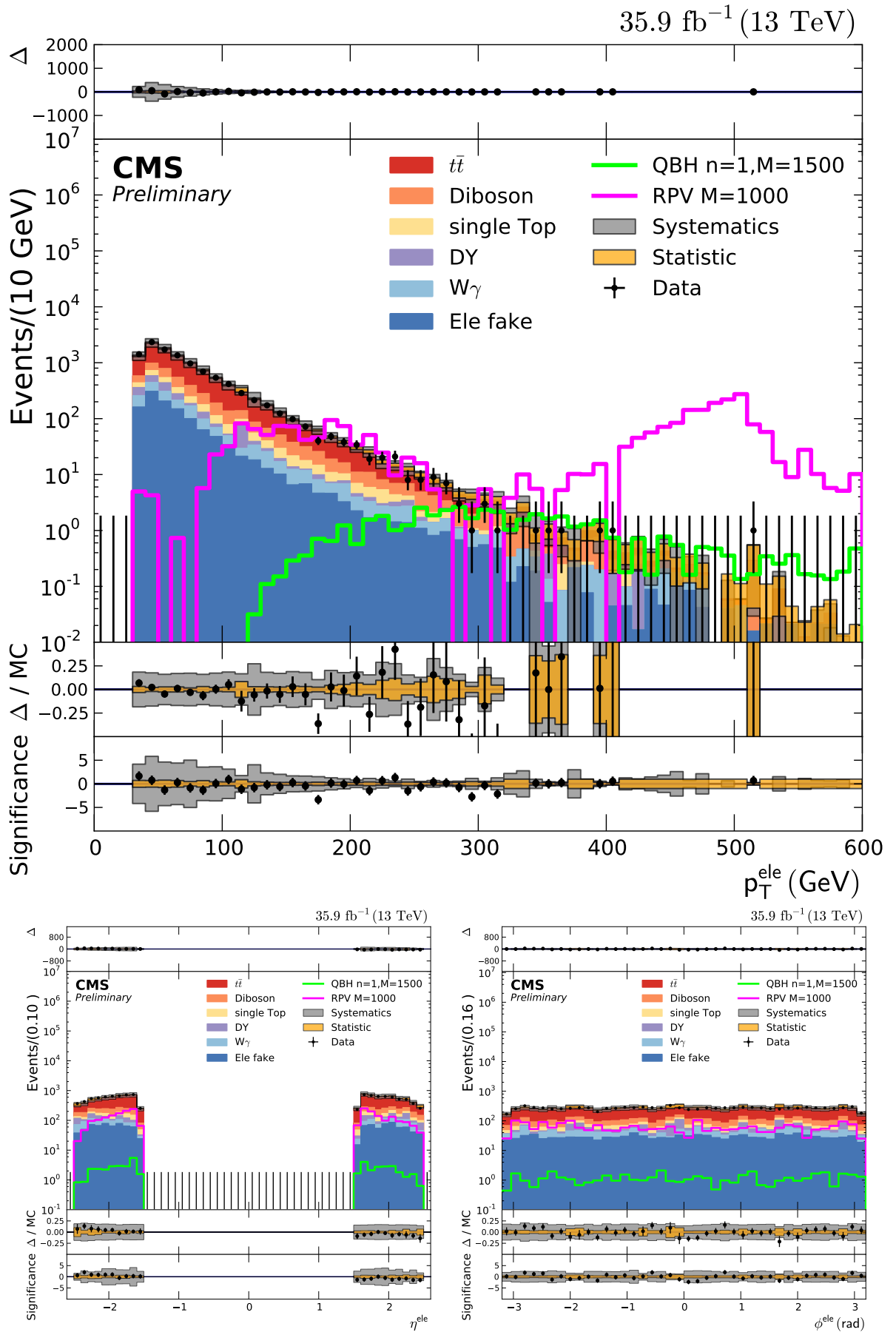


Figure 6.8: p_T (top), η (bottom left), and ϕ (bottom right) distributions of all selected electron candidates in endcap-endcap events. All shown events are required to pass the complete selection and contain therefore at least one electron and one muon.

B LFV signal invariant mass resolution

The mass resolution of the signal samples in Chapter 2 as function of gen-level $e\mu$ pair invariant mass in various categories are shown in figures 6.9. The values of the coefficients A, B, C, and D that are given in the plots are from the Crystal Ball function used to model the Gaussian shape of the signal distribution in the limit setting procedure.

The Crystal Ball function is defined as:

$$f(x; \alpha, n, \bar{x}, \sigma) = N \cdot \begin{cases} \exp\left(-\frac{(x-\bar{x})^2}{2\sigma^2}\right), & \text{for } \frac{x-\bar{x}}{\sigma} > -\alpha \\ A \cdot (B - \frac{x-\bar{x}}{\sigma})^{-n}, & \text{for } \frac{x-\bar{x}}{\sigma} \leq -\alpha \end{cases} \quad (6.1)$$

with input:

$$\begin{aligned} A &= \left(\frac{n}{|\alpha|}\right)^n \cdot \exp\left(-\frac{|\alpha|^2}{2}\right) \\ B &= \frac{n}{|\alpha|} - |\alpha| \\ N &= \frac{1}{\sigma(C+D)} \\ C &= \frac{n}{|\alpha|} \cdot \frac{1}{n-1} \cdot \exp\left(-\frac{|\alpha|^2}{2}\right) \\ D &= \sqrt{\frac{\pi}{2}} \left(1 + \operatorname{erf}\left(\frac{|\alpha|}{\sqrt{2}}\right)\right) \end{aligned}$$

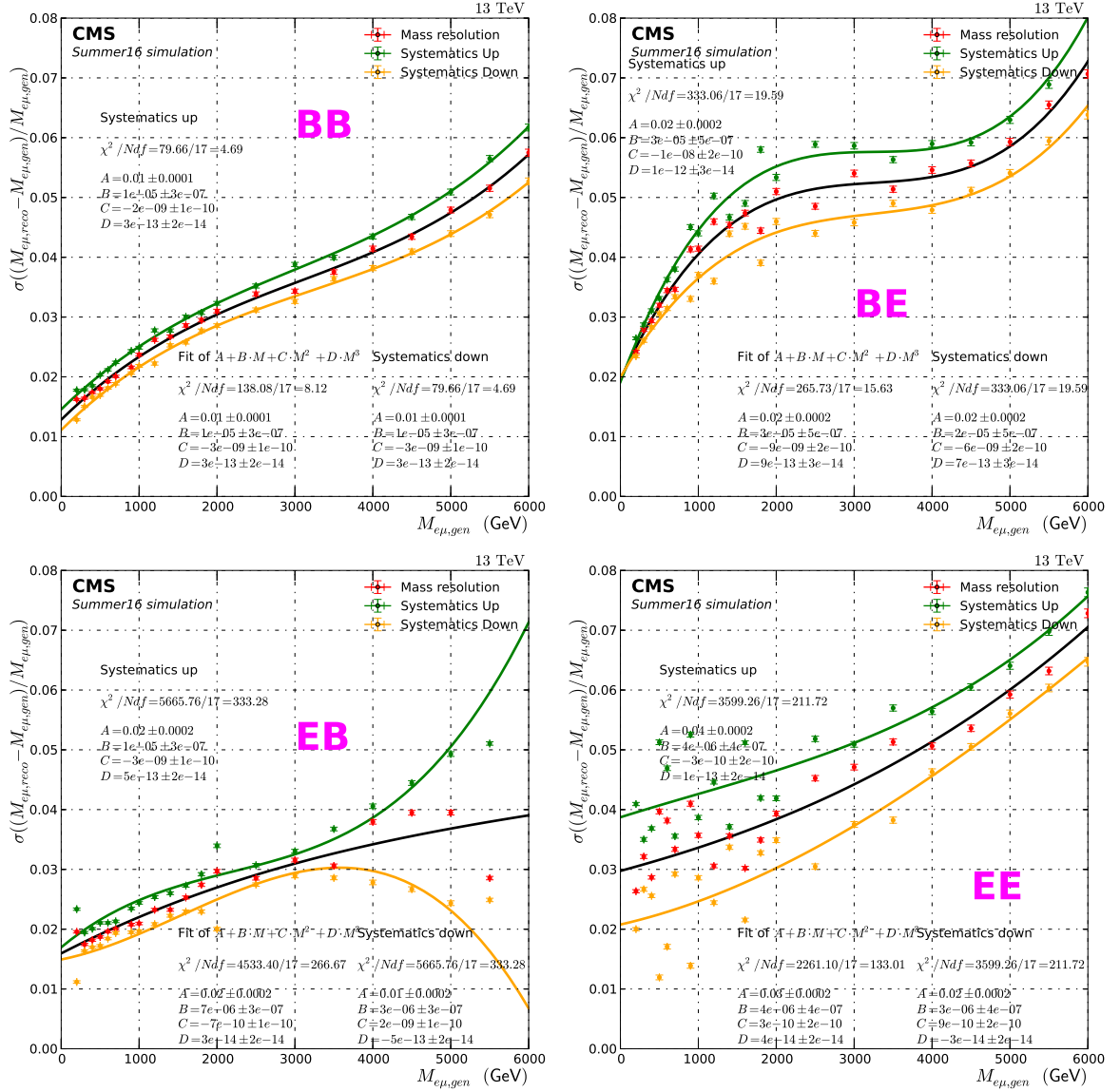


Figure 6.9: Relative invariant mass resolution for the different categories, top-left: barrel(μ)-barrel(e), top-right: barrel(μ)-endcap(e), bottom-left: endcap(μ)-barrel(e), bottom-right: endcap(μ)-endcap(e), of $e\mu$ pairs obtained from RPV signal simulation. The systematic uncertainties are derived by propagating the effect of the systematic uncertainties towards the mass resolution.

C HEEP ID efficiencies

The following figures 6.10, 6.11, 6.12 show the efficiencies of the HEEP ID selection described in the Table 2.1 in the Chapter 3. The efficiencies for data and MC are shown as functions of η , ϕ , and of the number of primary vertices (N_{vts}) respectively.

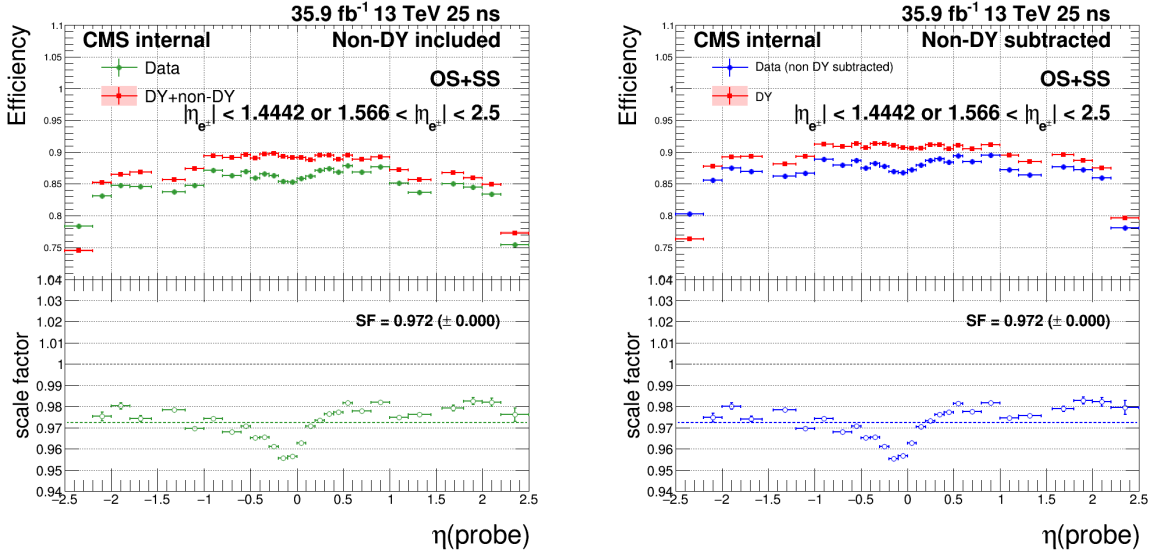


Figure 6.10: Efficiencies and scale factors in MC and data where the non-DY processes are included (left) and subtracted (right) as functions of probe η .

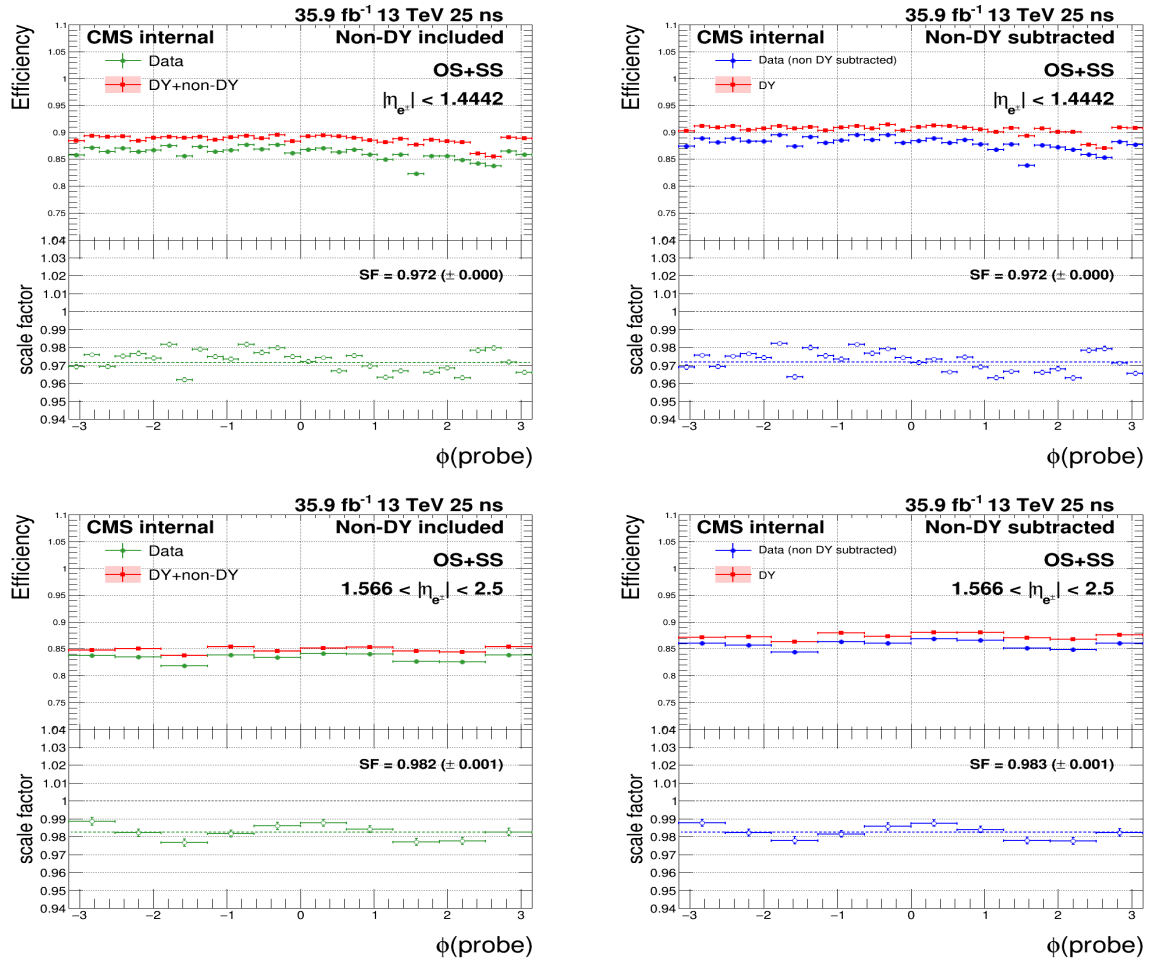


Figure 6.11: Efficiencies and scale factors in MC and data in the barrel (top) and endcap (bottom) where the non-DY processes are included (left) and subtracted (right) as functions of probe ϕ .

6. APPENDIX

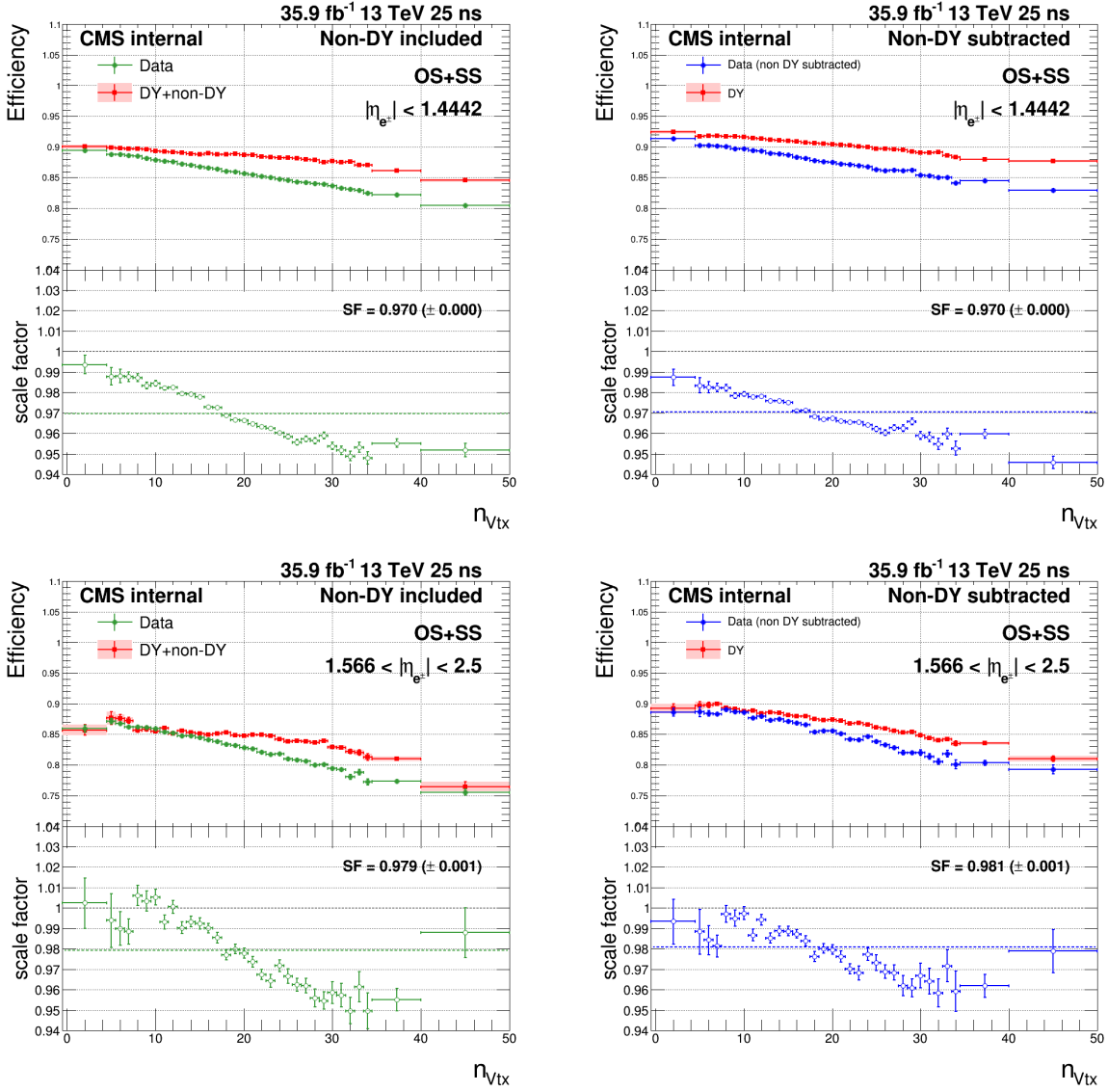


Figure 6.12: Efficiencies and scale factors in MC and data in the barrel (top) and endcap (bottom) where the non-DY processes are included (left) and subtracted (right) as functions of the number of primary vertices, n_{Vtx} .

D ee mass scale and resolution

The ee invariant mass distributions of the data and MC events passed selections describe in Chapter 3 at the Z peak are shown in figure 6.13.

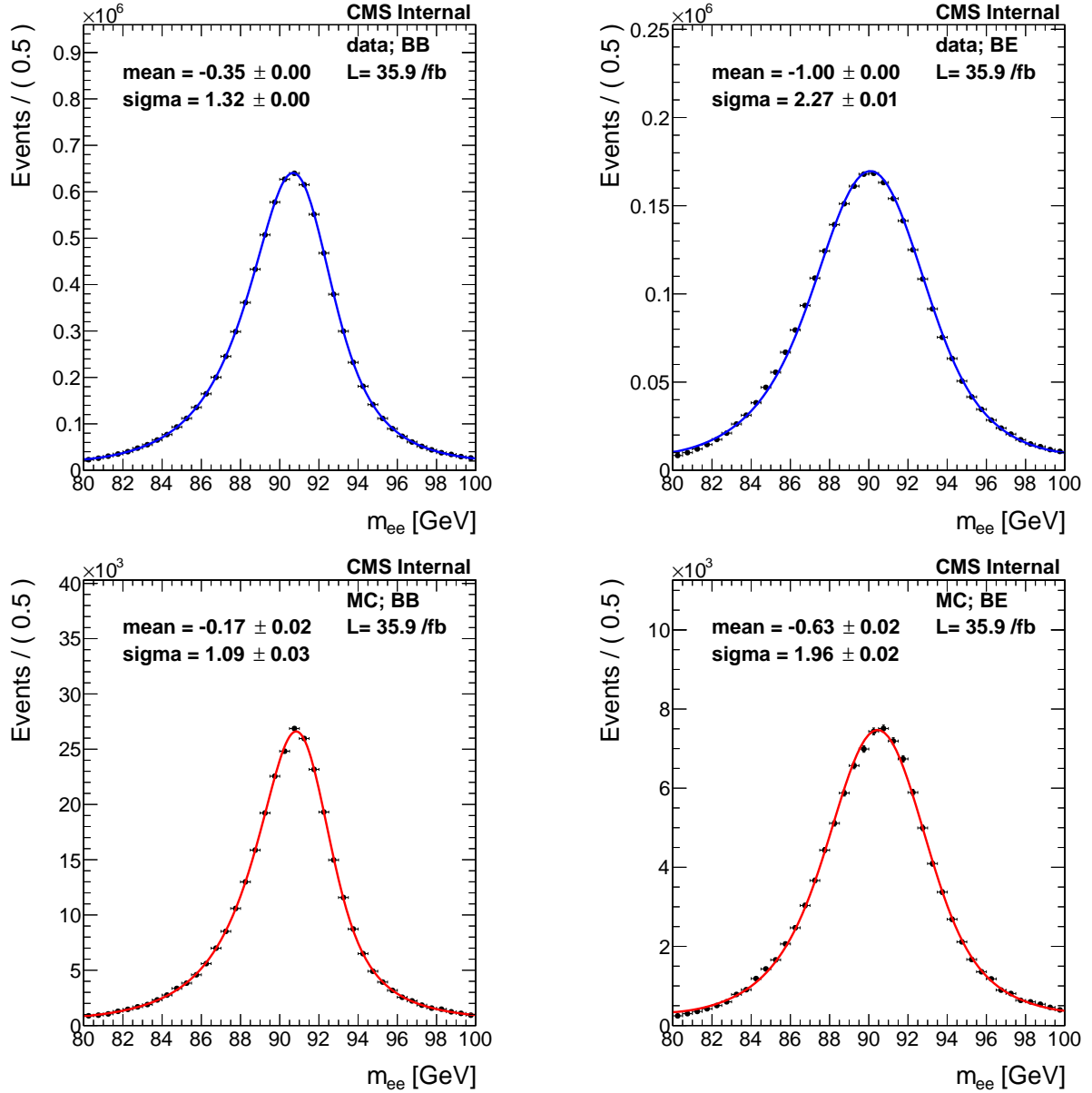


Figure 6.13: The ee invariant mass distributions at the Z peak in data (top) and MC (bottom) for the BB region (left) and BE (right) channels.

We define the mass scale variable as $scale = \frac{m_{reco}}{m_{gen}}$, which can be also written as $scale = \frac{m_{reco}}{m_{gen}} = 1 + resolution$ according to the *resolution* variable defined above. We get the mean parameter of the CB as mass scale from the fit to *resolution* distributions. Results for the BB and BE categories are shown in Fig. 6.14.

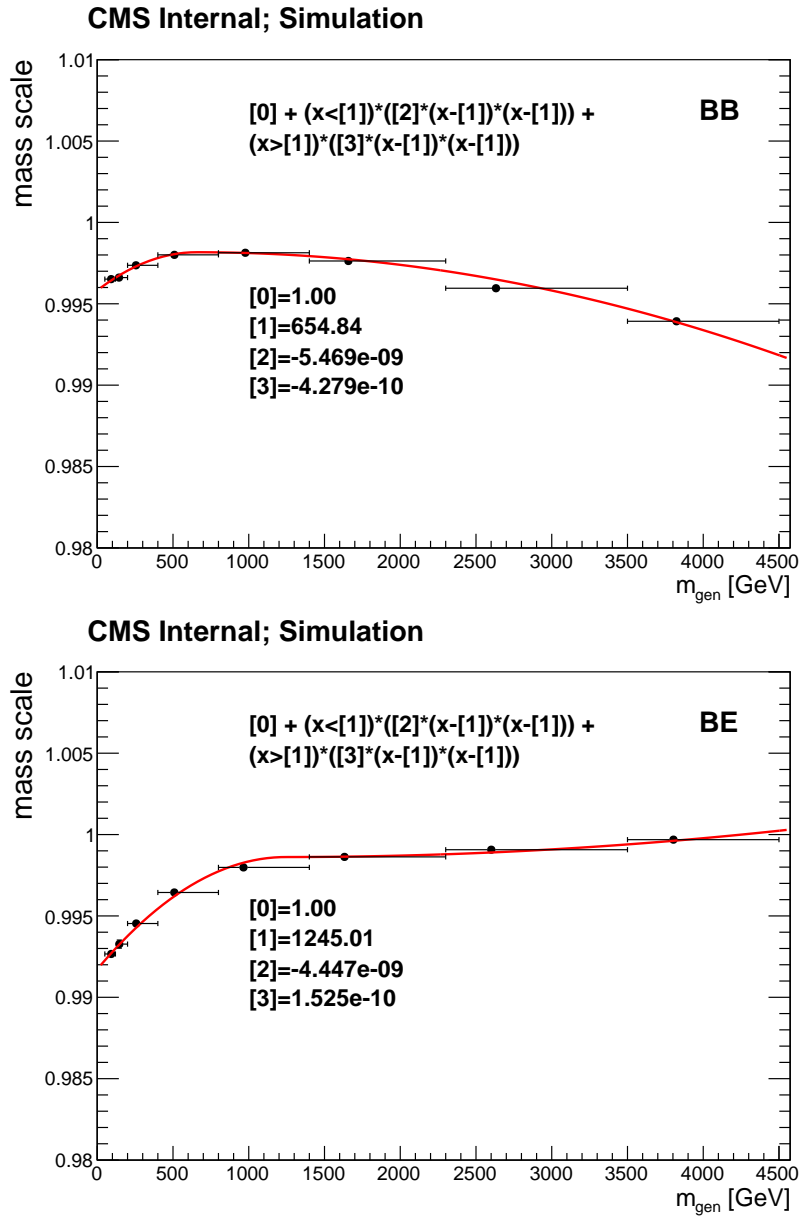


Figure 6.14: Mass scale as a function of the generated invariant mass for the barrel-barre region (top) and barrel-endcap (bottom) channels.

References

- [1] R. Barbier *et al.*, *R-parity violating supersymmetry*, Phys. Rept. **420** (2005) 1.
- [2] L. Randall and R. Sundrum, *Large Mass Hierarchy from a Small Extra Dimension*, Phys. Rev. Lett. **83** (1999) 3370.
- [3] N. Arkani-Hamed, S. Dimopoulos, and R. Dvali, *The Hierarchy Problem and New Dimensions at a Millimeter*, Phys. Lett. B **429** (1998) 263.
- [4] X. Calmet and N. Gausmann, *NONTHERMAL QUANTUM BLACK HOLES WITH QUANTIZED MASSES*, International Journal of Modern Physics **28** (2013).
- [5] X. Calmet, S. D. H. Hsu, and D. Reeb, *Quantum gravity at a TeV and the renormalization of Newton's constant*, Phys. Rev. D **77** (2008) 125015.
- [6] A. Leike, *The Phenomenology of extra neutral gauge bosons*, Phys. Rept. **317** (1999) 143.
- [7] J.L. Hewett and T.G. Rizzo, *Low-Energy Phenomenology of Superstring Inspired E(6) Models*, Phys. Rept. **183** (1989) 193.
- [8] L. Randall and R. Sundrum, *A Large mass hierarchy from a small extra dimension*, Phys. Rev. Lett. **83**, (1999) 3370.
- [9] L. Randall and R. Sundrum, *An alternative to compactification*, Phys. Rev. Lett. **83** (1999) 4690.
- [10] E. Eichten, K. Gottfried, T. Kinoshita, K. D. Lane, T.-M. Yan, *Charmonium: The model*, Phys. Rev. D **17**, (1978) 3090.
- [11] (CDF Collaboration), *Search for R-Parity Violating Decays of Sneutrinos to $e\mu$, $\mu\tau$, and $e\tau$ Pairs in $p\bar{p}$ Collisions at $\sqrt{s} = 1.96$ TeV*, Phys. Rev. Lett. **105**, (2010), 191801.
- [12] (D0), *Search for Sneutrino Production in $e\mu$ Final States in 5.3 fb^{-1} of $p\bar{p}$ Collisions at $\sqrt{s} = 1.96$ TeV*, Phys. Rev. Lett. **105**, (2010), 191802.
- [13] (ATLAS Collaboration), *Search for a heavy narrow resonance decaying to $e\mu$, $e\tau$, or $\mu\tau$ with the ATLAS detector in $s=7$ TeV pp collisions at the LHC*, Phys. Lett. B, 723 15 (2013).
- [14] (ATLAS Collaboration), *Search for a Heavy Neutral Particle Decaying to $e\mu$, $e\tau$, or $\mu\tau$ in pp Collisions at $\sqrt{s} = 8$ TeV with the ATLAS Detector*, Phys. Rev. Lett. **115**, (2015), 031801.
- [15] (ATLAS Collaboration), *Search for beyond the Standard Model phenomena in $e\mu$ final states in pp collisions at $\sqrt{s} = 13$ TeV with the ATLAS detector*, ATLAS CONF 2015-072, 2015.
- [16] (ATLAS Collaboration), *Search for new phenomena in different-flavour high-mass dilepton final states in pp collisions at $\sqrt{s} = 13$ TeV with the ATLAS detector*, Eur. Phys. J. C **76** (2016), no. 10, 541.
- [17] (CMS Collaboration), *Search for lepton flavour violating decays of heavy resonances and quantum black holes to an $e\mu$ pair in proton-antiproton collisions at $\sqrt{s} = 8$ TeV*, Eur. Phys. J. C **76** (2016): 317.

REFERENCES

- [18] (CMS Collaboration), *Search for high-mass $e\mu$ resonances*, CMS-PAS-EXO-16-001, CERN, Geneva, 2016.
- [19] (CMS collaboration), *Search for resonances in the dilepton mass distribution in pp collisions at $\sqrt{s} = 7$ TeV*, JHEP **05** (2011) 093.
- [20] (CMS collaboration), *Search for narrow resonances in dilepton mass spectra in pp collisions at $\sqrt{s} = 7$ TeV*, Phys. Lett. B **714** (2012) 158.
- [21] (CMS collaboration), *MSearch for heavy narrow dilepton resonances in pp collisions at $\sqrt{s} = 7$ TeV and $\sqrt{s} = 8$ TeV*, Phys. Lett. B **720** (2013) 63.
- [22] (CMS collaboration), *Search for physics beyond the Standard Model in dilepton mass spectra in proton-proton collisions at $\sqrt{s} = 8$ TeV*, JHEP **04** (2015) 025.
- [23] (CMS collaboration), *Search for narrow resonances in dilepton mass spectra in proton-proton collisions at $\sqrt{s} = 13$ TeV and combination with 8 TeV data*, Phys. Lett. B **768** (2017) 57.
- [24] (ATLAS collaboration), *Search for high mass dilepton resonances in pp collisions at $\sqrt{s} = 7$ TeV with the ATLAS experiment*, Phys. Lett. B **700** (2011) 163.
- [25] (ATLAS collaboration), *Search for high-mass resonances decaying to dilepton final states in pp collisions at $\sqrt{s} = 7$ TeV with the ATLAS detector*, JHEP **11** (2012) 138.
- [26] (ATLAS collaboration), *Search for high-mass dilepton resonances in pp collisions at $\sqrt{s} = 8$ TeV with the ATLAS detector*, Phys. Rev. D **90** (2014) 052005.
- [27] (ATLAS collaboration), *Search for new high-mass phenomena in the dilepton final state using 36 fb $^{-1}$ of proton-proton collision data at $\sqrt{s} = 13$ TeV with the ATLAS detector*, JHEP **10** (2017) 182.
- [28] (CDF collaboration), *Search for high-mass e^+e^- resonances in $p\bar{p}$ collisions at $\sqrt{s} = 1.96$ TeV*, Phys. Rev. Lett. **102** (2009) 031801.
- [29] (CDF collaboration), *A search for high-mass resonances decaying to dimuons at CDF*, Phys. Rev. Lett. **102** (2009) 091805.
- [30] (D0 collaboration), *Search for Randall-Sundrum gravitons in the dielectron and diphoton final states with 5.4 fb $^{-1}$ of data from $p\bar{p}$ collisions at $\sqrt{s} = 1.96$ TeV*, Phys. Rev. Lett. **104** (2010) 241802.
- [31] (D0 collaboration), *Search for a heavy neutral gauge boson in the dielectron channel with 5.4 fb $^{-1}$ of $p\bar{p}$ collisions at $\sqrt{s} = 1.96$ TeV*, Phys. Lett. B **695** (2011) 88.
- [32] CDF collaboration, *Search for high mass resonances decaying to muon pairs in $\sqrt{s} = 1.96$ TeV $p\bar{p}$ collisions*, Phys. Rev. Lett. **106** (2011) 121801.
- [33] CDF collaboration, *Search for new dielectron resonances and Randall-Sundrum gravitons at the collider detector at Fermilab*, Phys. Rev. Lett. **107** (2011) 051801.
- [34] S. Godfrey, N. Isgur, *Mesons in a relativized quark model with chromodynamics*, Phys. Rev. D **32**, (1985)189.
- [35] T. Barnes, S. Godfrey, E. S. Swanson, *Higher charmonia*, Phys. Rev. D **72**, (2005) 054026.
- [36] *CLEO home page*, <https://www.classe.cornell.edu/Research/CLEO/>
- [37] *BESIII home page*, <http://bes3.ihep.ac.cn/>
- [38] *CDF home page*, <https://www-cdf.fnal.gov/>
- [39] *D0 home page*, <https://www-d0.fnal.gov/>

-
- [40] *LHCb home page*, <https://lhcb.web.cern.ch/lhcb/>
- [41] *CMS home page*, <https://cms.cern/>
- [42] S. K. Choi *et al.* (Belle Collaboration), *Observation of a Narrow Charmoniumlike State in Exclusive $B^\pm \rightarrow K^\pm \pi^+ \pi^- J/\psi$ Decays*, Phys. Rev. Lett. **91**, 262001 (2003).
- [43] G. Gokhroo, *et al.*, (Belle Collaboration), *Observation of a Near-Threshold $D^0 \bar{D}^0 \pi^0$ Enhancement in $B \rightarrow D^0 \bar{D}^0 \pi^0 K$ Decay*, Phys. Rev. Lett. **97** (2006) 162002.
- [44] I. Adachi, *et al.*, *Study of $X(3872)$ in B meson decays*, in: Proceedings, 34th International Conference on High Energy Physics (ICHEP 2008).
- [45] T. Aushev, *et al.*, (Belle Collaboration), *Study of the $B \rightarrow X(3872)(\rightarrow D^{*0} \bar{D}^0)K$ decay*, Phys. Rev. D **81**, (2010) 031103.
- [46] V. Bhardwaj, *et al.*, (Belle Collaboration), *Observation of $X(3872) \rightarrow J/\psi \gamma$ and Search for $X(3872) \rightarrow \psi' \gamma$ in B Decays*, Phys. Rev. Lett. **107** (2011) 091803.
- [47] S. K. Choi, *et al.*, *Bounds on the width, mass difference and other properties of $X(3872) \rightarrow \pi^+ \pi^- J/\psi$ decays*, Phys. Rev. D **84**, (2011) 052004.
- [48] A. Abulencia, *et al.*, (CDF Collaboration), *Measurement of the Dipion Mass Spectrum in $X(3872) \rightarrow J/\psi \pi^+ \pi^-$ Decays*, Phys. Rev. Lett. **96** (2006) 102002.
- [49] R. Aaij, *et al.*, (LHCb Collaboration), *Determination of the $X(3872)$ Meson Quantum Numbers*, Phys. Rev. Lett. **110** (2013) 222001.
- [50] M. Ablikim, *et al.*, (BESIII Collaboration), *Observation of the $\psi(1^3D_2)$ State in $e^+ e^- \rightarrow \pi^+ \pi^- \gamma \chi_{c1}$ at BESIII*, Phys. Rev. Lett. **115** (2015) 011803.
- [51] V. Bhardwaj, *et al.*, (Belle Collaboration), *Evidence of a New Narrow Resonance Decaying to $\chi_{c1} \gamma$ in $B \rightarrow \chi_{c1} \gamma K$* , Phys. Rev. Lett. **111** (2013) 032001.
- [52] K. Abe, *et al.*, (Belle Collaboration), *Observation of a Charmoniumlike State Produced in Association with a J/ψ in $e^+ e^-$ Annihilation at $\sqrt{s} \approx 10.6$ GeV*, Phys. Rev. Lett. **98** (2007) 082001.
- [53] P. Pakhlov, *et al.*, (Belle Collaboration), *Production of New Charmoniumlike States in $e^+ e^- \rightarrow J/\psi D^{(*)} \bar{D}^{(*)}$ at $\sqrt{s} \approx 10.6$ GeV*, Phys. Rev. Lett. **100** (2008) 202001.
- [54] S. Uehara, *et al.*, (Belle Collaboration), *Observation of a Charmoniumlike Enhancement in the $\gamma\gamma \rightarrow \omega J/\psi$ Process*, Phys. Rev. Lett. **104** (2010) 092001.
- [55] J. P. Lees, *et al.*, (BaBar Collaboration), *Study of $X(3915) \rightarrow J/\psi \omega$ in two-photon collisions*, Phys. Rev. D **86**, (2012) 072002.
- [56] C. P. Shen, *et al.*, (Belle Collaboration), *Evidence for a New Resonance and Search for the $Y(4140)$ in the $\gamma\gamma \rightarrow \phi J/\psi$ Process*, Phys. Rev. Lett. **104** (2010) 112004.
- [57] K. Abe, *et al.*, (Belle Collaboration), *Observation of a Near-Threshold $\omega J/\psi$ Mass Enhancement in Exclusive $B \rightarrow K \omega J/\psi$ Decays*, Phys. Rev. Lett. **94** (2005) 182002.
- [58] P. del Amo Sanchez, *et al.*, (BaBar Collaboration), *Evidence for the decay $X(3872) \rightarrow J/\psi \omega$* , Phys. Rev. D **82**, (2010) 011101.
- [59] T. Aaltonen, *et al.*, (CDF Collaboration), *Evidence for a Narrow Near-Threshold Structure in the $J/\psi \phi$ Mass Spectrum in $B^+ \rightarrow J/\psi \phi K^+$ Decays*, Phys. Rev. Lett. **102** (2009) 242002.

REFERENCES

- [60] T. Aaltonen, *et al.*, (CDF Collaboration), *Observation of the $Y(4140)$ structure in the $J/\psi\phi$ mass spectrum in $B^\pm \rightarrow J/\psi\phi K^\pm$ decays*, Mod. Phys. Lett. A, **26** (2017) 1750139.
- [61] R. Aaij, *et al.*, (LHCb Collaboration), *Search for the $X(4140)$ state in $B^+ \rightarrow J/\psi\phi K^+$ decays*, Phys. Rev. D **85**, (2012) 091103.
- [62] V. M. Abazov, *et al.*, (D0 Collaboration), *Search for the $X(4140)$ state in $B^+ \rightarrow J/\psi\phi K^+$ decays with the D0 detector*, Phys. Rev. D **89**, (2014) 012004.
- [63] S. Chatrchyan, *et al.*, [CMS Collaboration], *Observation of a peaking structure in the $J/\psi\phi$ mass spectrum from $B^\pm \rightarrow J/\psi\phi K^\pm$ decays*, Phys. Lett. B **734**, (2014) 261-281.
- [64] C. Z. Yuan *et al.* (Belle Collaboration), *Measurement of the $e^+e^- \rightarrow \pi^+\pi^- J/\psi$ Cross Section Via Initial-State Radiation at Belle*, Phys. Rev. Lett. **99**, 182004 (2007).
- [65] Q. He, *et al.*, (CLEO Collaboration), *Confirmation of the $Y(4260)$ resonance production in initial state radiation*, Phys. Rev. D. **74** (2006) 091104.
- [66] Z. Q. Liu *et al.* (Belle Collaboration), *Study of $e^+e^- \rightarrow \pi^+\pi^- J/\psi$ and Observation of a Charged Charmoniumlike State at Belle*, Phys. Rev. Lett. **110**, 252002 (2013).
- [67] J. P. Lees *et al.* (BaBar Collaboration), *Study of the reaction $e^+e^- \rightarrow J/\psi\pi^+\pi^-$ via initial-state radiation at BABAR*, Phys. Rev. D **86**, 051102(R) (2012).
- [68] B. Aubert *et al.* (BaBar Collaboration), *Evidence of a Broad Structure at an Invariant Mass of 4.32 GeV/ c^2 in the Reaction $e^+e^- \rightarrow \pi^+\pi^-\psi(2S)$ Measured at BABAR*, Phys. Rev. Lett. **98**, 212001 (2007).
- [69] X. L. Wang *et al.* (Belle Collaboration), *Observation of Two Resonant Structures in $e^+e^- \rightarrow \pi^+\pi^-\psi(2S)$ via Initial-State Radiation at Belle*, Phys. Rev. Lett. **99**, 142002 (2007).
- [70] J. P. Lees, *et al.*, (BaBar Collaboration), *Study of the reaction $e^+e^- \rightarrow \psi(2S)\pi^+\pi^-$ via initial-state radiation at BaBar*, Phys. Rev. D **89**, (2014) 111103.
- [71] G. Pakhlova, *et al.*, (Belle Collaboration), *Observation of a Near-Threshold Enhancement in the $e^+e^- \rightarrow \Lambda_c^+\Lambda_c^-$ Cross Section Using Initial-State Radiation*, Phys. Rev. Lett. **101** (2008) 172001.
- [72] S. K. Choi, *et al.*, (Belle Collaboration), *Observation of a Resonancelike Structure in the $\pi^{+-}\psi'$ Mass Distribution in Exclusive $B \rightarrow K\pi^{+-}\psi'$ Decays*, Phys. Rev. Lett. **100** (2008) 142001.
- [73] (BaBar Collaboration), *Search for the $Z(4430)^-$ at BABAR*, Phys. Rev. D. **79** (2009) 112001.
- [74] R. Aaij, *et al.*, (LHCb Collaboration), *Observation of the Resonant Character of the $Z(4430)^-$ State*, Phys. Rev. Lett. **112** (2014) 222002.
- [75] R. Mizuk, *et al.*, (Belle Collaboration), *Observation of two resonancelike structures in the $\pi^+\chi_{c1}$ mass distribution in exclusive $\bar{B}^0 \rightarrow K^-\pi^+\chi_{c1}$ decays*, Phys. Rev. D **78**, (2008) 072004.
- [76] J. P. Lees, *et al.*, (BaBar Collaboration), *Search for the $Z_1(4050)^+$ and $Z_2(4250)^+$ states in $\bar{B}^0 \rightarrow \chi_{c1}K^-\pi^+$ and $B^+ \rightarrow \chi_{c1}K_S^0\pi^+$* , Phys. Rev. D **85**, (2012) 052003.
- [77] K. Chilikin, *et al.*, (Belle Collaboration), *Observation of a new charged charmoniumlike state in $\bar{B}^0 \rightarrow J/\psi K^-\pi^+$ decays*, Phys. Rev. D **90**, (2014) 112009.
- [78] B. Aubert *et al.* (BaBar Collaboration), *Observation of a Broad Structure in the $\pi^+\pi^- J/\psi$ Mass Spectrum around 4.26 GeV/ c^2* , Phys. Rev. Lett. **95**, 142001 (2005).
- [79] S. Uehara, *et al.*, (Belle Collaboration), *Observation of a χ'_{c2} Candidate in $\gamma\gamma \rightarrow D\bar{D}$ Production at Belle*, Phys. Rev. Lett. **96** (2006) 082003.

- [80] B. Aubert, *et al.*, (BaBar Collaboration), *Observation of the $\chi_{c2}(2P)$ meson in the reaction $\gamma\gamma \rightarrow D\bar{D}$ at BABAR*, Phys. Rev. D **81**, (2010) 092003.
- [81] M. Ablikim *et al.* (BESIII Collaboration), *Observation of a Charged Charmoniumlike Structure in $e^+e^- \rightarrow \pi^+\pi^- J/\psi$ at $\sqrt{s}=4.26$ GeV*, Phys. Rev. Lett. **110**, (2013) 252001.
- [82] M. Ablikim, *et al.*, (BESIII Collaboration), *Observation of a Charged $(D\bar{D}^*)^\pm$ Mass Peak in $e^+e^- \rightarrow \pi D\bar{D}^*$ at $\sqrt{s} = 4.26$ GeV*, Phys. Rev. Lett. **112** (2014) 022001.
- [83] M. Ablikim, *et al.*, (BESIII Collaboration), *Observation of $Z_c(3900)^0$ in $e^+e^- \rightarrow \pi^0\pi^0 J/\psi$* , Phys. Rev. Lett. **115** (2015) 112003.
- [84] M. Ablikim, *et al.*, (BESIII Collaboration), *Observation of a Neutral Structure near the $D\bar{D}^*$ Mass Threshold in $e^+e^- \rightarrow (D\bar{D}^*)^0\pi^0$ at $\sqrt{s} = 4.226$ and 4.257 GeV*, Phys. Rev. Lett. **115** (2015) 222002.
- [85] M. Ablikim, *et al.*, (BESIII Collaboration), *Observation of a Charged Charmoniumlike Structure in $e^+e^- \rightarrow (D^*\bar{D}^*)^\pm\pi^\mp$ at $\sqrt{s} = 4.26$ GeV*, Phys. Rev. Lett. **112** (2014) 132001.
- [86] M. Ablikim *et al.* (BESIII Collaboration), *Observation of a Charged Charmoniumlike Structure $Z_c(4020)$ and Search for the $Z_c(3900)$ in $e^+e^- \rightarrow \pi^+\pi^- h_c$* , Phys. Rev. Lett. **111**, (2013) 242001.
- [87] J. He, X. Liu, Z.-F. Sun, S.-L. Zhu, *$Z_c(4025)$ as the hadronic molecule with hidden charm*, Eur. Phys. J. C **73**, (2013) 2635.
- [88] R. Aaij, *et al.*, (LHCb Collaboration), *Observation of J/ψ Resonances Consistent with Pentaquark States in $\Lambda_b^0 \rightarrow J/\psi K^- p$ Decays*, Phys. Rev. Lett. **115** (2015) 072001.
- [89] *PANDA home page*, <https://panda.gsi.de/>
- [90] For recent reviews, see, H. X. Chen, W. Chen, X. Liu and S. L. Zhu, *The hidden-charm pentaquark and tetraquark states*, Phys. Rept. **639**, 1 (2016); N. Brambilla *et al.*, *Heavy quarkonium: progress, puzzles, and opportunities*, Eur. Phys. J. C **71**, 1534 (2011).
- [91] S.-L. Zhu, *The possible interpretations of $Y(4260)$* , Phys. Lett. B **625**, (2005) 212.
- [92] S.-L. Zhu, *Masses and decay widths of heavy hybrid mesons*, Phys. Rev. D **60**, (1999) 014008.
- [93] S.-L. Zhu, *Some decay modes of the 1^{-+} hybrid meson in QCD sum rules reexamined*, Phys. Rev. D **60**, (1999) 097502.
- [94] F. E. Close, P. R. Page, *The production and decay of hybrid mesons by flux-tube breaking*, Nucl. Phys. B **443**, (1995) 233-254.
- [95] F. E. Close, S. Godfrey, *Charmonium hybrid production in exclusive B-meson decays*, Phys. Lett. B **574**, (2003) 210-216.
- [96] E. Kou, O. Pene, *Suppressed decay into open charm for the $Y(4260)$ being an hybrid*, Phys. Lett. B. **631** (2005) 164-169.
- [97] F. E. Close, P. R. Page, *Gluonic charmonium resonances at BaBar and Belle?*, Phys. Lett. B **628**, (2005) 215-222.
- [98] L. Liu, G. Moir, M. Peardon, S. M. Ryan, C. E. Thomas, P. Vilaseca, J. J. Dudek, R. G. Edwards, B. Joo, D. G. Richards, (Hadron Spectrum Collaboration), *Excited and exotic charmonium spectroscopy from lattice QCD*, JHEP **07** (2012) 126.
- [99] L. Maiani, V. Riquer, F. Piccinini, A. D. Polosa, *Four quark interpretation of $Y(4260)$* , Phys. Rev. D **72** (2005) 031502.

REFERENCES

- [100] I. Bigi, L. Maiani, F. Piccinini, A. D. Polosa, V. Riquer, *Four-quark mesons in nonleptonic B decays: Could they resolve some old puzzles?*, Phys. Rev. D **72**, (2005) 114016.
- [101] N. V. Drenska, R. Faccini, A. D. Polosa, *Exotic hadrons with hidden charm and strangeness*, Phys. Rev. D **79**, (2009) 077502.
- [102] H. X. Chen, L. Maiani, A. D. Polosa, V. Riquer, *$Y(4260) \rightarrow \gamma + X(3872)$ in the diquarkonium picture*, Eur. Phys. J. C **75**, (11) (2015) 550.
- [103] D. Ebert, R. N. Faustov, V. O. Galkin, *Masses of heavy tetraquarks in the relativistic quark model*, Phys. Lett. B **634**, (2006) 214-219.
- [104] D. Ebert, R. N. Faustov, V. O. Galkin, *Excited heavy tetraquarks with hidden charm*, Eur. Phys. J. C **58**, (2008) 399-405.
- [105] W. Chen, S.-L. Zhu, *Vector and axial-vector charmoniumlike states*, Phys. Rev. D **83**, (2011) 034010.
- [106] C. Z. Yuan, P. Wang, X. H. Mo, *The $Y(4260)$ as an $\omega\chi_{c1}$ molecular state*, Phys. Lett. B **634**, (2006) 399-402.
- [107] G.-J. Ding, *Are $Y(4260)$ and $Z_2^+(4250)$ D_1D or D_0D^* hadronic molecules?*, Phys. Rev. D **79** (2009) 014001.
- [108] F. Close, C. Downum, *Possibility of Deeply Bound Hadronic Molecules from Single Pion Exchange*, Phys. Rev. Lett. **102** (2009) 242003.
- [109] F. Close, C. Downum, C. E. Thomas, *Novel charmonium and bottomonium spectroscopies due to deeply bound hadronic molecules from single pion exchange*, Phys. Rev. D **81**, (2010) 074033.
- [110] M. Cleven, Q. Wang, F.-K. Guo, C. Hanhart, U.-G. Meissner, Q. Zhao, *$Y(4260)$ as the first S-wave open charm vector molecular state?*, Phys. Rev. D **90** (2014) 074039.
- [111] E. van Beveren, G. Rupp, *Interference effects in the $X(4260)$ signal*, Phys. Rev. D **79** (2009) 111501.
- [112] D.-Y. Chen, J. He, X. Liu, *Nonresonant explanation for the $Y(4260)$ structure observed in the $e^+e^- \rightarrow J/\psi\pi^+\pi^-$ process*, Phys. Rev. D **83** (2011) 054021.
- [113] G. Pakhlova, *et al.*, (Belle Collaboration), *Measurement of the near-threshold $e^+e^- \rightarrow D\bar{D}$ cross section using initial-state radiation*, Phys. Rev. D **77**, (2008) 011103.
- [114] K. Abe, *et al.*, (Belle Collaboration), *Measurement of the Near-Threshold $e^+e^- \rightarrow D^{(*)\pm}D^{(*)\mp}$ Cross Section using Initial-State Radiation*, Phys. Rev. Lett. **98** (2007) 092001.
- [115] G. Pakhlova, *et al.*, (Belle Collaboration), *Observation of the $\psi(4415) \rightarrow D\bar{D}_2^*(2460)$ Decay Using Initial-State Radiation*, Phys. Rev. Lett. **100** (2008) 062001.
- [116] CMS collaboration, *The CMS experiment at the CERN LHC*, 2008 JINST **3** S08004.
- [117] X. Calmet, W. Gong and S.D.H. Hsu, *Colorful quantum black holes at the LHC*, Phys. Lett. B **668** (2008) 20.
- [118] P. Meade and L. Randall, *Black holes and quantum gravity at the LHC*, JHEP **05** (2008) 003.
- [119] P. Langacker, *The physics of heavy Z' gauge bosons*, Rev. Mod. Phys. **81** (2009) 1199.
- [120] A. Belyaev, N.D. Christensen and A. Pukhov, *CalcHEP 3.4 for collider physics within and beyond the Standard Model*, Comput. Phys. Commun. **184** (2013) 1729.
- [121] T. Sjostrand, S. Mrenna and P.Z. Skands, *A Brief Introduction to PYTHIA 8.1*, Comput. Phys. Commun. **178** (2008) 852.

-
- [122] D.M. Gingrich, *Monte Carlo event generator for black hole production and decay in proton-proton collisions QBH version 1.02*, Comput. Phys. Commun. **181** (2010) 1917.
- [123] (CMS collaboration), *Event generator tunes obtained from underlying event and multiparton scattering measurements*, Eur. Phys. J. C **76** (2016) 155.
- [124] J. Pumplin, D.R. Stump, J. Huston, H.L. Lai, P.M. Nadolsky and W.K. Tung, *New Generation of Parton Distributions with Uncertainties from Global QCD Analysis*, JHEP **07** (2002) 012.
- [125] (NNPDF collaboration), R.D. Ball *et al.*, *Parton distributions for the LHC run II*, JHEP **04** (2015) 040.
- [126] (GEANT4 collaboration), S. Agostinelli *et al.*, *GEANT4: A Simulation toolkit*, Nucl. Instrum. Meth. A **506** (2003) 250.
- [127] J. Allison *et al.*, *Geant4 developments and applications*, IEEE Trans. Nucl. Sci. **53** (2006) 270.
- [128] J. Allison *et al.*, *Recent developments in Geant4*, Nucl. Instrum. Meth. A **835** (2016) 186.
- [129] S. Frixione, P. Nason and C. Oleari, *Matching NLO QCD computations with parton shower simulations: the POWHEG method*, JHEP **11** (2007) 070.
- [130] P. Nason, *A New Method for Combining NLO QCD with Shower Monte Carlo Algorithms*, JHEP **11** (2004) 040.
- [131] S. Alioli, P. Nason, C. Oleari and E. Re, *A general framework for implementing NLO calculations in shower Monte Carlo programs: the POWHEG BOX*, JHEP **06** (2010) 043.
- [132] R. Frederix and S. Frixione, *Merging meets matching in MC@NLO*, JHEP **12** (2012) 061.
- [133] J. Alwall *et al.*, *The automated computation of tree-level and next-to-leading order differential cross sections, and their matching to parton shower simulations* JHEP **07** (2014) 079.
- [134] (CMS Collaboration). *Search for lepton flavour violating decays of heavy resonances in pp collisions with CMS detector*, CMS Analysis Note AN-16-163 (2017).
- [135] (CMS collaboration), *The CMS trigger system*, 2017 JINST **12** P01020.
- [136] (CMS collaboration), *Performance of CMS muon reconstruction in pp collision events at $\sqrt{s} = 7$ TeV*, 2012 JINST **7** P10002.
- [137] (CMS collaboration), *Performance of electron reconstruction and selection with the CMS detector in proton-proton collisions at $\sqrt{s} = 8$ TeV*, 2015 JINST **10** P06005.
- [138] (CMS Collaboration), *Search for high-mass resonances in dilepton final states in proton-proton collisions at $\sqrt{s} = 13$ TeV*, JHEP, **06** (2018) 120.
- [139] B. D. Pecjak, D. J. Scott, X. Wang, and L. L. Yang, *Probing the Small- x Gluon Tomography in Correlated Hard Diffractive Dijet Production in Deep Inelastic Scattering*, Phys. Rev. Lett. **116** (2016), no. 20, 202001.
- [140] (CMS Collaboration), *Search for lepton-flavor violating decays of heavy resonances and quantum black holes to $e\mu$ final states in proton-proton collisions at $\sqrt{s} = 13$ TeV*, JHEP, **04** (2018) 073.
- [141] (CMS Collaboration). *Search for high mass di-electron resonances with the full 2016 data*, CMS Analysis Note AN-16-404 (2017).
- [142] (CMS Collaboration). *Search for high mass resonances in the dielectron final state*, CMS Analysis PAS AN-18-006 (2018).
- [143] G. Altarelli, B. Mele and M. Ruiz-Altaba, *Searching for New Heavy Vector Bosons in $p\bar{p}$ Colliders*, Z. Phys. C **45** (1989) 109.

REFERENCES

- [144] P. Nason, *A New method for combining NLO QCD with shower Monte Carlo algorithms*, JHEP **11** (2004) 040.
- [145] S. Frixione, P. Nason and C. Oleari, *Matching NLO QCD computations with Parton Shower simulations: the POWHEG method*, JHEP **11** (2007) 070.
- [146] S. Alioli *et al.*, *A general framework for implementing NLO calculations in shower Monte Carlo programs: the POWHEG BOX*, JHEP **06** (2010) 043.
- [147] S. Alioli, P. Nason, C. Oleari and E. Re, *NLO vector-boson production matched with shower in POWHEG*, JHEP **07** (2008) 060.
- [148] S. Frixione, P. Nason and G. Ridolfi, *A Positive-weight next-to-leading-order Monte Carlo for heavy flavour hadroproduction*, JHEP **09** (2007) 126.
- [149] E. Re, *Single-top Wt -channel production matched with parton showers using the POWHEG method*, Eur. Phys. J. C **71** (2011) 1547.
- [150] (NNPDF collaboration), R.D. Ball *et al.*, *Parton distributions for the LHC Run II*, JHEP **04** (2015) 040.
- [151] (CMS collaboration), *Event generator tunes obtained from underlying event and multiparton scattering measurements*, Eur. Phys. J. C **76** (2016) 155.
- [152] Y. Li and F. Petriello, *Combining QCD and electroweak corrections to dilepton production in FEWZ*, Phys. Rev. D **86** (2012) 094034.
- [153] D. Bourilkov, *Photon-induced Background for Dilepton Searches and Measurements in pp Collisions at 13 TeV*, arXiv:1606.00523.
- [154] D. Bourilkov, *Exploring the LHC Landscape with Dileptons*, arXiv:1609.08994.
- [155] M. Czakon and A. Mitov, *Top++: A Program for the Calculation of the Top-Pair Cross-Section at Hadron Colliders*, **185** (2014) 2930.
- [156] J. Alwall *et al.*, *The automated computation of tree-level and next-to-leading order differential cross sections, and their matching to parton shower simulations*, JHEP **07** (2014) 079.
- [157] (CMS collaboration), *Search for Resonances in the Dilepton Mass Distribution in pp Collisions at $\sqrt{s} = 7$ TeV*, JHEP **05** (2011) 093.
- [158] (CMS collaboration), *Search for physics beyond the Standard Model in dilepton mass spectra in proton-proton collisions at $\sqrt{s} = 8$ TeV*, JHEP **04** (2015) 025.
- [159] L. Moneta *et al.*, *The RooStats Project*, PoS(ACAT2010)057.
- [160] (ATLAS and CMS Collaborations and The LHC Higgs Combination Group), *Procedure for the LHC Higgs boson search combination in summer 2011*, CMS-NOTE-2011-005 (2011).
- [161] N. Metropolis *et al.*, *Equation of state calculations by fast computing machines*, J. Chem. Phys. **21** (1953) 1087.
- [162] W. K. HASTINGS, *Monte Carlo Sampling Methods Using Markov Chains and Their Applications*, Biometrika **57** (1970) 97.
- [163] (CMS Collaboration), *Search for high-mass resonances in dilepton final states in proton-proton collisions at $\sqrt{s} = 13$ TeV*, JHEP **1806** (2018) 120.
- [164] T. Barnes, S. Godfrey and E. S. Swanson, *Higher charmonia*, Phys. Rev. D **72**, 054026 (2005).
- [165] T. K. Pedlar *et al.* (CLEO Collaboration), *Observation of the $h_c(1P)$ using e^+e^- collisions above $D\bar{D}$ threshold*, Phys. Rev. Lett. **107**, 041803 (2011).

- [166] Chang-Zheng Yuan, *Evidence for resonant structures in $e^+e^- \rightarrow \pi^+\pi^-h_c$* , Chin. Phys. C **38**, 043001 (2014).
- [167] C. Patrignani *et al.* (Particle Data Group), *Review of Particle Physics*, Chin. Phys. C **40**, 100001 (2016).
- [168] M. Ablikim *et al.* (BESIII Collaboration), *Study of $e^+e^- \rightarrow \omega\chi_{cJ}$ at center-of-mass energies from 4.21 to 4.42 GeV*, Phys. Rev. Lett. **114**, 092003 (2015).
- [169] X. N. Feng, X. Y. Gao and C. P. Shen, *Combined fit to BESIII data on $e^+e^- \rightarrow h_c\pi^+\pi^-$ and $\chi_{c0}\omega$* , Int. J. Mod. Phys. A **30**, 1550142 (2015).
- [170] R. Faccini, G. Filaci, A. L. Guerrieri, A. Pilloni and A. D. Polosa, *Note on the newly observed $Y(4220)$ resonance*, Phys. Rev. D **91**, 117501 (2015).
- [171] M. Ablikim *et al.* (BESIII Collaboration), *Evidence of Two Resonant Structures in $e^+e^- \rightarrow \pi^+\pi^-h_c$* , Phys. Rev. Lett. **118**, 092002 (2017).
- [172] M. Ablikim *et al.* (BESIII Collaboration), *Observation of $e^+e^- \rightarrow \omega\chi_{c1,2}$ near $\sqrt{s} = 4.42$ and 4.6 GeV*, Phys. Rev. D **93**, 011102(R) (2016).
- [173] M. Ablikim *et al.* (BESIII Collaboration), *Precise measurement of the $e^+e^- \rightarrow \pi^+\pi^-J/\psi$ cross section at center-of-mass energies from 3.77 to 4.60 GeV*, Phys. Rev. Lett. **118**, 092001 (2017).
- [174] M. Ablikim *et al.* (BESIII Collaboration), *Evidence of a resonant structure in the $e^+e^- \rightarrow \pi^+D^0D^{*-}$ cross section between 4.05 and 4.60 GeV*, Phys. Rev. Lett. **122**, 102002 (2019).
- [175] G. Pakhlova *et al.* (Belle Collaboration), *Measurement of the $e^+e^- \rightarrow D^0D^{*-}\pi^+$ cross section using initial-state radiation*, Phys. Rev. D **80**, 091101(R) (2009).
- [176] G. Pakhlova, *$e^+e^- \rightarrow$ charm cross sections via ISR*, Chin. Phys. C **34**, 656 (2010).
- [177] R. Faccini, G. Filaci, A. L. Guerrieri, A. Pilloni and A. D. Polosa, *Note on the newly observed $Y(4220)$ resonance*, Phys. Rev. D **91**, 117501 (2015).
- [178] M. Cleven, Q. Wang, F.-K. Guo, C. Hanhart, U.-G. Meißner and Q. Zhao, *$Y(4260)$ as the first S -wave open charm vector molecular state?*, Phys. Rev. D **90**, 074039 (2014).
- [179] X. Li and M. B. Voloshin, *$Y(4260)$ and $Y(4360)$ as mixed hadrocharmonium*, Mod. Phys. Lett. A **29**, 1450060 (2014).
- [180] L. Y. Dai, M. Shi, G. Y. Tang and H. Q. Zheng, *Nature of $X(4260)$* , Phys. Rev. D **92**, 014020 (2015).
- [181] C. Z. Yuan, P. Wang and X. H. Mo, *The $Y(4260)$ as an omega chi($c1$) molecular state*, Phys. Lett. B **634**, 399 (2006).
- [182] T. Barnes, F. E. Close and E. S. Swanson, *Hybrid and conventional mesons in the flux tube model: Numerical studies and their phenomenological implications*, Phys. Rev. D **52**, 5242 (1995); P. Guo, A. P. Szczepaniak, G. Galata, A. Vassallo and E. Santopinto, *Heavy quarkonium hybrids from Coulomb gauge QCD* Phys. Rev. D **78**, 056003 (2008); J. J. Dudek and E. Rrapaj, *Charmonium in lattice QCD and the non-relativistic quark-model*, Phys. Rev. D **78**, 094504 (2008).
- [183] J. James, MINUIT, CERN Program Library Writeup Report No. D506.
- [184] Y. Chen, W. F. Chiu, M. Gong, L. C. Gui and Z. Liu, *Exotic vector charmonium and its leptonic decay width*, Chin. Phys. C, **40**, 081002 (2016).
- [185] W. Qin, S. R. Xue and Q. Zhao, *Production of $Y(4260)$ as a hadronic molecule state of $\bar{D}D_1 + c.c.$ in e^+e^- annihilations*, Phys. Rev. D **94**, 054035 (2016).

REFERENCES

- [186] L. Y. Dai, M. Shi, G. Y. Tang and H.Q. Zheng, *Nature of $X(4260)$* , Phys. Rev. D **92**, 014020 (2015).